A Spectroscopic Study of Electronic Correlations in Twisted Bilayer Graphene by Scanning Tunneling Microscopy

Thesis by
Youngjoon Choi

In Partial Fulfillment of the Requirements for the
Degree of
Doctor of Philosophy

CALIFORNIA INSTITUTE OF TECHNOLOGY
Pasadena, California

2022
Defended August 23, 2021

Youngjoon Choi
ORCID: 0000-0001-9783-5992

ACKNOWLEDGEMENTS

First, I want to thank my advisor Stevan for his support and guidance along this journey. Among many other invaluable lessons, I learned how to priotize what to study with given resources, how to identify essential physics out of experimental details, and how to tackle problems interacting with other brains. I have really enjoyed numerous discussions with him while having a great freedom to pursue what I wanted to try, the best combination of independence and directed motivation I can imagine.

Also I owe a lot to the STM team members I have worked with. Most of my backgrounds on STM is from Dr. Jeannette Kemmer who taught me with patience. Thanks to Hyunjin Kim, his devotion to physics and hard work always amaze me. I will miss our daily chat on every subject.

Being surrounded by all other wonderful members in the lab was a blessing to me : Dr. HP Arora, Robbie Polski, Yiran Zhang, Jash Banker, Dr. Hechen Ren, Dr. Ding Zhong, and Dr. Soudi Mashhadi, who made the exchange of ideas easy and the atmosphere fun. I was also very fortunate to have brilliant theory collaborators : Prof. Yang Peng, Dr. Cyprian Lewandowski, Dr. Alex Thomson, Prof. Jason Alicea, Prof. Gil Refael, and Prof. Felix von Oppen. I would like to thank Prof. Dave Hsieh and Prof. Patrick Lee for supports and being on the committee along the way.

Music house has been one of my shelters away from the overloads of the research. Thanks to Delores Bing, Maia Jasper White, Martin Chalifour, Prof. Robert Ward, and Dr. Glenn Price for taking care of the unique music program on the campus and giving me unforgettable opportunities to perform piano concertos and chamber musics in many concerts. Special thanks to Pastor Jonghak Seo and Pasadena Lord's Church family for all the prayers and being a spiritual shelter for my family.

Finally I would like to dedicate this work to my family. To my parents and my sister for their endless love and support. To my little children, Philip, Isaac, and Johan, for making me happier than ever. And to my wife Junah, for being together with me always.

ABSTRACT

Twisted bilayer graphene around the magic angle has shown variety of correlated phases such as superconductivity, correlated insulators, and magnetism due to its flat band structure. The unconventional nature of the superconductivity and its possible relation to high temperature superconductors have sparked a lot of theoretical and experimental efforts to understand the properties of the magic angle twisted bilayer graphene. While electrical transport measurements revealed the interesting phases, spectroscopic understanding is strongly needed to connect the phases with theoretical calculations. We present the spectroscopic studies of gate-tunable magic angle twisted bilayer graphene using scanning tunneling microscopy. We report that the band structure is significantly modified even at charge neutrality due to exchange interaction. We apply a perpendicular magnetic field and develop a novel method that enables scanning tunneling microscopy to reveal Landau fan diagrams. We discover topologically non-trivial states appearing at finite magnetic field, and from spectroscopy we are able to identify the mechanism. Finally, we verify interaction driven band flattening experimentally in twisted bilayer graphene, which is responsible for creating strong correlations.

PUBLISHED CONTENT AND CONTRIBUTIONS

[1] Youngjoon Choi, Jeannette Kemmer, Yang Peng, Alex Thomson, Harpreet Arora, Robert Polski, Yiran Zhang, Hechen Ren, Jason Alicea, Gil Refael, Felix von Oppen, Kenji Watanabe, Takashi Taniguchi, and Stevan Nadj-Perge. Imaging Electronic Correlations in Twisted Bilayer Graphene near the Magic Angle. *Nature Physics*, 15:1174–1180, 2019. doi: 10.1038/s41567-019-0606-5.
Y.C. co-conceived the experiment. Y.C. co-performed the measurements. Y.C. made the samples. Y.C. co-performed data analysis. Y.C. co-wrote the manuscript with input from all authors.

[2] Youngjoon Choi*, Hyunjin Kim*, Yang Peng, Alex Thomson, Cyprian Lewandowski, Robert Polski, Yiran Zhang, Harpreet Singh Arora, Kenji Watanabe, Takashi Taniguchi, Jason Alicea, and Stevan Nadj-Perge. Correlation-driven topological phases in magic-angle twisted bilayer graphene. *Nature*, 589:536–541, 2021. doi: 10.1038/s41586-020-03159-7.
Y.C. co-fabricated samples and co-performed STM measurements. Y.C. co-analysed the data. Y.C. co-wrote the manuscript.

[3] Youngjoon Choi*, Hyunjin Kim*, Cyprian Lewandowski, Yang Peng, Alex Thomson, Robert Polski, Yiran Zhang, Kenji Watanabe, Takashi Taniguchi, Jason Alicea, and Stevan Nadj-Perge. Interaction-driven Band Flattening and Correlated Phases in Twisted Bilayer Graphene. *Nature Physics*, In press, 2021.
Y.C. co-fabricated samples and co-performed STM measurements. Y.C. co-analyzed the data. Y.C. co-wrote the manuscript with input from other authors.

[4] Hyunjin Kim*, Youngjoon Choi*, Cyprian Lewandowski, Alex Thomson, Robert Polski, Yiran Zhang, Kenji Watanabe, Takashi Taniguchi, Jason Alicea, and Stevan Nadj-Perge. Spectroscopy of strongly coupled superconductivity and electronic correlations in Twisted Trilayer Graphene. In preparation, 2021.
Y.C. co-fabricated samples and co-performed STM measurements. Y.C. co-analyzed the data. Y.C. co-wrote the manuscript with input from other authors.

TABLE OF CONTENTS

LIST OF ILLUSTRATIONS

Chapter 1

INTRODUCTION

1.1 Twisted bilayer graphene as a host for strong correlations

Strongly correlated phenomena have been one of the main questions in the modern condensed matter physics. BCS theory of superconductivity fails to predict properties of unconventional high-temperature superconductors, such as cuprates or iron-pnictides, where correlated electrons create not only superconductivity but also variety of ordered (or dis-ordered) phases like Mott insulators, charge or spin density waves, pseudogap, and so on. Correlated electrons in fractional quantum Hall states have led to the discovery of a fractional charge, and possibly fractional and non-abelian statistics.

Before utilizing all the interesting properties for real world applications, we physicists want to understand them better. We want to test our favorite theories from multiple cases and deduce which principle globally applies, to extract 'physics' out of them. The problem is, each testing ground has its own complications and limitations, and we do not have many.

That is why graphene and two-dimensional materials have quickly become one of the mainstreams. They have served as an alternative platform for probing two-dimensional physics which GaAs heterostructure and a few others have been exploring. Integer quantum Hall effect and fractional quantum Hall effect, the hallmarks of a great testing ground, have been observed [1–4].

While studying electronic correlations in two-dimensional materials in the context of fractional quantum Hall effect is an interesting direction, they actually have their unique way to realize strong correlations. Before directly going into that, let us first discuss in which system correlation of electrons become important.

Electrons in a material act as a result of the competition between repulsive Coulomb interactions among them and the kinetic energy given by the periodic potential from the underlying lattice, or band structure. When the Coulomb energy is relatively larger than the kinetic energy, roughly speaking, electrons in the system do not follow what the underlying lattice tells them, and make their own orders, resulting in interesting phases. In the case of fractional quantum Hall effect, it is the

high magnetic field that quenches kinetic energy and makes Coulomb interaction dominates.

The important question is then, how do we engineer a material that relatively minimizes the kinetic energy compared to the Coulomb interaction. Graphene seemed not to be an ideal material for this qualification since electrons in its Dirac cones have relatively fast velocities, $v_F \sim 10^6 m/s$. However, theorists considered a specific case where one graphene layer is on top of another graphene layer, slightly twisted, enabled by a unique property that two-dimensional materials make possible.

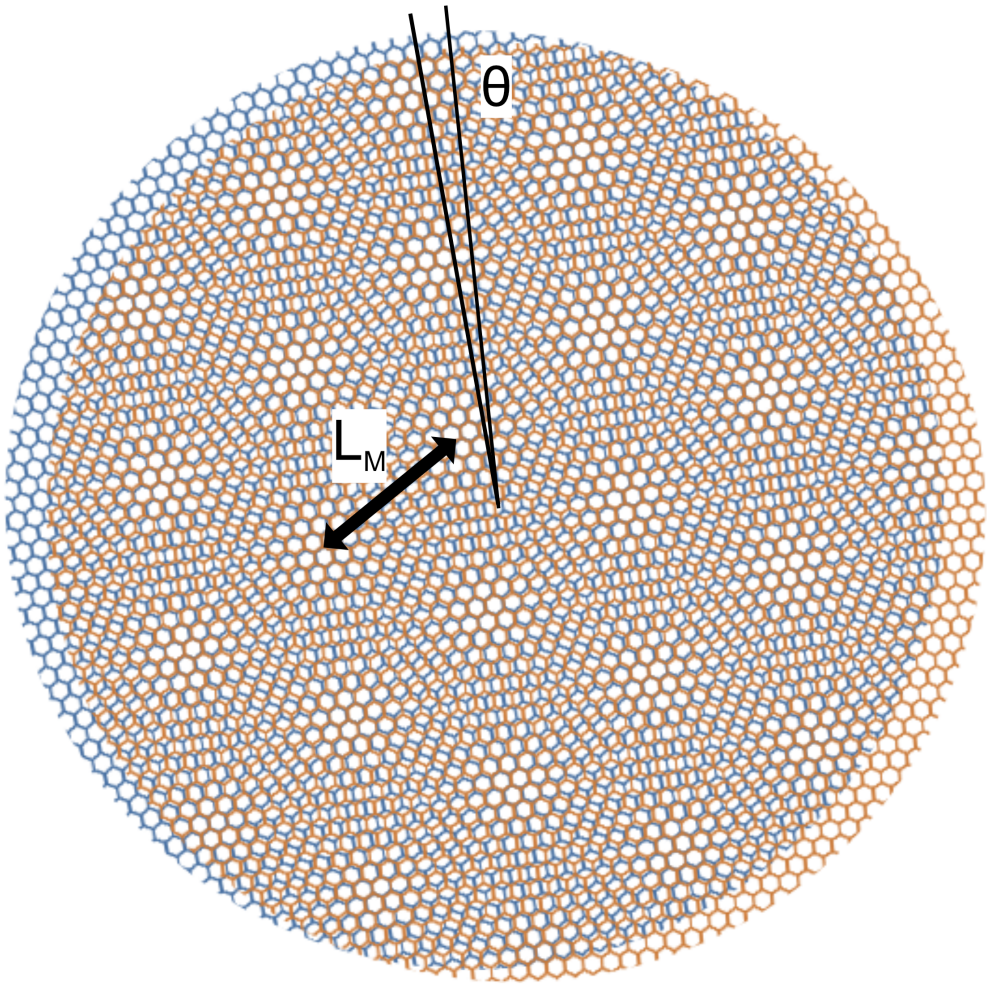

Figure 1.1: Moiré pattern in twisted graphene sheets.

When two graphene layers are stacked slightly twisted, they create a moiré pattern in real space, as shown in Fig. 1.1. The periodicity L_M is given by the twist angle

θ and the graphene lattice constant a, $L_M = a/(2\sin\theta/2)$. In the reciprocal space, since monolayer graphene has hexagonal brillouin zone with low energy Dirac cones at each vertex, two Dirac cones are slightly shifted by the twist of top and bottom layers (Fig. 1.2a). The Dirac cones are denoted as circles here. Since K and K' points are far enough when the twist angle is low, no scattering is assumed and it is safe to focus only on one valley. Figure 1.2b shows the low energy dispersion on one of the valleys (either K or K'). The points where energy crosses are the places where hybridization due to tunneling (or hopping) between two layers occur. Because of this hybridization energy gap opens at those points and the band closer to the zero energy becomes very flat (Fig. 1.2c). Flat band means low kinetic energy, so we now have a system where the kinetic energy is very small!

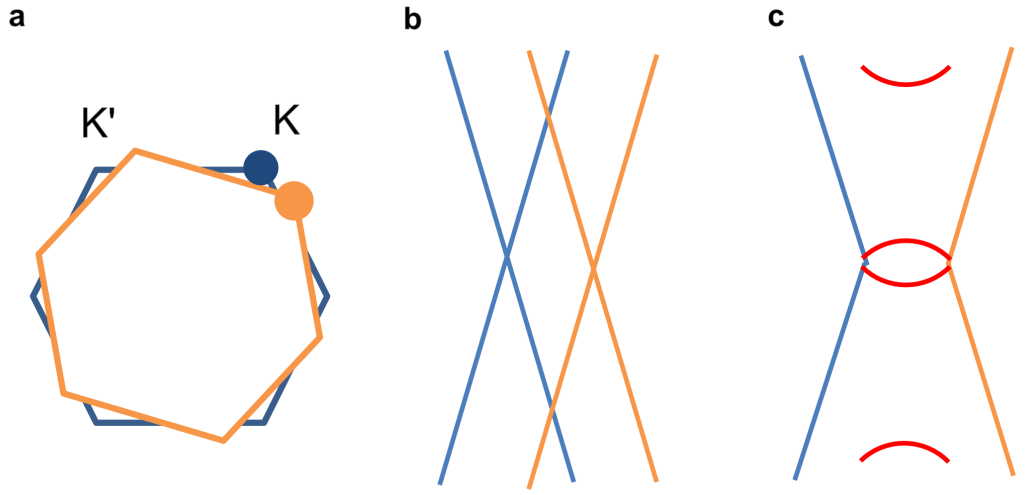

Figure 1.2: Engineering flat band. a) Twisted bilayer in reciprocal space. b) Two Dirac cones before hybridization. c) After hybridization, creating a flat band.

The explanation in the previous paragraph is first suggested and calculated in Ref. [5–7]. Detailed calculations found that around the twist angle of 1.1°, the bandwidth nearly vanishes (Fig. 1.3a) and the band velocity drops to zero (Fig. 1.3b) [7]. Since the Coulomb energy scale at this angle is roughly $U \sim \frac{e^2}{4\pi\epsilon L_M} \sim 30\, meV$ (L_M at this angle is about 13 nm), if the bandwidth W, which roughly is the scale of the kinetic energy, really goes to zero, U/W then become really big at this special angle, called the 'magic angle'. Large U/W would bring strong correlations in the system.

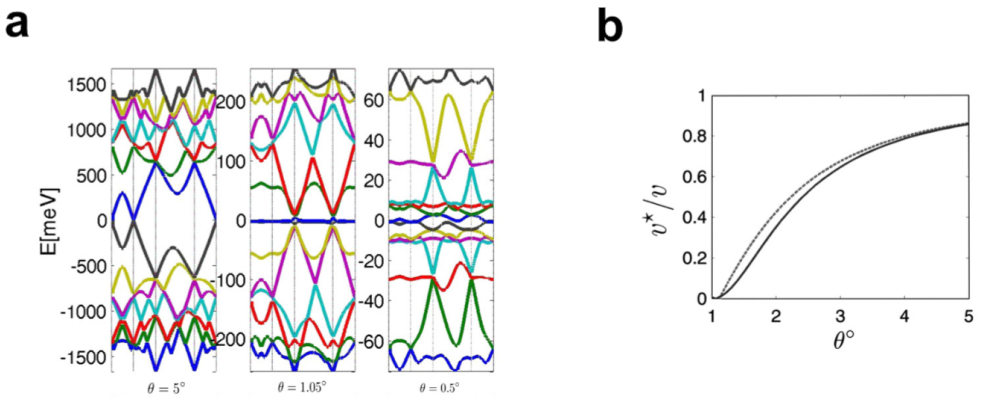

Figure 1.3: Calculated band structure of twisted bilayer graphene. a) Bandwidth becomes very small at $\theta = 1.05°$. b) Velocity drops to zero around $\theta = 1.1°$. Taken from [7], with permission.

1.2 Correlated insulating states and superconductivity

Following the theoretical predictions, experiments have been done aiming to target the magic angle. Controlling the twist angle with precision was the first challenge. Kim et al. and Cao et al. [8, 9] developed a tear-and-stack technique that enables the fine control of the twist angle. They prepared one sheet of monolayer graphene and picked up only half of the sheet with hBN. Then they rotated the remaining half manually by a desired angle, and picked it up to create the twisted bilayer graphene (TBG). Since the two graphene sheets came from the same crystalline graphene, their relative angle is now much more precise, compared to the case when the two sheets are from two individual graphene sheets that tried to align crystalline axes by optical means.

At $\theta = 1.8°$ [9], a low conductivity has been observed at charge neutrality due to the protected Dirac points, and also when four electrons are filled (or emptied) from the flat band due to the opening of gaps at hybridization points (Fig. 1.2c). Here degeneracy of four comes from two spins and two valleys (K and K' in Fig. 1.2a). However, no signatures of correlations were found because the angle is still not close enough to the magic value.

Finally, the magic angle device has been made. At $\theta = 1.08°$ [10], when two electrons are filled (or emptied) to the flat band, insulating states are surprisingly observed. Band structure calculation shows no sign of gaps inside of the flat band. Thus the only plausible explanation of this insulating behavior is correlation enabled

insulating states, similar to half filled Mott insulating states in a Hubbard model.

Moreover, resistivity suddenly drops to zero at low temperatures around this insulating states (Fig. 1.4) [11]. The zero resistance shows Fraunhofer pattern with magnetic field, confirming the state is indeed superconductivity, the critical temperature being around $T_c \sim 2\ K$ at the maximum. It is very unusual that at such a low carrier density of $n \sim 1.5 \times 10^{12} cm^{-2}$ (if counting from the $\nu = -2$ where the Fermi surface reconstructs, $n' \sim 1.5 \times 10^{11} cm^{-2}$, even smaller) the superconductivity arises.

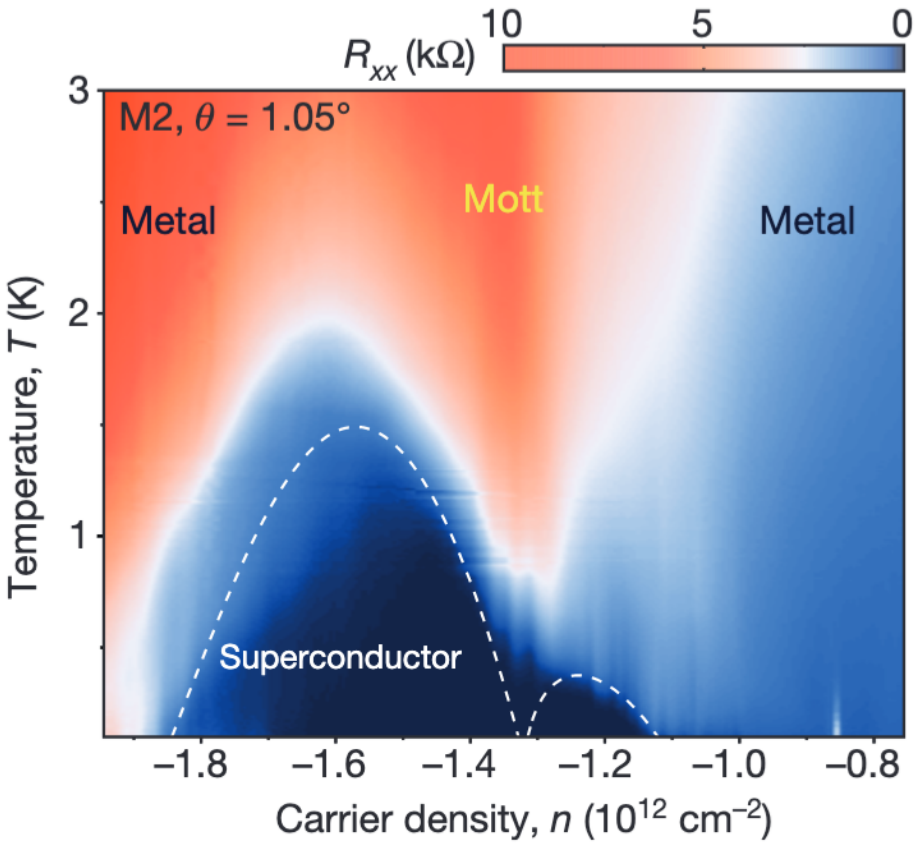

Figure 1.4: Superconductivity in twisted bilayer graphene. Taken from [11], with permission.

Strong correlations bring these unconventional superconductivity and insulating states. Similarity of the phase diagram to that of high temperature superconductors like cuprates, where doping antiferromagnetic Mott insulator causes superconductivity, has brought a lot of excitement to the field. Comparing to these previous

correlated materials with multiple components, TBG is much cleaner since carbon is the only component and it is easy to dope with electrostatic gating, not like introducing dopant atoms. This opens up a possibility to study a correlated material in a clean limit.

Soon after the report, Yankowitz et al. [12] applied high pressure to TBG at $\theta = 1.27°$ and reproduced superconductivity. Without applying pressure, the device was not superconducting. Pressure decreases the physical height separation between two layers and enhances the tunneling or hybridization. Therefore, band width become squished with high pressure, hence enhancing correlations. This experiment highlights that the observed superconductivity and insulating behaviors are indeed from flatness of the band and enhanced correlations.

1.3 Magnetism and topology

Strong correlations in the magic angle TBG (MATBG) also enable ferromagnetism to appear when the three electrons are filled in the moiré band [13]. A giant anomalous Hall effect is observed at low temperatures. Moreover, a similar kind of device, maybe slightly better quality, showed quantum anomalous Hall effect with Chern number 1 [14].

Quantum anomalous Hall effect has been observed only in a few materials. Also, in MATBG, the amount of magnetism exceeds the value considering only spins, signalling the magnetism is mostly orbital [15]. C_2T symmetry is believed to be explicitly broken in these devices since hBN is nearly aligned with the bottom graphene from optical means. Other devices that are not aligned and showed superconductivity have not shown this strong anomalous Hall effect. Due to the broken C_2T symmetry, a gap opens at the charge neutrality and somehow makes Chern number C= 1 state favorable at three electron fillings. MATBG is therefore a nice platform for understanding the interplay between strong correlation and topology.

1.4 Scanning tunneling microscopy on TBG

While transport studies have shown various interesting phases, spectroscopic studies are needed to investigate and support the physical mechanisms behind them. One tool might be angle-resolved photoemission spectroscopy (ARPES). ARPES has revealed band structures of interesting materials including recent discovery of topological materials [16]. However, the physics of MATBG is determined inside the energy scale of 10 meV below liquid He-4 temperatures, beyond the capability

of ARPES yet.

Alternatively, scanning tunneling microscopy (STM) can also reveal spectroscopy of a system. Atomically sharp metallic tip is placed on a material. When a bias voltage V is applied between the tip and the sample, tunneling current flows as soon as the distance between them is close enough. The tunneling current I is determined by the available states between them within the bias voltage. Since we choose the tip material to have flat density of states around the Fermi energy, the tunneling current is mainly determined by the integrated density of states in the sample. dI/dV then is proportional to the density of states itself. By measuring dI/dV changing V, STM gives local DOS as a function of energy.

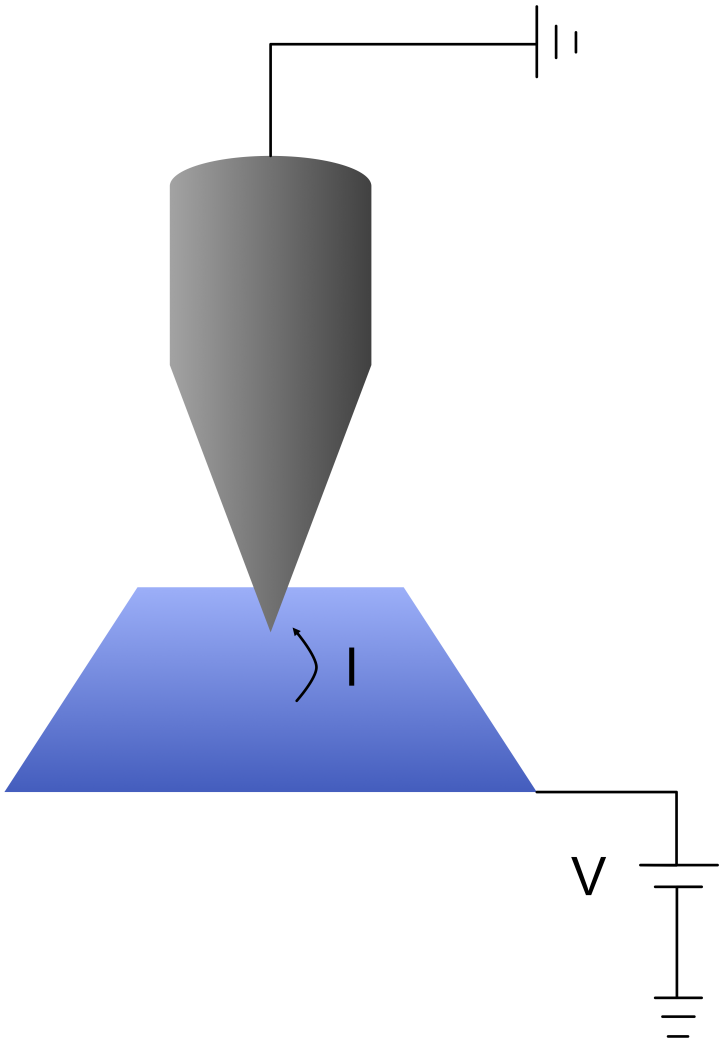

Figure 1.5: Schematic of STM.

Efforts to explore TBG with STM have been fruitful. At the initial stage, TBG appeared naturally and randomly on a surface of a cleaved graphite or on a graphene multilayers grown by chemical vapour deposition (CVD). Li et al. [17] found that strong enhancement of DOS occurs when the twist angle is around $\theta = 1.16°$ due to Van Hove singularities (VHSs) from the flat band. Brihuega et al. [18] systematically studied the evolution of the VHSs as a function of twist angle. They reported decreasing separations between two VHSs while decreasing the twist angle, following the theoretical expectations. However, due to the nature of the sample, changing the carrier density or doping was not possible.

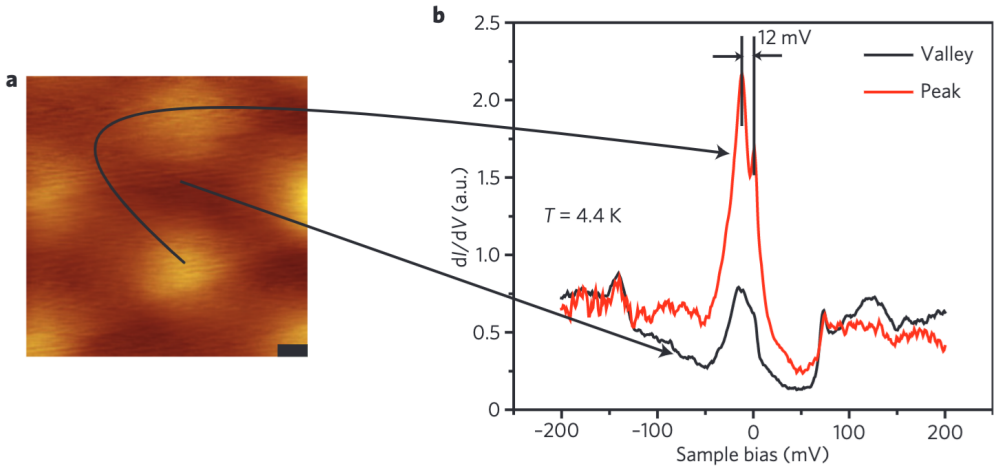

Figure 1.6: Observation of VHS in TBG at $\theta = 1.16°$. a) Moiré pattern. b) VHS is higher on the bright side in the moiré pattern. Taken from [17], with permission.

Wong et al. [19] and Kim et al. [20] tried to add gate tunability in TBG devices. They indeed were succesful on tuning carrier density in their devices. The VHSs move in energy according to the dopings. Unfortunately, the measurements were all done away from the magic angle. It seemed that controlling twist angle precisely to the desired value with gate tunability is difficult to achieve at the same time.

1.5 Outline

In Chapter 2, we will first discuss how we developed a new fabrication method to make gate-tunable TBG at the magic angle. We will show the topography and the moiré pattern, and reproduce the STM spectroscopies reported. Then, with our ability to tune the sample, we will show how VHSs evolve when there are strong

correlations. Due to the strong correlations, the VHS separation is significantly enhanced at the charge neutrality point, compared to when they are completely filled or emptied. We attribute the exchange interaction causing this phenomenon, by showing theoretical calculations incorporating the interaction. We will also discuss signatures of correlated insulators at integer fillings in our earliest samples.

In Chapter 3, with improved sample qualities, we will show cascade of phase transitions signalling flavor symmetry breaking in MATBG. With out-of-plane magnetic field, we observe Landau levels from the flat bands. To make a connection to transport experiments with magnetic field, we develop a novel technique that enables STM to plot Landau fan diagram. With this LDOS Landau fan diagram, we will show that topologically non-trivial states arise at finite magnetic field. Stoner instability explains the emergence of these Chern phases. By mapping the Chern phases continuously changing twist angles and dopings, we will draw a phase diagram of these phases, and the diagram corroborates the identified mechanism. We will discuss the possible band structures that are behind not-well-understood sequences of Landau levels at charge neutrality and try to rule out some of the possibilities.

In Chapter 4, we will further utilize the Landau levels to visualize the detailed band structure of TBG. At slightly larger twist angles, we will show that the electronic interaction already bends the band structrue significantly in the context of Hartree effect. The interaction-driven band bending causes flattening of flat bands, and amplifies DOS significantly. We attribute this amplification to the origin of strong correlations in MATBG. We show that the flattening of the band is responsible for the occurences of correlated insulating states or cascade of phase transitions. We also systematically study the effect of heterostrain in TBG to clarify the role of heterostrain and rule out this effect as a possible explanation for what we observe. This band flattening due to interaction clears up many discrepancies such as large band width still at the magic angle, inconsistent Fermi velocities, or large Van Hove singularity separations. It tells us the high DOS from a portion of the band structure determines the onsets of correlated phenomena in MATBG. Moreover, since this band deformation due to interaction is in principle applicable to other moiré materials, one should consider it when forming an idea of how a band structure looks and predicting properties of a moiré material.

In Chapter 5, we will conclude the thesis by showing our efforts to detect possible signals from the superconductivity. We will discuss interesting directions to identify superconductivity with our STM. We will talk about various other phases that can

also be observed in the STM. Not only TBG, but any fascinating two-dimensional materials can be investigated by the method we developed. We expect new phases will be explored with gate tunable STM devices in the near future.

Chapter 2

SCANNING TUNNELING MICROSCOPY ON GATE TUNABLE TWISTED BILAYER GRAPHENE

2.1 Two-dimensional materials probed by STM

Since the discovery of isolated monolayer graphene, two-dimensional materials have opened a new possibility to probe two-dimensional physics with STM. Traditionally, interesting two-dimensional physics, such as integer and fractional Quantum Hall effect, has been mostly studied in two-dimensional electron gas trapped in quantum well structures. These structures are not ideal for STM, since STM tip only measures the surface with the scale of $\sim 1\ nm$ where the tunneling current occurs.

Two-dimensional materials have emerged as an alternative playgrounds for interesting physics that require high-quality samples. These class of materials are crystalline and have few defects on its own. After the reports of integer Quantum Hall effect [1, 2] in monolayer graphene, the field has become one of the fastest growing subfields in condensed matter physics. The fabrication quality has grown rapidly and at cryogenic temeratures electrons move in the graphene device ballistically, mean free path exceeding $> 10\ \mu m$, only bound by the size of the device. Fractional Quantum Hall effect [3, 4] has been found, signalling that the materials host physics with electronic interactions as well.

In general, three different fabrication methods have been implemented to investigate two-dimensional materials with STM. One is to grow a monolayer on top of a preferred substrate in situ. Miller et al. grew graphene on top of SiC and observed nicely developed Landau levels and hence integer Quantum Hall effect [21]. Second method is to cleave highly oriented pyrolitic graphite (HOPG). On the surface of HOPG, occasionally there is a graphene on top of graphite, and the property of graphene is somewhat isolated from the properties of substrate graphite. Li et al. observed Landau levels from this graphene and they showed that the property is the same as isolated graphene. However, these two methods by their nature lack the ability to tune charge density by electrostatic gating, which has been one of the most powerful knobs in transport measurements.

The last method is to exfoliate a monolayer onto a substrate, similar to transport measurements. The electrostatic gating is utilized in this way. At the early stage

of this method, graphene on SiO_2 seemed to yield poor quality of Landau levels compared to grown graphene samples due to amorphous nature of SiO_2 surface and charge puddles [22]. Soon after the discovery of hBN as a clean substrate for transport measurements [23], STM devices have also been made with hBN substrate [24, 25], showing cleaner Landau levels [26] with gate tunability.

To fabricate these devices, exfoliated graphene on either SiO_2 or Poly(methyl methacrylate) (PMMA) is carried by a sticking PMMA layer, and is dropped on top of a substrate hBN with the PMMA layer. Then, PMMA on top of the device is cleaned by acetone and IPA, and typically annealed above 350°C in an Ar/H_2 environment, to make the device clean enough for tunneling measurements.

2.2 Fabrication of TBG device

TBG, however, has an intrinsic issue with previously developed fabrication methods. First, it is reported that annealing at high enough temperature (above 200°C), upper and lower layers relax to the lowest energy configuration, which is 0° rotated Bernal bilayer [10]. Methods including PMMA on top of sample, and annealing it above 350°C have high chance to mess up the twist angles.

Second, obviously, control of doping is necessary, which rules out the methods including cleaving of HOPG or growth based technique. Also, for the high quality device, it is better for TBG to be on the hBN, rather than on an uneven insulating substrate such as SiO_2.

Third, as discussed in Ch. 1.4, interesting phases such as superconductivity and correlated insulating phases only occur at very narrow angle range around 1°. Putting CVD grown graphene sheets on hBN randomly might yield gate tunable TBG device, but the angle ends up in a random value [19]. The only reliable way of getting the angle consistently around 1° is to use tear-and-twist method developed in [8, 9] so far.

To reconcile all the requirements, we developed a new fabrication method. First steps are identical to the tear-and-twist method. After picking up a 30- 50nm-thick boron nitride flake using Polydimethylsiloxane (PDMS) coated with a Poly(bisphenol A carbonate) (PC) polymer, the graphene is torn into two parts which were subsequently picked up while controlling the twist between the parts to be around 1° (Fig. 2.1a).

But after these steps, we modified the method to make an STM-compatible device. Detailed process is described in Fig. 2.2. PC film with the entire stack is manually

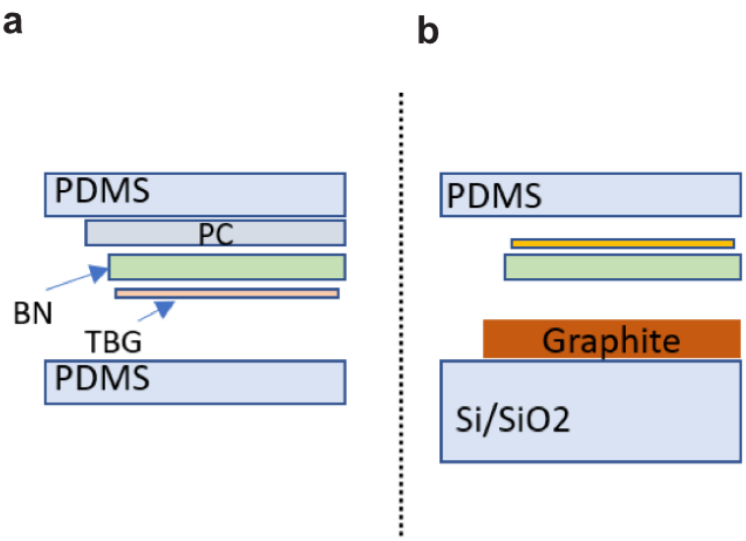

Figure 2.1: Flip-and-stack technique. a) Monolayer graphene is tear and picked up sequentially with hBN, with the twist angle around 1°. b) The stack is flipped using another PDMS and placed on a graphite gate.

peeled from the base PDMS and transferred onto a separate PDMS in order to flip the order of the layers . PC is dissolved in N-Methyl-2-pyrrolidone (NMP) a couple of times, each for around 5 seconds, until no PC and NMP residues are remaining on PDMS. We chose NMP instead of typically used Chloroform, since Chloroform significantly deforms PDMS and could damage flakes. Also NMP liquid tends not to stick to PDMS, making it easier to remove liquid residues on PDMS. hBN protects the desired sample from solvents.

Afterward the second PDMS with the inverted stack structure is transferred onto a prepared chip (silicon chip covered with 300 *nm* of silicon-oxide) with pre- patterned electrodes and a $\sim$ 10 *nm* thick metallic graphene multilayer that is used as the back gate (Fig. 2.1b). The twisted bilayer graphene (TBG) is then contacted to the gold electrodes using additional few-layer graphene contacts. During device fabrication special care is taken so that the temperature of the sample never exceeds 150℃ to

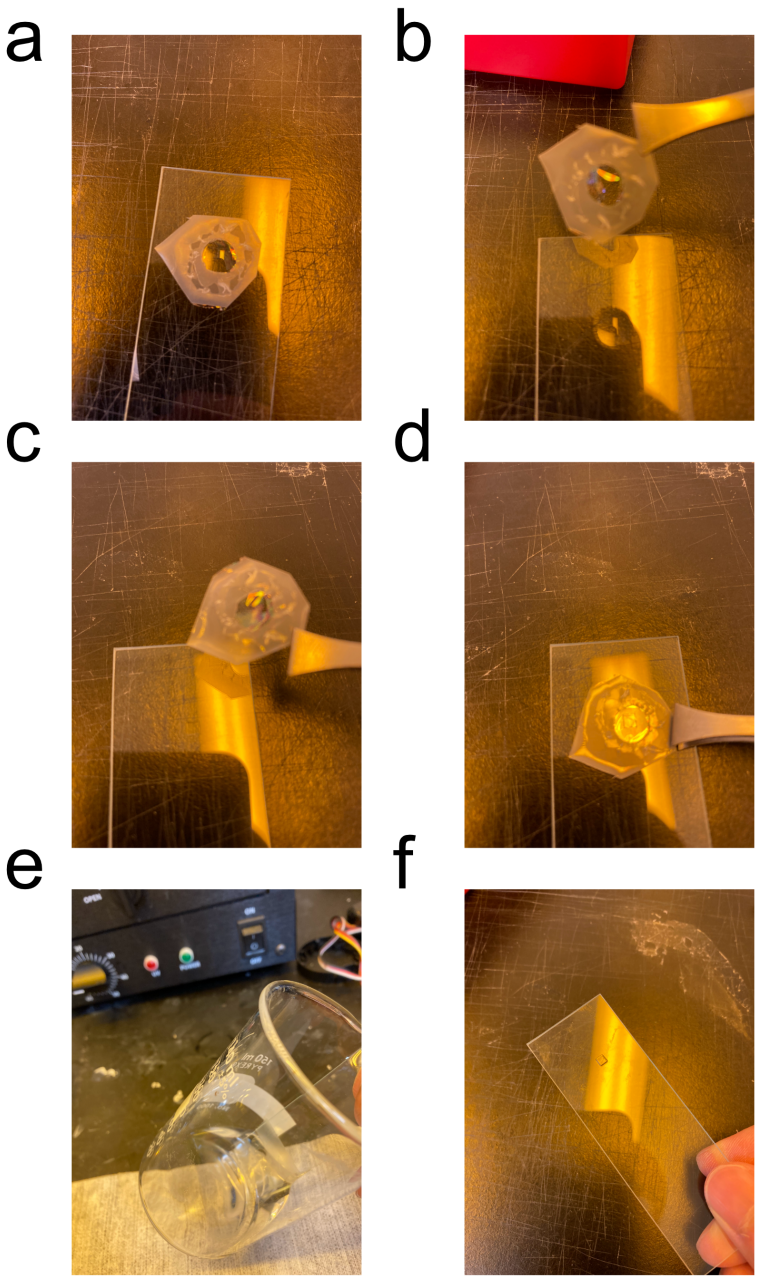

Figure 2.2: Flipping the stack on PDMS. a) The stack is on top of PC film. b) Manually lift the PC film from the base PDMS. c) Prepare another clean PDMS on a glass slide and manually flip the PC attached with tape. d) Carefully drop the PC without causing wrinkles or bubbles. e) Dissolve PC in NMP. f) Clean up tape residues. The resulting PDMS has flipped stack on top.

avoid untwisting of the TBG. With this method we obtain twist angle controlled, gate tunable TBG device. We easily find over 100 $nm \times 100\ nm$ area without signatures of dirts.

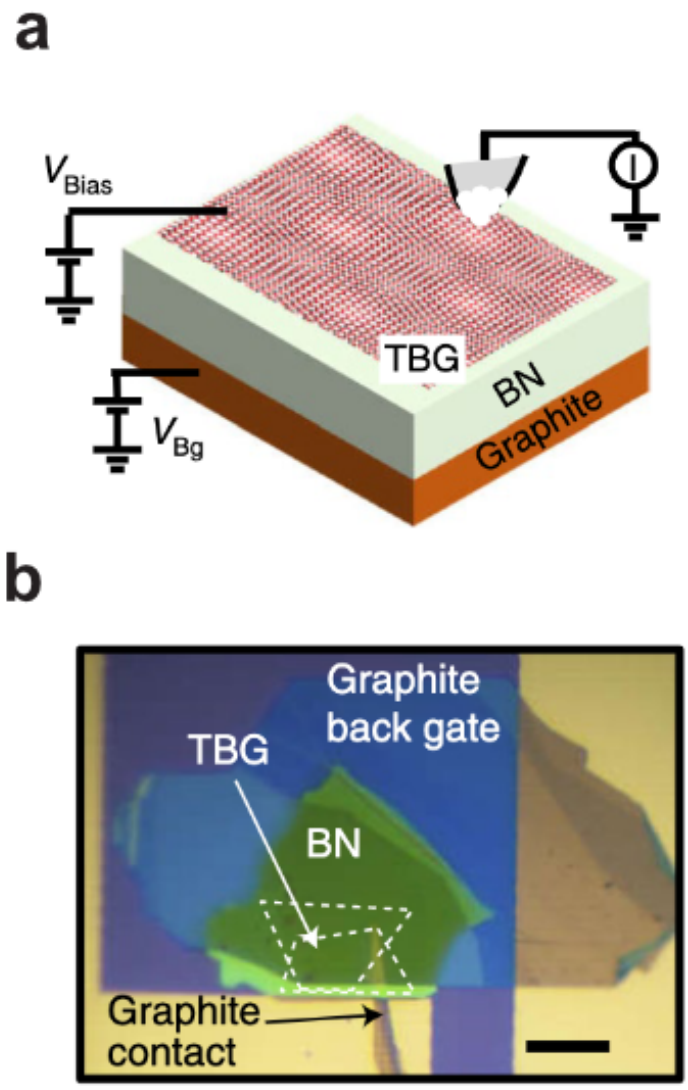

Figure 2.3: Device schematic and optical image. a) Device schematic. b) Optical image. Scale bar: 20 μm

The schematic of our measurement is shown in Figure 2.3a. TBG on top of hBN substrate is directly probed by STM tip. V_{Bias} is applied to the TBG, for spectroscopic measurements. V_{Gate} is applied to the graphite back gate, controlling the carrier

density. Using the graphite back gate instead of silicon gate beneath SiO_2, height corrogations as well as charge impurities are minimized. Figure 2.3b shows an optical image of a typical device.

2.3 Topography

When we measure topography by keeping tunneling current constant, the moiré lattice is clearly shown, where the wavelength is around 13 *nm* (Fig. 2.4a). As discussed in Chapter 1, AA stacked area has high LDOS, represented as high signals in topography, and AB stacked area has low LDOS. Atomic configuration of the AA and AB stacked region is illustrated in Fig. 2.4b. When we increase the resolution of the topography, we identify graphene lattice with wavelength of 246nm, agreeing with the lattice constant of graphene (Fig. 2.4c-d). In AB stacked region, the A graphene atom at the top is on top of the B graphene atom at the bottom, and the B atom at the top is not on top of anything. Therefore, it is likely that the A graphene atoms at the top are brighter than B graphene, so that only A atoms are visible on AB stacked region (Fig. 2.4c). However, in AA stacked region, both A and B atoms at the top are on top of the graphene atoms at the bottom. Therefore, both A and B atoms are visible (Fig. 2.4d). Our measurement temperature is usually 2 K, unless otherwise specified.

Since our STM topography is taken with constant current mode, high density of states yield higher topographic profile. Note that the resulting topography is not an actual height of the sample. The measured corrugation between AA and AB/BA can be ranging from 0.1 *nm* to 0.3 *nm*, depending on how much of LDOS is in between the bias and the fermi energy. To get a true topography due to atomic corrugation, one should tune the gate voltage to place the AA concentrated LDOS away from the bias window. However, with our gate range, even dispersive bands have some distribution centered around AA and we cannot get rid of it completely. We are able to lower it as low as 0.1 *nm*, hence the physical corrugation is less than this value. This issue sometimes complicates the spectroscopic mapping.

We can measure the moiré wavelengths in all three directions, and typically they are not equal. The main source is coming from heterostrain of the two layers, the relative strain in upper and lower layer. A small amount of strain in one of the layers can cause significant distortion in moiré lattice [27]. Assuming only one layer is slightly stretched [28] and with the inputs of three moiré wavelengths, we can identify the twist angle, as well as the amount of heterostrain. Our samples give

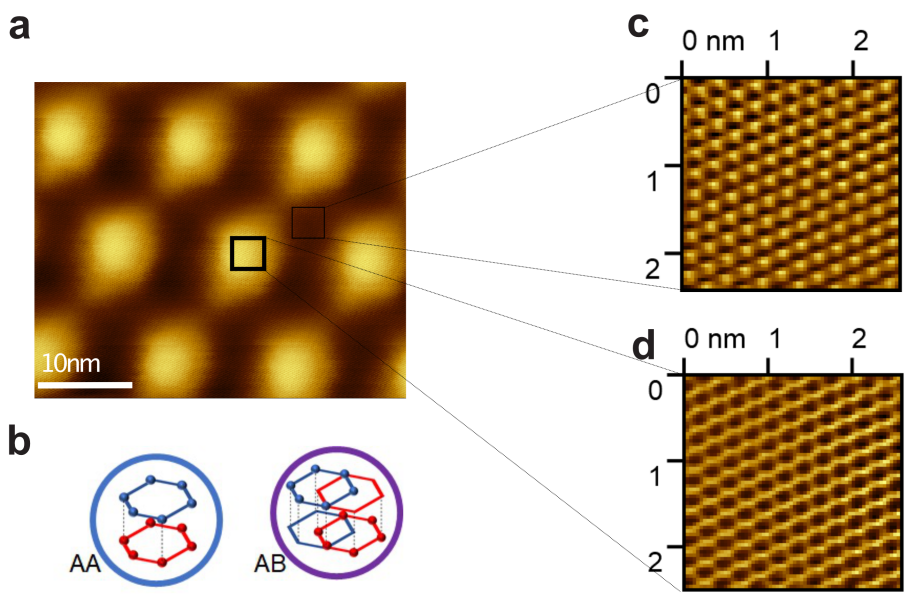

Figure 2.4: Moiré lattice and stacking configurations. a) Moiré lattice with twist angle around 1.1°. Typical tunneling parameters are : $I = 30\ pA$, $V_{Bias} = \pm 100\ mV$, $V_{Gate} \sim 0\ mV$. b) Atomic configurations of AA and AB stackings. c,d) High-resolution topography around AB and AA regions, respectively.

an average around $0.1 - 0.3\%$ of strain. This method gives a much more precise value of twist angles than the ones measured in transport, which we will discuss further in Chapter 3. STM is the most accurate way to measure local twist angle and the level of strain in TBG.

2.4 Point spectroscopy

We now want to discuss the band structure of TBG using the spectroscopic ability of STM. According to the calculations discussed in Chapter 1, two Van Hove singularities (VHSs) are present in TBG near the small angles. Indeed, spectra taken at the small angles ($\theta < 3°$) at a fixed gate voltage all show two sharp peaks above and below the Fermi energy at charge neutrality point (Fig. 2.5). We take the spectra on an AA site since the VHSs are most pronounced on an AA site due to the LDOS concentration. Also, as the twist angle decreases from $\sim 3°$ to $1°$ close to the magic angle, the separation of the two VHSs decreases as well from $\sim 400\ meV$ to $\sim 30\ meV$, consistent with the theoretical calculations and previous experiments [18, 19].

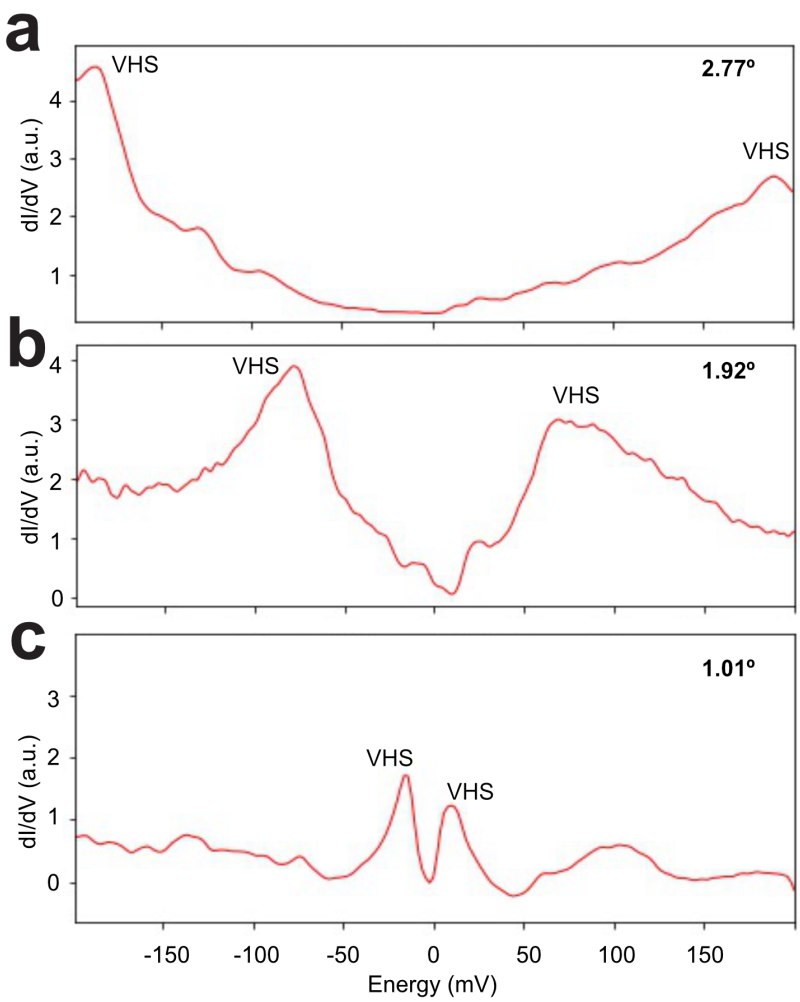

Figure 2.5: Point spectroscopy and VHS on an AA site. a) $\theta = 2.77°$. b) $\theta = 1.92°$. c) $\theta = 1.01°$. Tunneling parameters : $I = 50\ pA$, $V_{Bias} = -200\ mV$, $V_{Gate} \sim 0\ mV$.

2.5 Evolution of point spectrum with doping

At slightly different gate voltages (V_{Gate}) around the charge neutrality point, Figure 2.6 shows the doping dependence of the observed point spectra for the non-magic twist angle $\theta = 1.92°$ (an AA site). The two peaks in the local tunnelling density of states (LDOS) are again identified as VHSs separated by approximately 150 meV. Changing the position of the Fermi level relative to the VHS via the back gate shifts the positions of the two peaks in bias voltage but leaves their separation and overall line shape approximately unchanged. This is consistent with a simple band-structure picture.

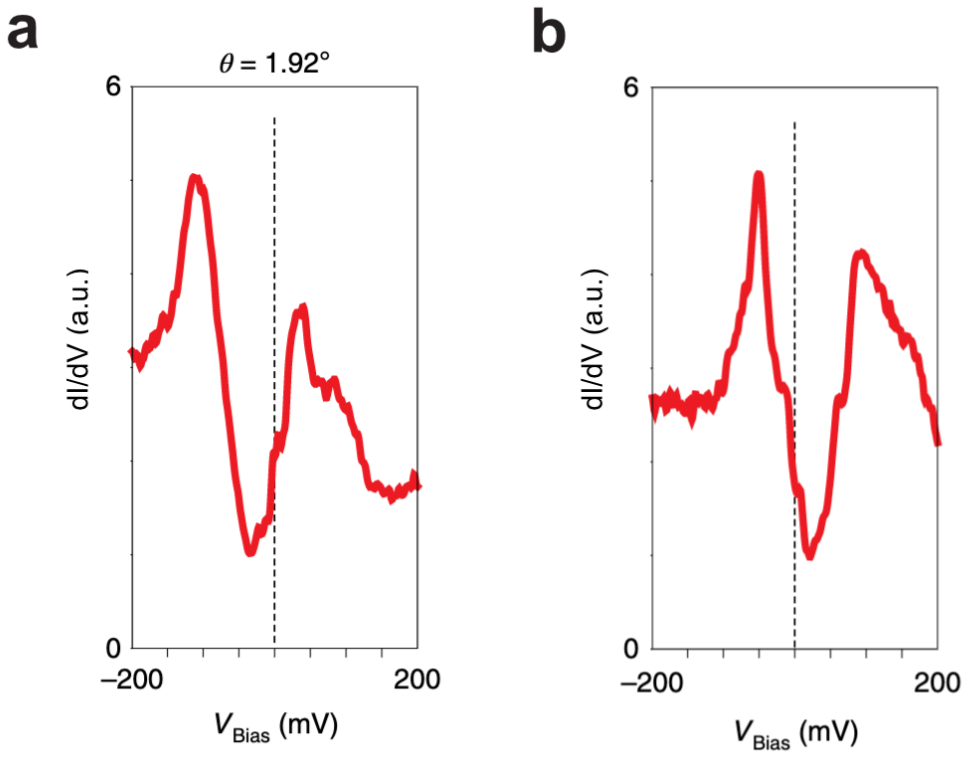

Figure 2.6: Point spectra at different gate voltages with $\theta = 1.92°$. a) $V_{Gate} = -0.6\,V$. b) $V_{Gate} = -4.6\,V$.

However, for regions near the magic angle ($\theta = 1.01°$), the observed spectra differ qualitatively (Fig. 2.7). Here, the overall shapes of the peaks change as they approach the Fermi energy ($V_{Bias} = 0mV$). When the upper VHS is closer to the Fermi energy, the upper VHS is much sharper than the lower VHS (Fig. 2.7a). On the other hand, when the lower VHS is closer to the Fermi energy, the lower VHS is much sharper than the upper VHS (Fig. 2.7a).

To visualize how the VHSs evolve with doping, we continuously plot the spectrum as a function of gate voltage, or doping (Fig. 2.8a). We compare the observed evolution with the schematic of the TBG band structure at small angles (Fig. 2.8b). When the flat bands sit below the Fermi level and the remote band is at the Fermi level ($3.8\ V < V_{Gate} < 10\ V$, green region in Fig. 2.8), the completely filled flat bands shift linearly as V_{Gate} is reduced. The slope of $\Delta V_{Gate}/\Delta V_{Bias} \approx 1\ V/5\ mV$ is directly proportional to the density of states $\Delta n/\Delta\mu$ at the Fermi level in the regimes (with n being the carrier concentration and μ the chemical potential). When the

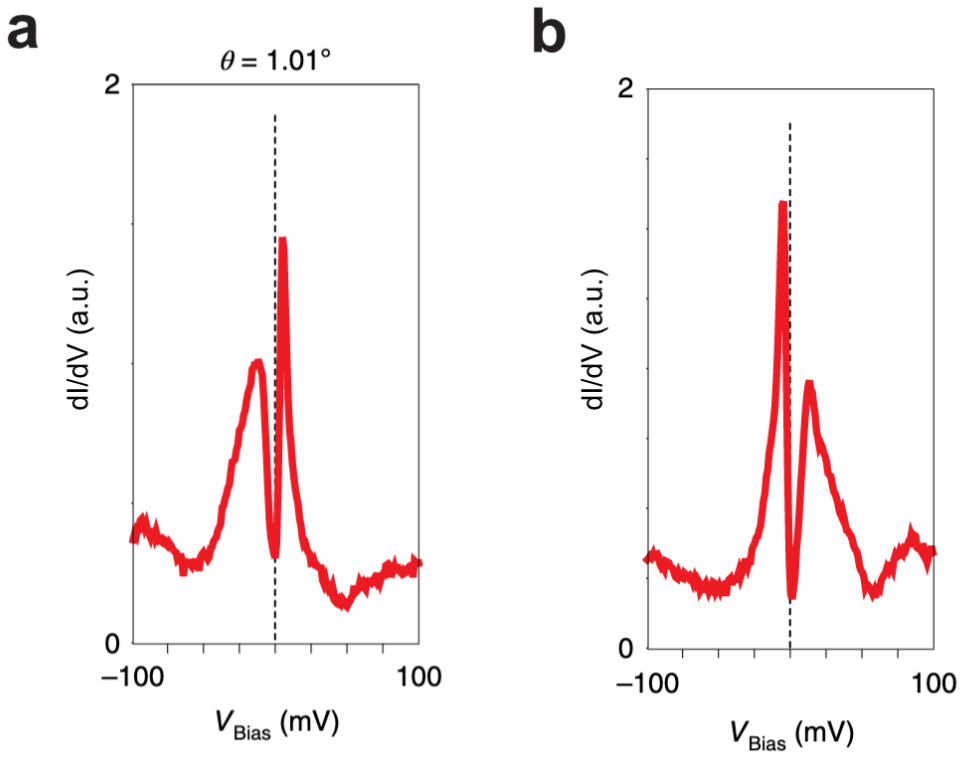

Figure 2.7: Point spectra at different gate voltages with $\theta = 1.01°$. a) $V_{Gate} = -0.7\,V$. b) $V_{Gate} = -3.6\,V$.

DOS is high, the slope $\Delta V_{Gate}/\Delta V_{Bias}$ is large as substantial changes in the back-gate voltage are needed to shift the chemical potential. In the opposite limit, when the Fermi level passes through a gapped region, the slope $\Delta V_{Gate}/\Delta V_{Bias}$ is close to zero since the DOS is very low. The linear shift of the peaks for the green region indicates a nearly constant DOS as expected when the Fermi level is located in the remote band (the green region).

The slope is reduced in the gate range $2.7\ V < V_{Gate} < 3.8\ V$ (the orange region) just before the flat bands start to cross the Fermi level. This observation indicates the existence of a gap between the flat and the upper remote band, of approximately $25\ meV$ according to the total shift in the chemical potential over the orange region. We also find that the gap decreases for smaller twist angles (Fig. 2.9) as predicted theoretically [29]. The extracted gap values strongly suggest that the additional remote bands will become increasingly important and contribute to the transport as the twist angle drops below 1°.

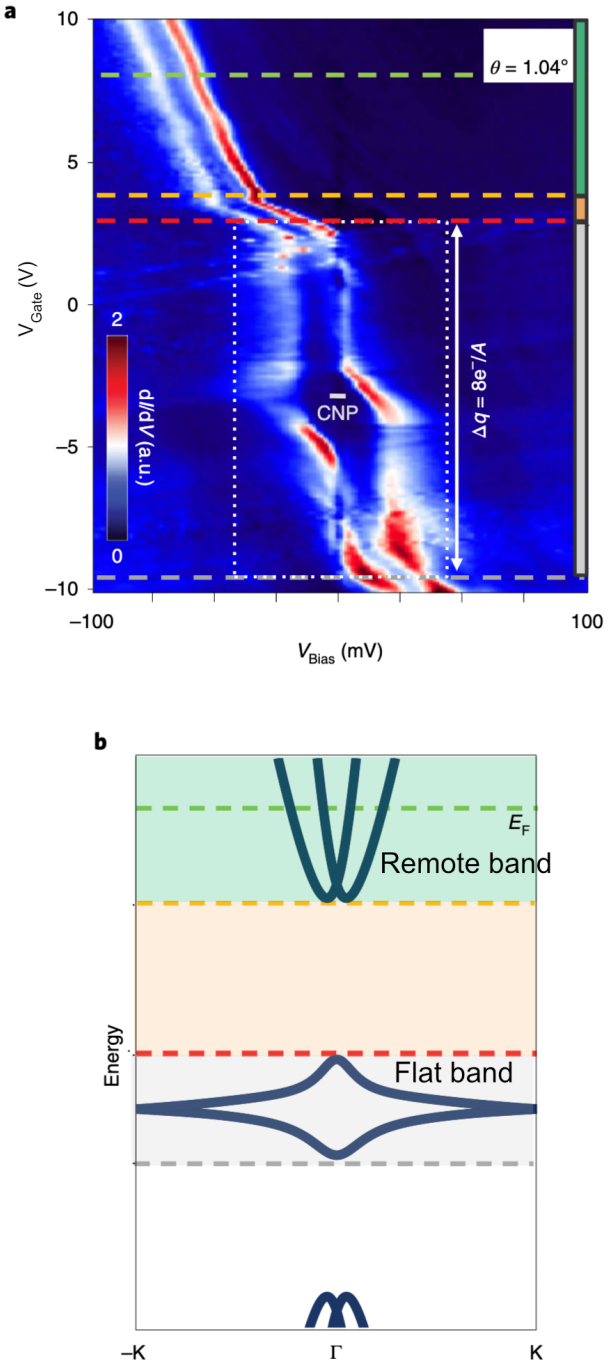

Figure 2.8: Evolution of the spectrum with doping at $\theta = 1.04°$. a) Gate voltage dependence of point spectra. b) Schematic band structure.

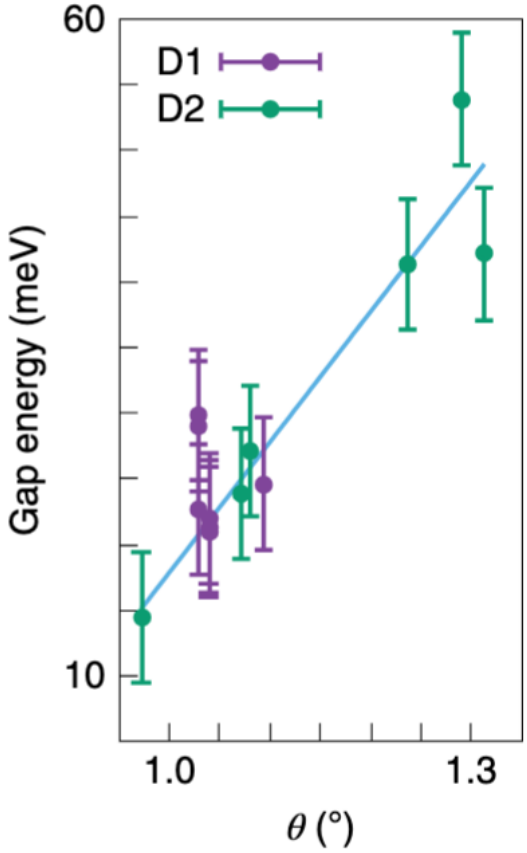

Figure 2.9: Flat band—remote band gap energy as a function of twist angle. The gap decreases linearly around the magic angle. The data is taken from two devices, D1 and D2.

For $-9.5\ V < V_{Gate} < 3\ V$ (Fig. 2.8, the grey region), the bands become distorted due to electronic correlations. We observe several suppressions of the LDOS at the Fermi level, and the slope $\Delta V_{Gate}/\Delta V_{Bias}$ changes repeatedly. First, the slope is large as the upper flat band, with its large DOS, crosses the Fermi level ($-1\ V < V_{Gate} < 2.7\ V$). In this region, suppressions of the LDOS near the Fermi energy are observed, indicating correlation driven gapped states. As the upper flat band is depopulated, the slope $\Delta V_{Gate}/\Delta V_{Bias}$ of the upper VHS peak decreases, while the slope of the lower peak barely changes, enhancing the apparent splitting between the upper and lower flat bands. At $V_{Gate} \approx -3.2\ V$, the charge neutrality point (CNP) is reached. As V_{Gate} is reduced further, the splitting between the LDOS peaks is gradually reduced and then the peak corresponding to the lower flat

band passes through the Fermi level. Again, when the lower flat band is partially populated, signatures of correlation driven gapped states are present at the Fermi energy.

The total range of $\Delta V_{Gate} \approx 13 \pm 1\ V$ (the grey region) over which the two flat bands cross the Fermi level is expected to change the charge density by $\Delta q = 8e/A$ (A is the measured area of this moiré unit cell), corresponding to filling of the two bands by a total of 8 electrons per moiré unit cell. This matches the change in charge density extracted experimentally based on the gate capacitance for a hBN thickness $d = 40\ nm$, as measured by atomic force microscopy (AFM), and dielectric constant $\epsilon \approx 3$. The relation between the V_{Gate} range and a density change of 8e/A is accurate to within 10% and allows us to determine V_{Gate} values corresponding to fractional fillings of the flat bands. We will improve this method of assigning filling factors in the later chapters.

2.6 Interaction effect at charge neutrality point

One of the surprising results of the doping dependence of the spectrum is the enhanced splitting between LDOS peaks (VHSs) around the CNP compared with the splitting when the flat bands are fully occupied (Fig. 2.10a). The peak separation in the red curve (fully filled) is much smaller than the peak separation in the blue curve (CNP). Moreover, this enhancement seems to be strongest around the magic angle (Fig. 2.10b). Away from the magic angle, the peak separation is nearly constant with doping. However, when the angle approaches 1.1°, there is a huge enhancement Δ_{PP}, defined by the difference between the separation at the CNP and at the fully filled case. This enhancement stands out at higher energies from the Fermi energy, hence has not been reported in transport measurements, which are only sensitive to energy scales of a few meV from the Fermi level. We claim that this effect is due to electronic interaction, and it is remarkable that the interaction effect is not only present at half fillings of the flat band, but also very strong at the CNP. To rule out trivial origins of the enhancing VHS separation, we later systematically consider the effect of heterostrain in Chapter 4. As expected from some theoretical calculations, the heterostrain could impact the VHS separation [30]. However, the huge amount of enhancement is not consistent with the heterostrain, especially the doping dependence.

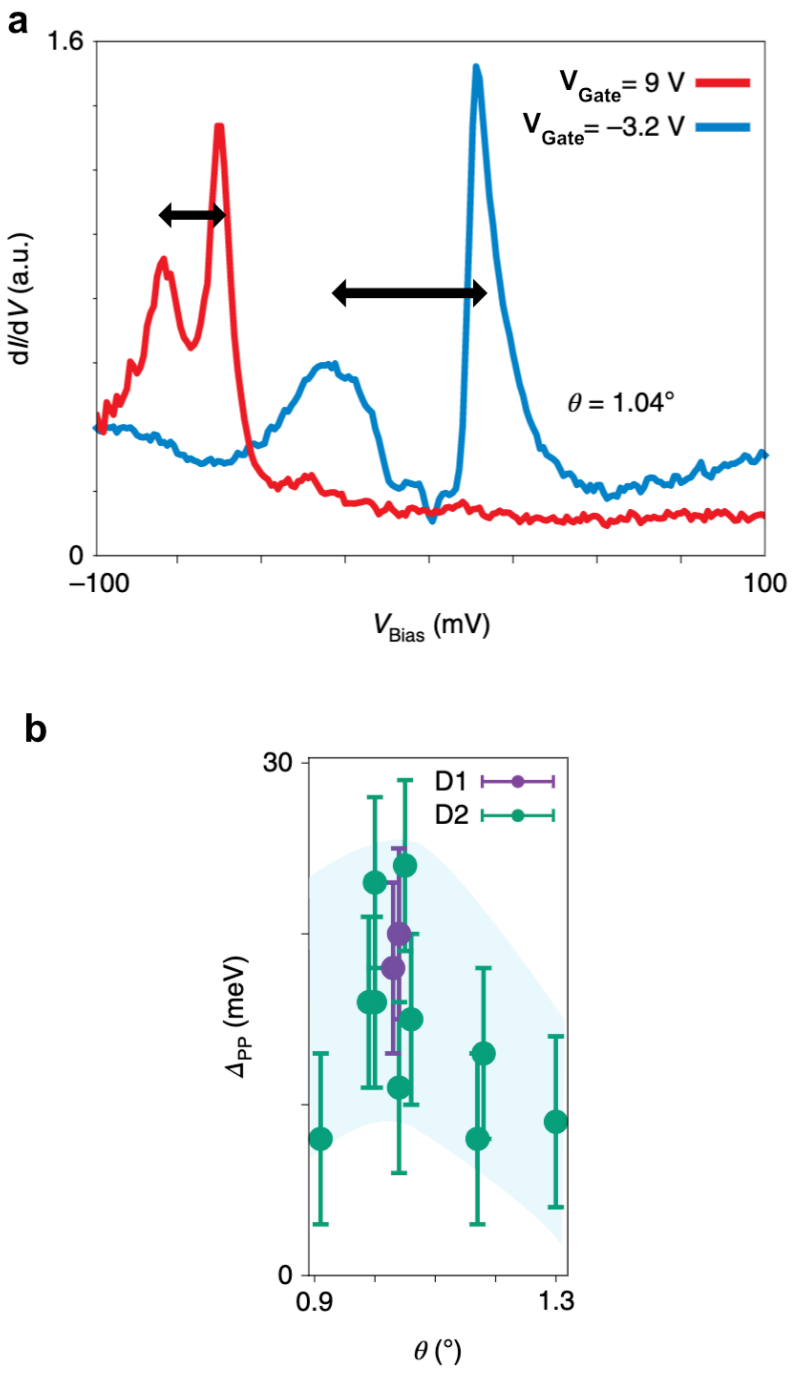

Figure 2.10: Enhancement of VHS separation at CNP. a) Red : when the flat bands are fully filled. Blue: at CNP. b) The enhancement is maximal around the magic angle.

2.7 Exchange interaction as theoretical explanation

Exchange interactions are a plausible origin of the enhanced splitting at the CNP in analogy with Quantum Hall ferromagnetism [31]. In this scenario, the strong exchange interaction maximizes the separation between the bands when one of the flat bands is completely filled and the other completely empty. Two important differences distinguish TBG from quantum Hall systems. First, no external magnetic field is needed as flat bands are already present at zero field; and second, the exchange interaction may not open a hard gap. Certain points in the Brillouin zone (away from the flat regions of the band causing the VHS) can remain gapless as a result of preserved symmetries [32, 33].

We support this interpretation by calculations within the framework of a ten-band model for TBG developed in Ref. [34]. While several effective models were proposed as starting points for studying TBG with and without interactions [35–39], the ten-band model captures the non-interacting band structure of magic-angle TBG while going beyond the flat bands and incorporates all relevant symmetries. Although its overall bandwidth for the flat bands and the VHS peak splitting ($7\ meV$ and $1mV$, respectively) are small compared with our observations, the model provides qualitative guidance on interaction effects, including broken symmetries. To account for interaction effects, we have added a symmetry-preserving short range interaction of strength E_c and solved the model self-consistently within mean-field theory assuming that the symmetry between the four flavours (spin and valley) remains unbroken. We find several nearly degenerate broken-symmetry states. The solution breaking C_3 symmetry qualitatively reproduces the observed splitting near the CNP (Fig. 2.11). Other features such as the overall broadening of the bands near the CNP are also qualitatively captured. The resulting solution shows that the peaks in the local density of states (LDOS) are split by an amount set by E_c. For $1 < E_c/W < 2$, with W being the bandwidth of the non-interacting model, the relative increase in the splitting matches well with our experimental observations (Fig. 2.11). The C_2T symmetry broken solution creates a hard gap, which we don't see in the experimental spectrum.

The competitive energy of the C_3 breaking solution suggests a high susceptibility towards nematicity [40, 41]; effects such as sample strain and unaccounted electronic correlations can plausibly stabilize this order as the unique ground state. Figure 2.12a shows the corresponding band structure across the Brillouin zone, with the Dirac cones protected by C_2T symmetry as indicated by the black dots. Broken C_3

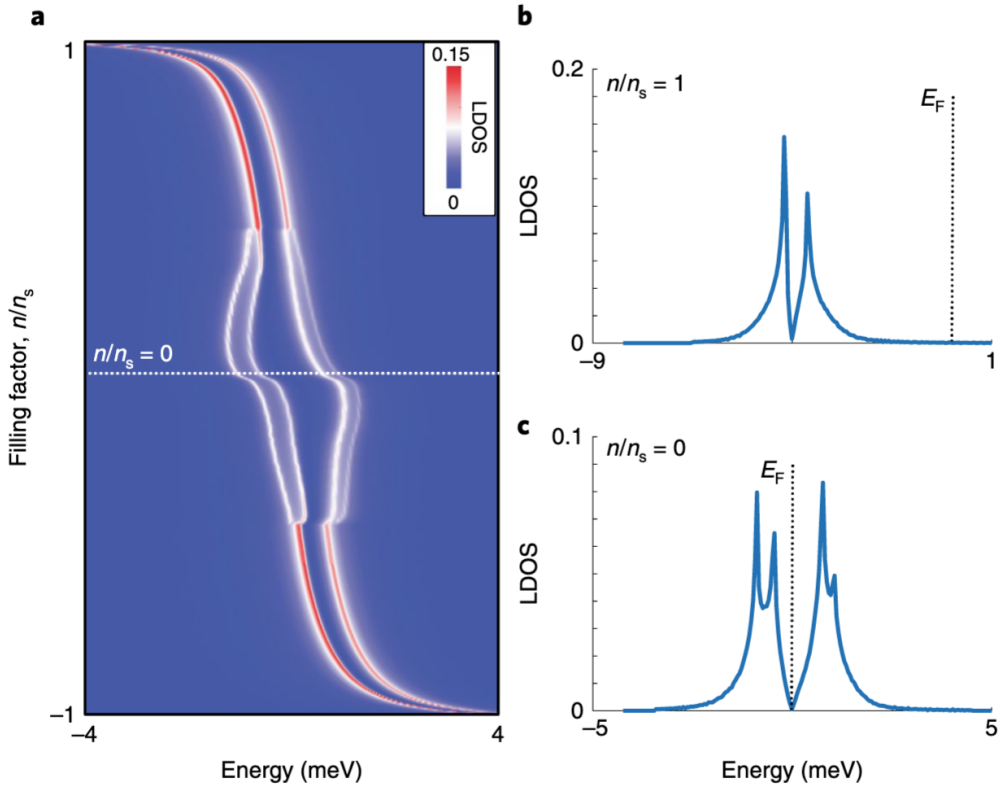

Figure 2.11: Simulated evolution of VHSs with C_3 symmetry broken solution. a) Evolution of VHSs. b) At full filling, the separation is small. c) At CNP, the separation is large due to interactions.

symmetry as a function of doping is clearly visible in Figure 2.12b.

Moreover, the model predicts that the spatially varying breaking of the C_3 symmetry is most pronounced in the LDOS at the domain walls connecting different AA sites for energies close to VHS peaks, as calculated in Fig. 2.13.

Consistent with these theoretical findings, spatially resolved LDOS maps taken on sites within the most C_3 symmetric moiré regions (from topography) show anisotropic LDOS profiles near the CNP (Fig. 2.14). The most pronounced domain-wall direction changes depending on whether V_{Bias} is adjusted to probe the lower or upper VHS as expected from the model calculations (Fig. 2.13). At full fillings, however, the anisotropy significantly reduces. We argue that the interaction plays a significant role in additionally breaking rotational symmetry on top of strain.

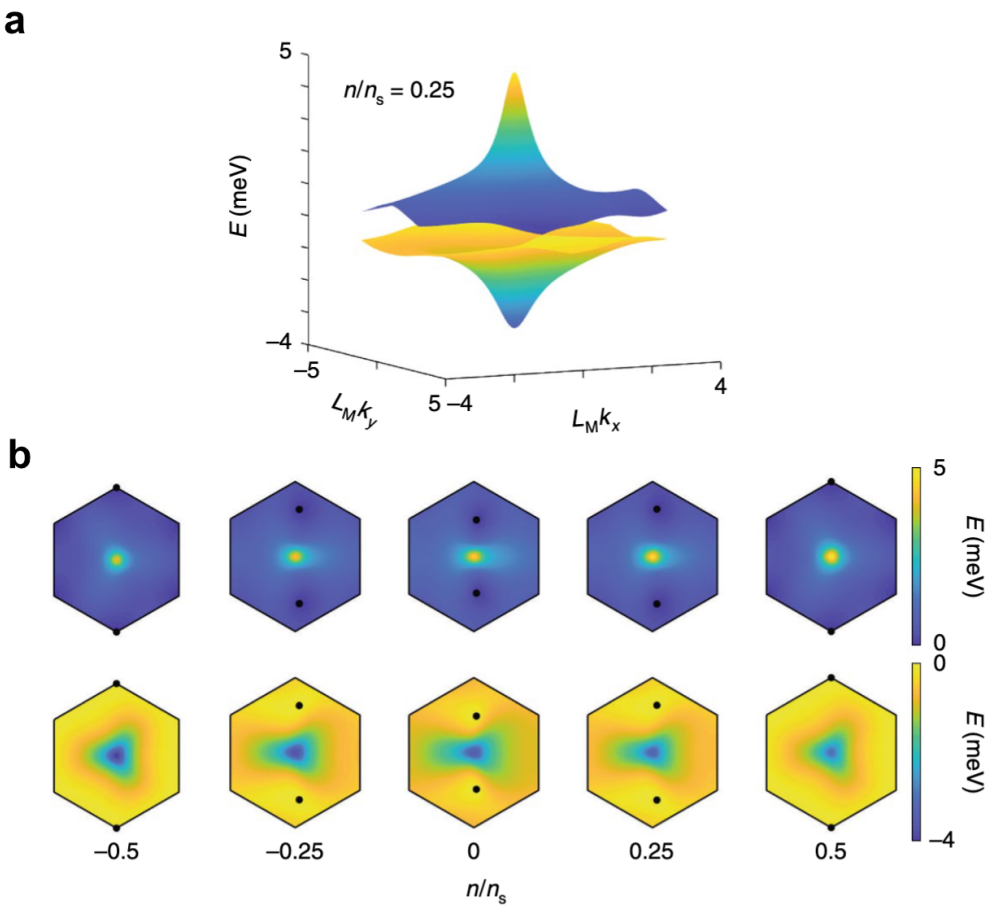

Figure 2.12: Band structure with C_3 symmetry breaking. a) The band structure. b) Dirac points are shifted from K points and create breaking of C_3 symmetry as a function of doping.

2.8 Signatures of correlated states at integer fillings

Finally, we focus on the states near half-filling of the flat bands where correlated insulating states and superconductivity were found in transport [10, 11]. Figure 2.15 shows two point spectroscopies at electron side half filling and hold side half filling for a moiré site with a local twist angle $\theta = 0.99°$. A suppression in the LDOS at the Fermi energy is observed near half-filling both for electrons and holes, which signals the emergence of correlated gaps. The gap values between 4 and 8 meV are measured, which are higher than the values extracted from thermal activation in transport experiments [10, 12]. In Chapter 4, with better quality of samples and tips, we showed that the gap values are actually around 2 meV at the maximum. The difference may be caused by tip induced quantum dot charging energies.

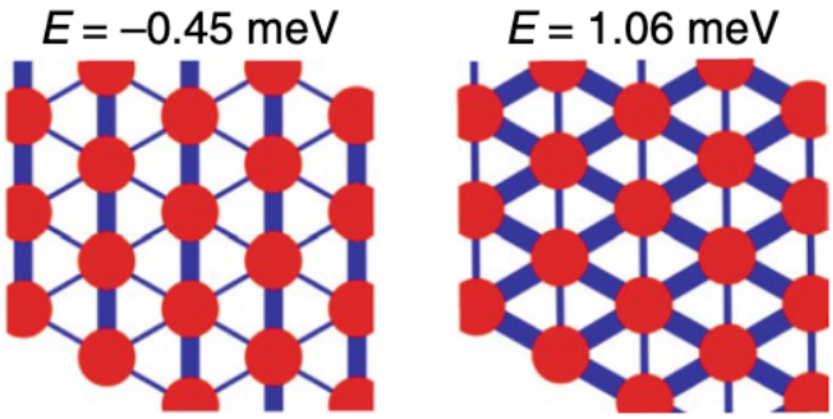

Figure 2.13: Effect of C_3 symmetry breaking in real space at CNP. Domain wall brightness or LDOS changes depending on the energy.

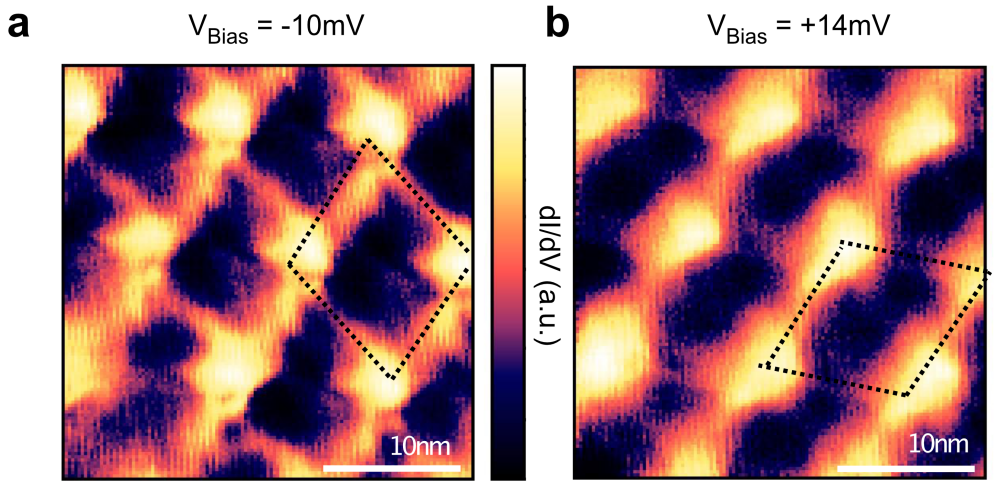

Figure 2.14: dI/dV map at CNP, showing C_3 symmetry breaking. a) $V_{Bias} = -10mV$. b) $V_{Bias} = +14mV$. Domain wall brigntness changes with energy in different directions.

To make a connection to transport experiments and better resolve the dependence on the filling of the flat band, we plot the zero-bias LDOS as a function of V_{Gate} in Fig. 2.16. The trace shows minima at charge neutrality and fully filled region, which is expected since there are low DOS in those regions (blue and gray regions). The trace

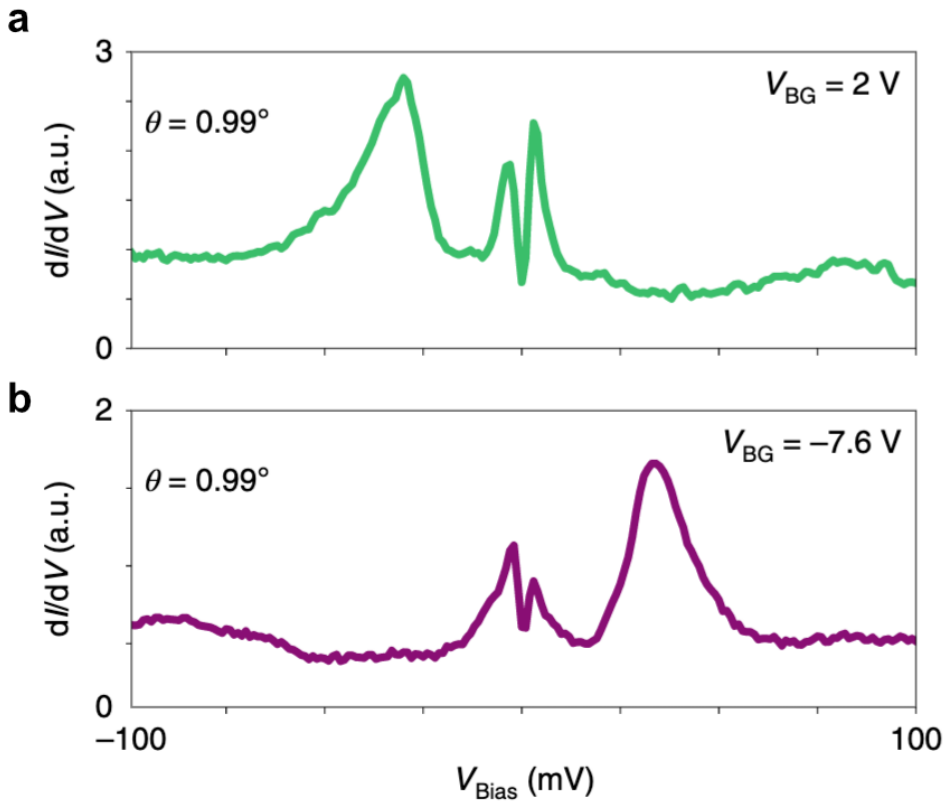

Figure 2.15: Spectra at half fillings at $\theta = 0.99°$. a) Electron side. b) Hole side.

also shows local minima of the zero-bias LDOS for half-filling of the flat bands, consistent with correlated ground states at these fillings (green and pink regions). The observed gaps typically occur near half-filling, although they are sometimes offset, presumably due to local electrostatic disorder, strain, or tip-related effects. Occasionally, the less-developed states at one-quarter and three-quarter filling may also be resolved. These observations strongly indicate that the measured gaps originate from correlated states at commensurate fillings and are distinct from other effects such as the Coulomb gap [42] that can also suppress the LDOS near the Fermi level in two dimensional systems with strong electronic correlations [22, 43–47]. In Chapter 3, we utilized this new type of measurement in STM to obtain LDOS Landau fan diagram. In Chapter 4, with better quality samples and tips, we are able to find these correlated gaps almost exactly at integer fillings, consistent with transport experiments.

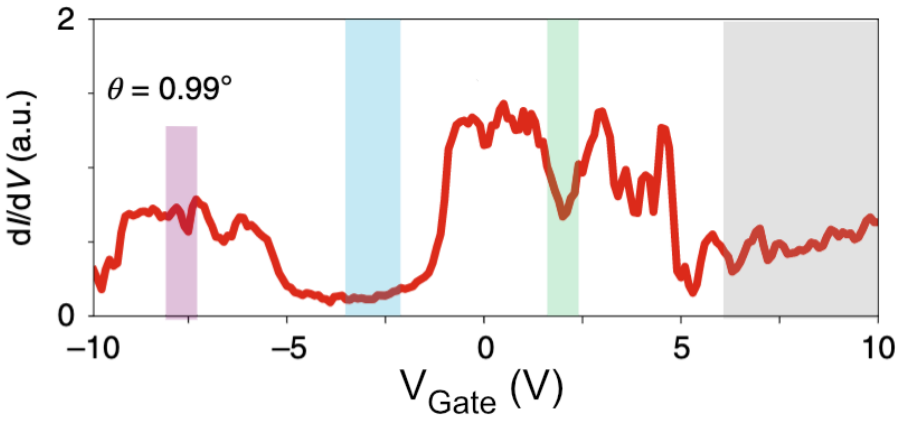

Figure 2.16: Gapped states as a function of doping. dI/dV is measured at fixed $V_{Bias} = 0mV$ while changing the V_{Gate}. Suppression of LDOS is observed near half fillings.

Chapter 3

CORRELATION-DRIVEN TOPOLOGICAL PHASES

As discussed in Chapter 1.3, among many interesting phases, TBG also hosts non-trivial topology in the system. To identify non-trivial topology, dominant experimental tools have been electrical transport measurements, using Hall bar geometry. In this chapter, I will present our novel method that enables STM to give information on non-trivial topology of a system.

With our new tool, we discover a new kind of topological phases, which develops with perpendicular magnetic field in TBG due to strong correlation. We benefit from the spectroscopic capability of STM, and directly visualize its mechanism: Stoner instability. Spatial ability of STM also helps to navigate different twist angles continuously, and corroborate identified mechanism of the new phases.

3.1 Cascade of phase transitions

Stoner instability in MATBG

Zondiner et al. [48] with local compressibility measurements and Wong et al. [49] with STM measurements reported cascade of phase transitions in MATBG, implying flavor symmetry breaking of four-fold degenerate flat bands. The explanation from Zondiner et al. [48] highlights the role of correlations, in the context of Stoner instability. In the case of Stoner ferromagnetism, initially degenerate two spins energetically favors spin polarization when the Stoner criterion $DOS > 1/U$, where U is the strength of interaction, meets. A notable example is Quantum Hall ferromagnetism. When a Landau level with high density of states approach to the Fermi energy, the degeneracy of the Landau level is broken when the Stoner criterion meets, polarizing the spins (and valleys if any) and creating a correlated gap. Similar physics happens in MATBG since the VHS also have a high density of states. When the four-fold degenerate (spin and valley) VHS approaches to the Fermi energy, the Stoner criterion is satisfied at some point and breaks the flavor symmetry. Since it has four flavors, while completely filling (emptying) the band, the band experiences the symmetry breaking four times, creating cascade of phase transitions.

Cascade of phase transitions in our sample

After getting cleaner samples and more reliable STM tips, we also observe a cascade of phase transtions in our samples, which was not obvious in our first generation experiments in Chapter 2. Figure 3.1 shows the evolution of the two LDOS peaks originating from the VHSs of the flat bands. At $V_{Gate} > +5V$, both peaks are below the Fermi energy (E_F, $V_{Bias} = 0$ mV), indicating completely filled flat bands. As V_{Gate} is reduced, the nearby VHS corresponding to the conduction flat band crosses E_F several times, resetting its position at gate voltages corresponding to $\nu = 3, 2,$ and 1 electrons per moiré unit cell. At $\nu = 0$ charge neutrality point (CNP) is reached, where the splitting between VHS is maximized.

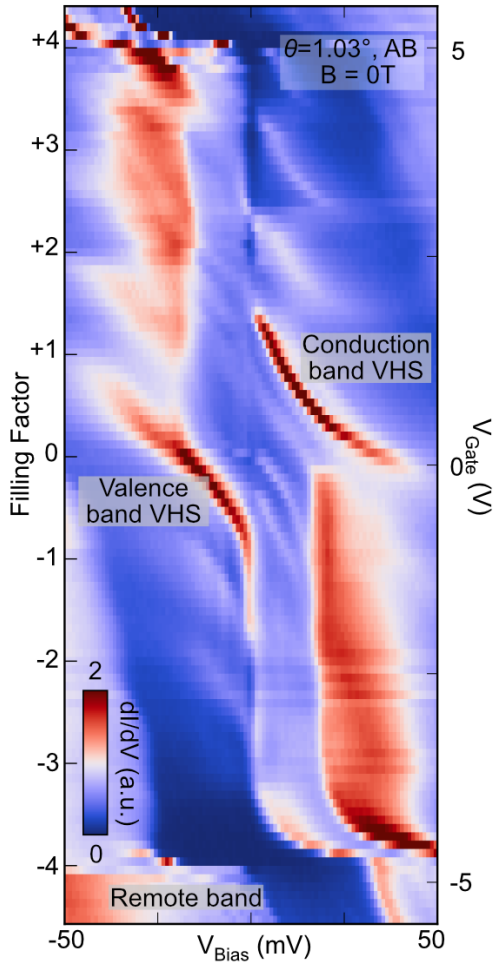

Figure 3.1: Cascade of phase transitions at $\theta = 1.03°$, on an AB site

Role of WSe_2

We use monolayer WSe_2 as a substrate for MATBG in the measurements in Chapters 3 and 4, since our previous work [50] suggests that WSe_2 improves the sample quality and does not change the magic-angle condition. The effects of spin-orbit interaction studied in Ref. [50] showed that the corresponding energy scale is $\sim 1\ meV$, smaller than the spectroscopic features we focus on. Our spectroscopy of MATBG on WSe_2 is qualitatively very similar to the report with MATBG directly on hBN [49]. Our observations thus indicate that the added WSe_2 does not significantly alter the spectrum or the cascade mechanics.

3.2 Landau levels in MATBG and signature of unusual phases

We now apply a perpendicular magnetic field and investigate the Landau levels (LLs) that appear in the flat band (Fig.3.2). In the magnetic field, the biggest change in the overall spectrum is the developed LLs in the flat bands around the CNP (white arrows in Fig.3.2). Multiple LLs gradually appear starting from $B = 0.5T$ from CNP, but at $B = 4T$ only two at the center remain and the others all merge with the VHSs (see Chapter 3.6 for details).

Hofstadter spectrum and merging of Landau levels

To understand the origin of these LLs near the CNP, a linecut at B = 8 T shows four well-resolved peaks (Fig.3.3a). The phenomenological ten-band model [34] with parameters chosen to semi-quantitatively match the data (Fig.3.3b) suggests that the inner two peaks are zeroth LLs (zLLs) originating from MATBG Dirac points. The outer peaks are composed of the LLs from all other parts of the band structure, merged with VHS, and cannot be individually resolved. We call the merged outer peaks simply VHSs.

Importantly, both zLLs and VHSs are expected to carry non-zero Chern number (+1 and −1 respectively per spin and valley flavor) and four-fold spin-valley degenerate. The total Chern number of zLL (VHS) is $C = +4$ ($C = -4$). The importance of non-zero Chern numbers will be clear in the next sections. The four-fold degeneracy of zLLs can be seen by observing the splitting of the levels into four distinct branches by Quantum Hall ferromagnetism, when each of the zLLs crosses the Fermi energy (Fig.3.4). Since there are two zLLs slightly lifted in energy outside of the Fermi energy, we observe in total eight separate branches crossing the Fermi energy (Fig.3.4b).

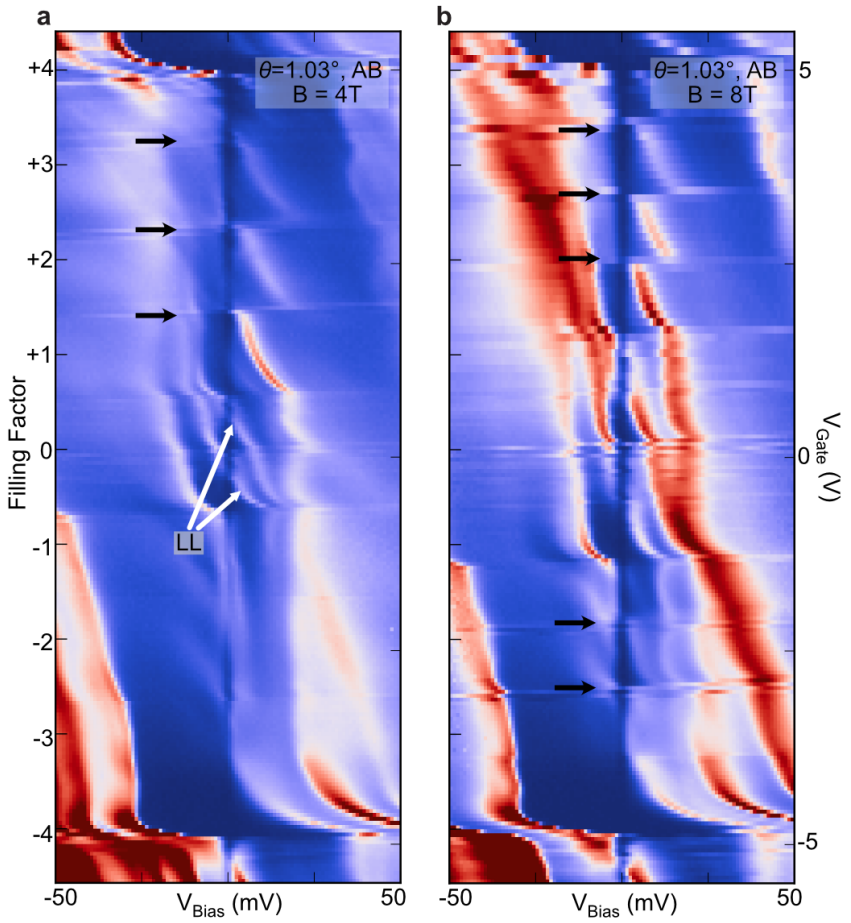

Figure 3.2: Landau levels in MATBG : a) $B = 4T$, b) $B = 8T$. LLs from CNP is the most obvious landau levels (white arrows). Onsets of cascade shift to higher filling factors with higher magnetic field (black arrows).

Signature of unusual phases

The next obvious change is the shifting of the onsets of the cascade transitions with magnetic field (see black arrows in Fig.3.2). These onsets are accompanied by a low LDOS at E_F and nearly horizontal resonance peaks, indicating the presence of gapped states. We attribute the shifting of cascades and the accompanying gaps to the formation of Chern insulating phases enabled by correlations, as we discuss below.

3.3 LDOS Landau fan diagram

Since we see Landau levels from spectroscopy, we want to compare it to the electrical transport measurements reported. MATBG in magnetic fields has so far been studied

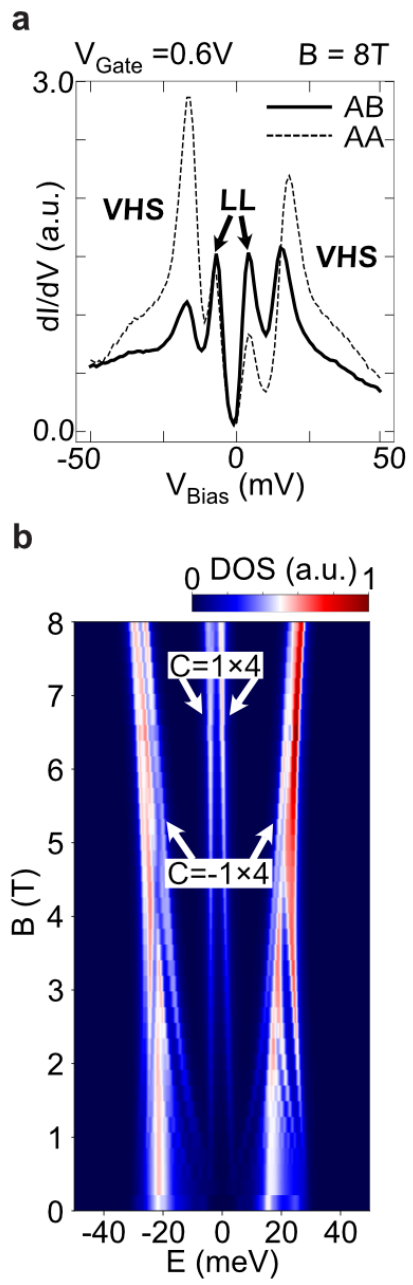

Figure 3.3: Hofstadter spectrum and merging of Landau levels. a) $B = 8T$ linecut around CNP on AA (dashed) and AB (solid) sites. Four peaks are visible. Two inner peaks are from Landau levels, and the two outside peaks are from merging of VHS and multiple LLs, we simply call them VHSs. b) Calculated Hofstadter spectrum, showing four peaks at large ($B > 6T$) B field, reproducing (a).

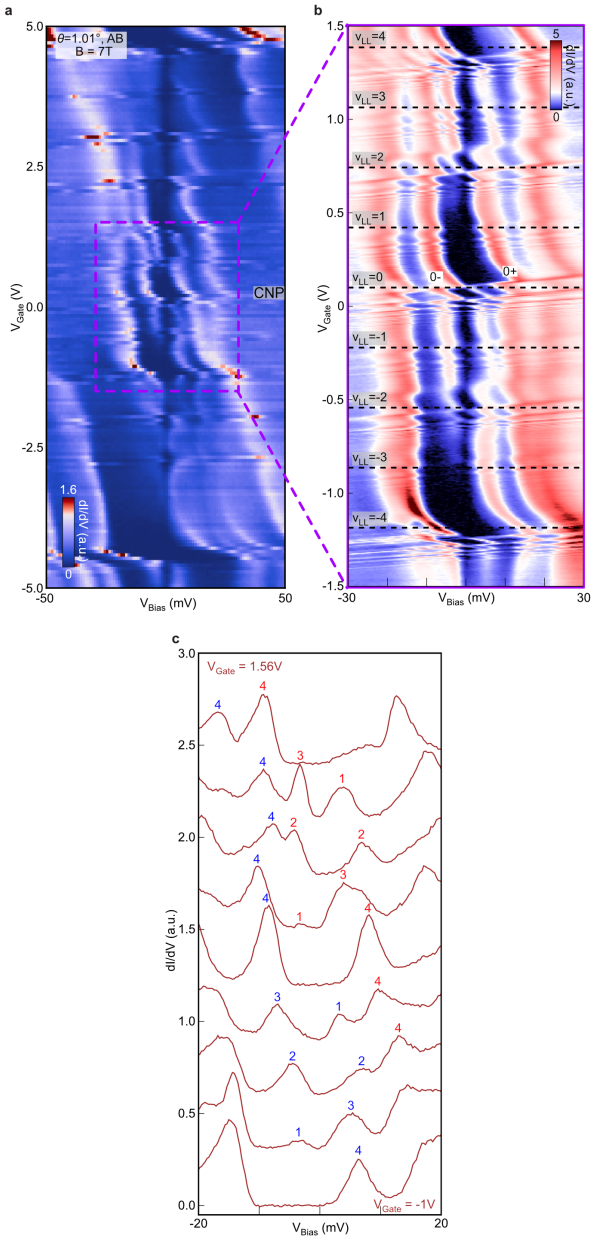

Figure 3.4: Four-fold degeneracy of zeroth Landau level and Quantum Hall ferromagnetism. a) Similar to Fig.3.2, but at $B = 7T$. b) High-resolution blow up of (a) around CNP, showing Quantum Hall ferromagnetic transitions. Each zeroth Landau level experiences four transitions due to four-fold degeneracy. c) Linecuts at each Quantum Hall ferromagnetic transitions, showing degeneracies and corresponding spectral weight shifting.

via Landau fan diagram using transport with Hall bar geometry, and it only provides information close to E_F [10, 12, 51, 52]. We relate these experiments to our STM

measurements by a novel method that enables measuring a full Landau fan diagram via LDOS. Since the transport Fan diagram has information at E_F, we measure LDOS at the Fermi energy to capture the same physics (Fig.3.5). LDOS at E_F is suppressed at gapped regions such as spaces between LLs, and pronounced when there is high density of states, such as LL or VHS. This LDOS Landau fan is acquired by taking the tunneling conductance when the tip height is fixed without feedback and measure LDOS at $V_{Bias} = 0$ mV while sweeping V_{Gate}. After each measurement at a fixed magnetic field, we go to feedback mode again and change the field, and track to the same point relative to the moiré pattern to compensate for any spatial shifting due to magnetic field.

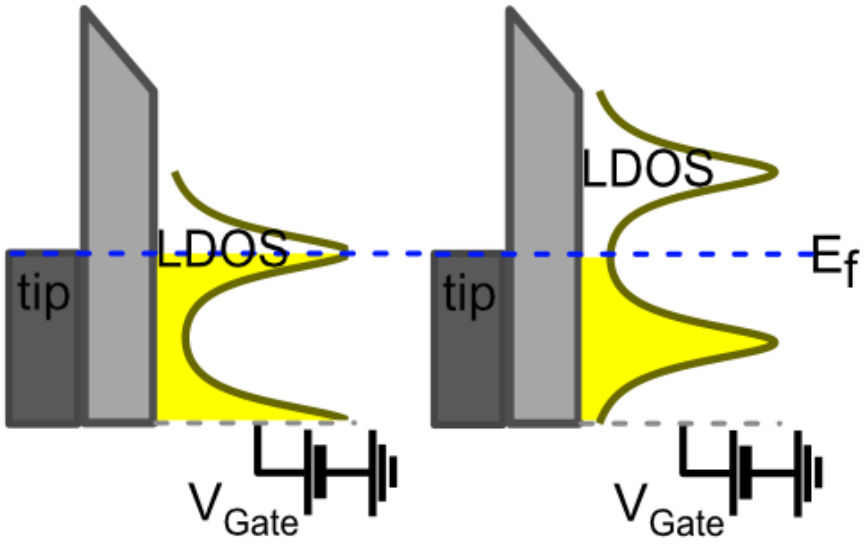

Figure 3.5: Principle of LDOS Landau fan diagram

LDOS Landau fan diagram

Our LDOS Landau fan (Fig.3.6), taken at an AB point, reproduces many of the features established in previous MATBG magneto-transport measurements although it records a fundamentally different quantity—LDOS— instead of transport resistance R_{xx}. A sequence of $0, \pm4, \pm8, \ldots$ from $\nu = 0$, and a sequence of $+4, +8, \ldots$ from $\nu = +4$, a sequence of $-4, -8, \ldots$ from $\nu = -4$ are reproduced. Fermi surface reconstructions at $\nu = \pm2$, which single particle band structure doesn't capture, are also visible in fans emanating from $\nu = \pm2$, with two-fold degeneracy.

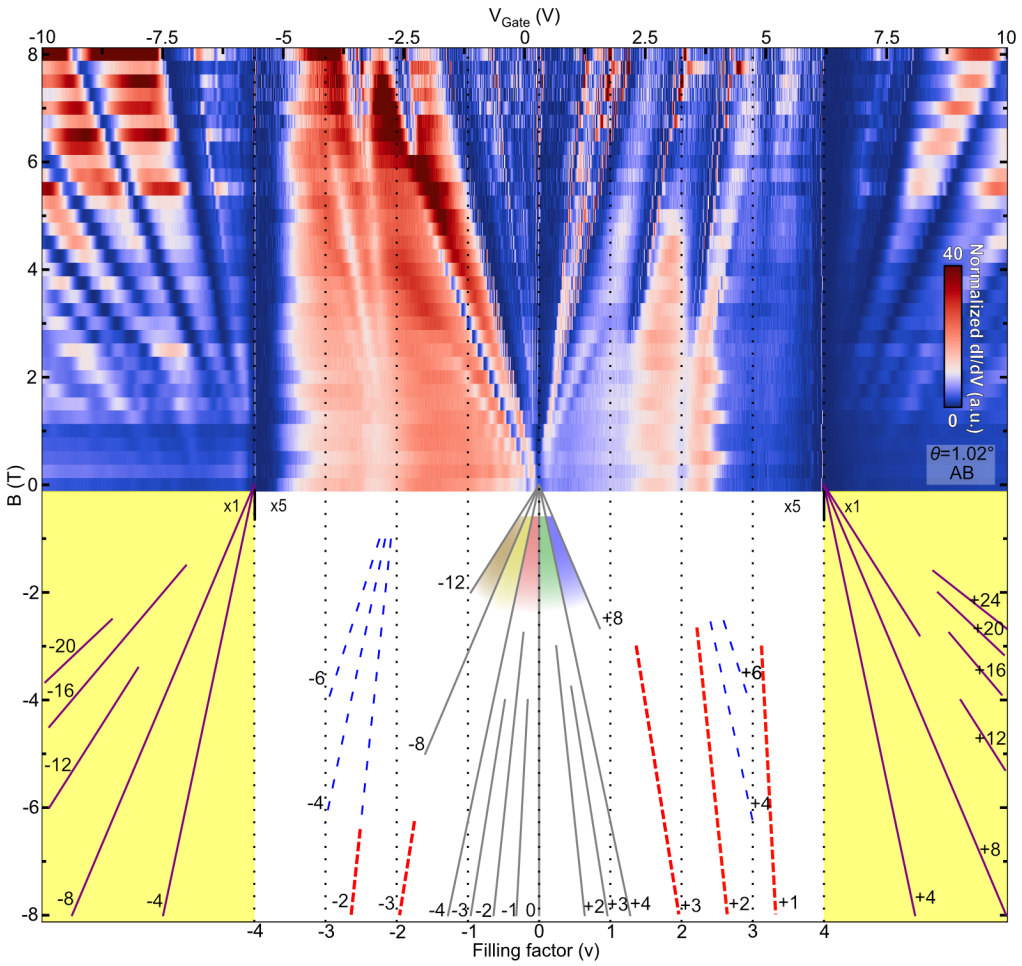

Figure 3.6: LDOS Landau fan diagram taken at an AB site, $\theta = 1.02°$. Gate ranges of filling factors inside $\nu = \pm 4$ are magnified by 5 to clarify the signals. Lower side shows eye-guides with corresponding Chern numbers.

LDOS Landau fan from STM also verifies the conventional method for angle determination in transport measurements. In transport, pinpointing $\nu = \pm 4$ from the fan emanating from it allows to convert carrier densities of $\nu = \pm 4$ (n_s) to a twist angle by $n_s \approx 8\theta^2/(\sqrt{3}a^2)$, where a is the graphene lattice constant. In our LDOS fan diagram, we can practice the same method to get the twist angle. Moreover, we can just directly scan the topography of the area and measure the moiré wavelengths and obtain the twist angle. The twist angle value extracted from the LDOS Landau fan matches with the one seen in topography within 0.01°, which justifies the usage of fan diagram as an angle deducing method.

Trivial advantages of LDOS Landau fan

One obvious advantage of our LDOS fan diagram is that it does not suffer from angle inhomogeneity in a sample. Uri et al. [52] showed that a TBG sample with typical dimensions of $\sim 1\ \mu m$ has significant amount of angle inhomogeneity, and the transport measurement averages them all and shows the data of the most dominant angle. Immediate consequence is that when the inhomogeneity is large, the fans from $\nu = \pm 4$ are faint. However, LDOS fan diagram does not suffer from inhomogeneity since the STM tip is atomically sharp and only picks the information on that particular angle. Therefore, we see very pronounced fans from $\nu = \pm 4$.

The other advantage of LDOS Landau fan diagram is that we can precisely identify gate voltages with the correct filling factors. Once gate voltages corresponding to $\nu = 0$ and $\nu = \pm 4$ are identified, conversion between gate voltage and filling factor is fully defined. This approach, equivalent to the one previously used in transport measurements, is much more precise than the alternative methods used in previous MATBG STM measurements [28, 53–55], where the filling-factor assignments are more ambiguous. By using the LDOS Landau fan, the full filling position can be determined with an error of less than about 0.1 V (Fig. 3.7) or, equivalently, a filling-factor error of 0.07 electrons per moiré unit cell.

3.4 Emergence of correlated Chern insulating phases

Importantly, in addition to Landau levels, we observe strong LDOS suppressions that abruptly appear in finite fields ($B > 3$ T for $\nu > 0$ and $B > 6$ T for $\nu < 0$; red dashed lines in Fig. 3.6), indicating the formation of unusual insulating phases emanating from $\nu = \pm 1, \pm 2$, and $+3$. The corresponding Chern numbers, $C = \pm 3, \pm 2$, and $+1$, respectively, can directly be assigned from the observed slopes of the gap positions as a function of ν and the Diophantine equation [56], $\nu(B) = C \times A_m \times B/\phi_0 + \nu(B = 0)$. Here $A_m = \sqrt{3}{L_m}^2/2$ is the moiré unit cell area, ϕ_0 is the flux quantum, and $\nu(B = 0)$ denotes the filling $(\pm 1, \pm 2, +3)$ from which the phases emanate. Transport studies simultaneously reported similar phases from their Fan diagrams [57–59]. They observe that these phases are insulating, which means that they are Chern insulators that abruptly appear with finite magnetic field.

Connection to spectroscopy

The power of our LDOS Landau fan diagram is that we can perform spectroscopic measurements together. Figure 3.8a shows the spectrum at $B = 7\ T$, focusing on the conduction side. The three white arrows identifies the gaps that appeared in

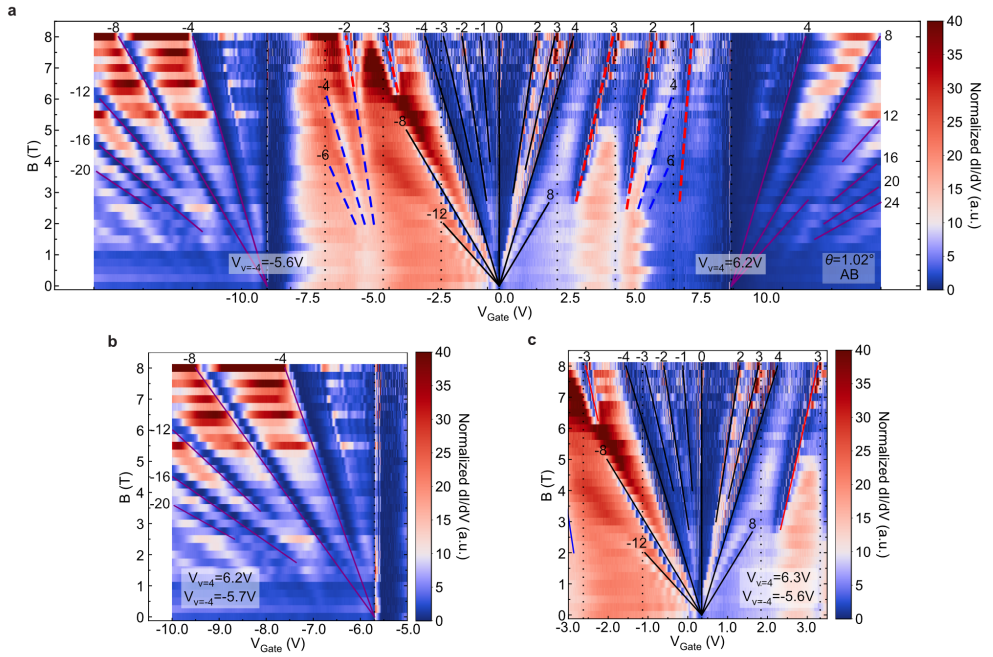

Figure 3.7: Fitting of fans to asign correct filling factors. a) Best matching case. b) Deviation seen around $\nu = -4$ when the used voltage parameter $V_{\nu=-4}$ is shifted by 0.1 V. c) Deviation seen around $\nu = 0$ when the used voltage parameter $V_{\nu=+4}$ is shifted by 0.1 V.

the LDOS Landau fan, which have Chern numbers $C = +3, +2, +1$ emanating from $\nu = +1, +2, +3$, respectively (see Fig. 3.6). As we discussed in Chapter 3 Section 2, at $V_{Gate} = 2$ the left peak is the zeroth LL and the right peak is the VHS. As the gate voltage increases from $V_{Gate} \approx 2$ V, the four-fold degenerate VHS approaches the Fermi level. Just before crossing $V_{Gate} \approx 3$ V, a gap open up at the Fermi energy, accompanied by a set of nearly horizontal resonance peaks.

As a digression, these resonances and accompanied Coulomb diamond features are signatures of the quantum dot formation around the tip due to the emergence of a fully gapped insulating state in its vicinity. For example, bandgaps between the remote bands and the flat band, gaps between LLs and Chern insulating gaps all show

resonances around the gaps. We note that the majority of resonances and Coulomb diamonds are formed below (in V_{Gate}) the gap position expected from the LDOS Landau fan. Because the STM tip and graphene have different work functions, even at zero bias the tip acts as a top gate and slightly dopes the region in the immediate vicinity. The likely presence of Au atoms on the tip and the observed positions of resonance peaks are both consistent with tip-induced hole doping underneath. Consequently, as we increase V_{Gate}, the global sample enters the insulating regime first, and the area underneath the tip can still be conducting—thereby creating a conducting island (that is, quantum dot) and consequent resonances. Further doping will bring the area underneath the tip to the gapped phase, explaining that resonances are below the gap in V_{Gate}. We interpret the resonances and observed Coulomb diamonds as direct evidence of fully developed gaps, given that quantum dots form only when the insulating-phase resistance exceeds the resistance quantum.

Back to the Fig. 3.8a, as V_{Gate} further increases from $V_{Gate} \approx 3$ V, part of the VHS is abruptly pushed up in energy, reducing its spectral weight. Similar transitions are observed also near $V_{Gate} \approx 4$ V and $V_{Gate} \approx 5.1$ V with the spectral weight reducing after each transition. This transition sequence is analogous to the B = 0 T cascade, though with the finite-field. As the Chern gaps follow the position of the corresponding Chern number positions with changing magnetic field, the onsets of the cascade also shift to new V_{Gate} positions to follow the corresponding Chern numbers (Fig. 3.9). We note that for the valence band, the onsets of the cascade do not change until $B = 6\ T$, where the correlated Chern insulating phases start to occur. For $B > 6\ T$, the cascade onsets from the valence band also match with the Chern number lines. To summarize the observation, the gaps open up at the positions of corresponding Chern numbers, and at the same time, cascade of phase transition occurs following the gaps. It suggests that there is an intrinsic connection between the gaps and the cascade of phase transitions at finite magnetic field.

Stoner instability in MATBG at finite magnetic field

These observations can be explained within the physics we discussed from Sections 1 and 2. In Section 1, we explained how high DOS brings instability, breaks flavor symmetry and could open a gap due to correlations. In Section 2, we showed that in magnetic field, MATBG developes two inner LLs ($C = +4$) and two outer VHSs ($C = -4$), and the VHSs have high DOS. Figure 3.8b illustrates what happens at finite magnetic field. When the conduction band's VHS is empty, the Chern number of the occupied bands is $C = -4 + 4 \times 2 = +4$ (here -4 comes from the valence

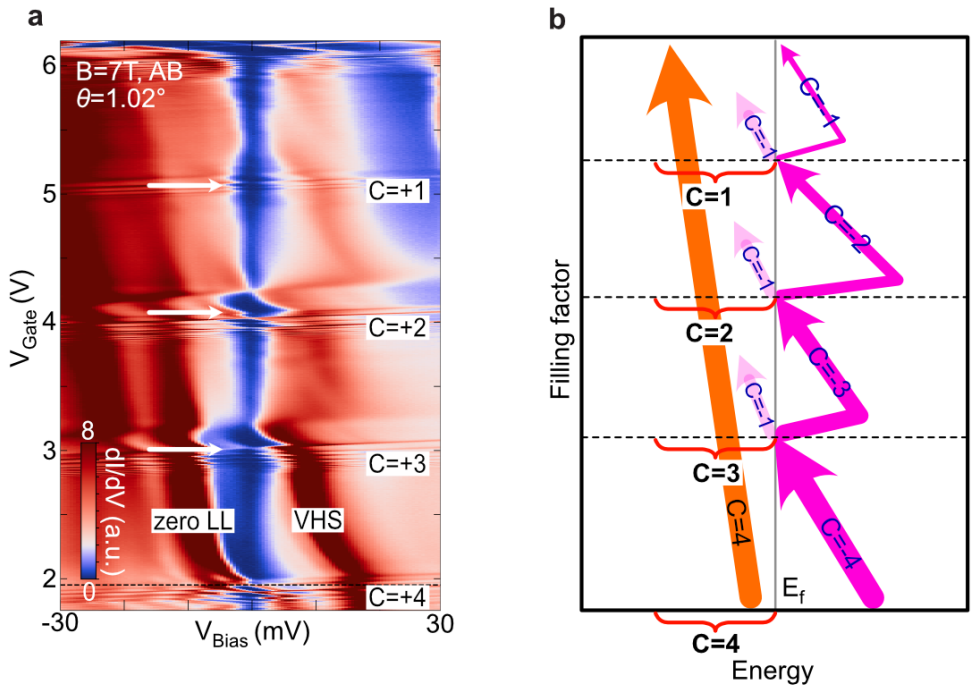

Figure 3.8: Connection to gate spectroscopy at $B = 7\ T$. a) Gate spectroscopy around the conduction side. b) Schematic of the Chern numbers of the system with respect to doping.

band VHS, while $+4 \times 2$ comes from zLLs). Consequently, the gap between the zLL and the bottom of the VHS follows the corresponding $C = +4$ slope in the LDOS Landau fan emanating from CNP. As charge density increases, all four spin-valley flavors in the conduction band are populated equally, until the VHS reaches E_F and

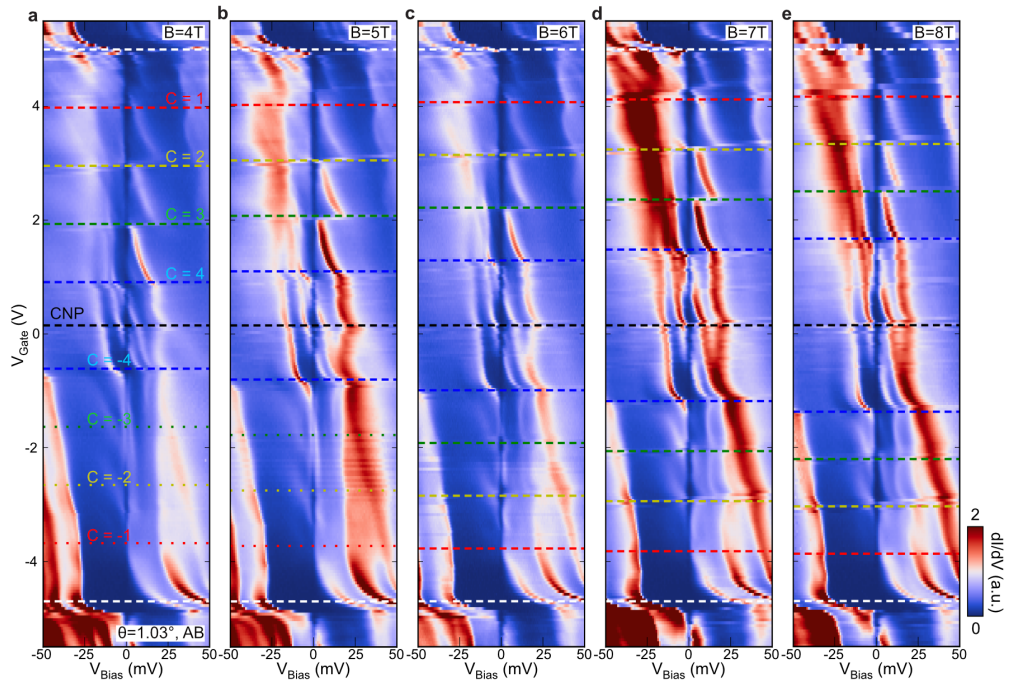

Figure 3.9: Shifting of cascade with magnetic field. a) 4T, b) 5T, c) 6T, d) 7T, e) 8T. The onsets of cascade nicely follow the positions of corresponding Chern numbers.

the instability shifts all carriers to one flavor VHS while the other three are pushed to higher energies, creating a gap. Since the added single-flavor VHS carries $C = -1$, the total Chern number is now $C = +3$, and the next corresponding gap in the LDOS Landau fan follows an accordingly reduced slope. This sequence repeats, creating a cascade. Hence, these unusual Chern insulating phases are the results of correlations at finite magnetic field.

3.5 Phase diagram of the correlated Chern phases

According to the explained mechanism of the correlated Chern insulating phases, there are two independent ways to make the phases easier to happen. One is to have

higher magnetic field; the higher magnetic field would bring more LLs closer in the band structure and make VHS tighter (DOS higher). The other is to change twist angle closer to the magic value; the band structure would be flatter and DOS would be higher.

Angle and magnetic field dependence

We extend the principle of LDOS Landau fan technique to visualize the evolution of these phases with twist angle. For this purpose, we focus on an area where the angle slowly changes over hundreds of nanometers (many moiré periods), so that twist angle is locally well-defined and the strain is low (<0.3%) (Fig. 3.10a). By measuring the LDOS at E_F vs. V_{Gate} and spatial position, we image the development of the Chern phases and the zLLs (Fig. 3.10b). While LL gaps around the CNP form at filling factor $\nu_{LL} = \pm 4, \pm 2, 0$ at fixed V_{Gate} independent of the twist angle, the Chern insulating phases move away from the CNP for larger angles as expected from the change of the moiré unit cell size. The Chern insulating phases are also only observed in a certain narrow range around the magic angle, highlighting the importance of correlations for their formation. For example, the $C = -3$ state emanating from $\nu = -1$ appears only for $1.02° < \theta < 1.14°$ at B = 7 T while the $C = -2$ state is stable for a slightly larger range. Further, we note a general electron-hole asymmetry of the angle range where Chern phases are observed: the $C = -2$ phase emanating from $\nu = -2$ on the hole side is seen for $1.19° > \theta > 1.01°$, while the $C = 2$ state on the electron side is observed for $1.15° > \theta$ down to 0.99°. This observation indicates that the 'magic angle' condition where correlations are strongest differs between the conduction and valence flat bands and highlights the sensitivity of MATBG physics to tiny twist-angle changes. Moreover, at lower fields, the angle range where the Chern phases are visible also diminishes (Fig. 3.10c-e).

Phase diagram

We now draw the phase diagram (Fig. 3.11a) that the correlated Chern phases occur inside the region, which depends sensitively on both magnetic field and twist angle. The observed evolution of the Chern phases with twist angle reflects a competition between Coulomb interactions and kinetic energy. Here the electron-electron interaction scale is approximately set by $U \approx e^2/4\pi\epsilon L_m$ (e and ϵ respectively denote the electron charge and dielectric constant) and increases for larger twist angle. The typical kinetic energy scale, taken to be the bandwidth W of the $C = -1$ single flavor VHS, instead exhibits non-monotonic twist-angle dependence, and is minimal at the

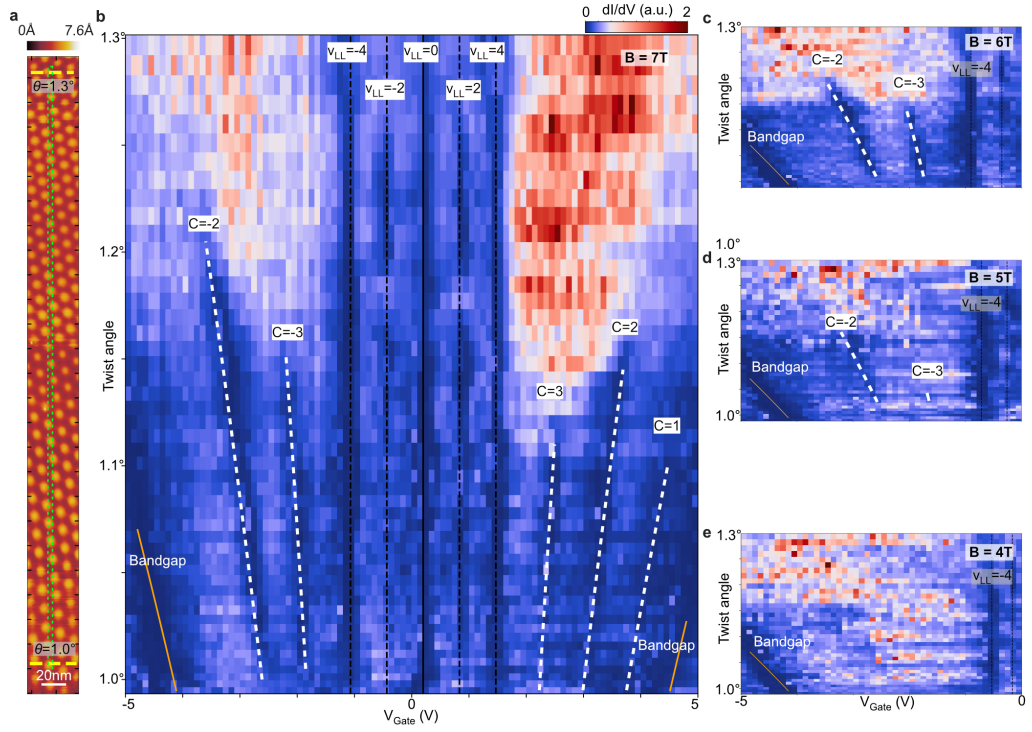

Figure 3.10: Mapping correlated Chern insulating phases. a) an area where the angle continuously changes from $\theta = 1.0°$ to $\theta = 1.3°$. b) LDOS map at $V_{Bias} \approx 0$ showing gaps as dark regions, $B = 7T$. c) 6T. d) 5T. e) 4T. As magnetic field decreases, the Chern phases also diminish to smaller angle range.

magic angle and further narrows with increasing magnetic field (Fig. 3.11b). We thus expect Chern insulating phases to occur close to the magic angle, with larger fields required for their onset away from the magic angle since. Estimates of U/W as a function of B based on a continuum model support this reasoning (Fig. 3.11c) and nicely reproduces the shape of the experimental phase diagram.

3.6 Spectroscopy of Landau levels near CNP

Since we observe Landau levels, we can utilize them to discern some of the mysteries on the band structure of MATBG. Many MATBG properties around the CNP remain poorly understood—e.g., the appearance of four-fold degenerate LLs around charge neutrality [10] instead of eight-fold as expected from the eight degenerate Dirac cones of the two stacked monolayers. These discrepancies are largely due to difficulties in performing band-structure calculations at CNP that incorporate electronic correlations [38, 60, 61], strain [30] and atomic reconstruction [29]. Several

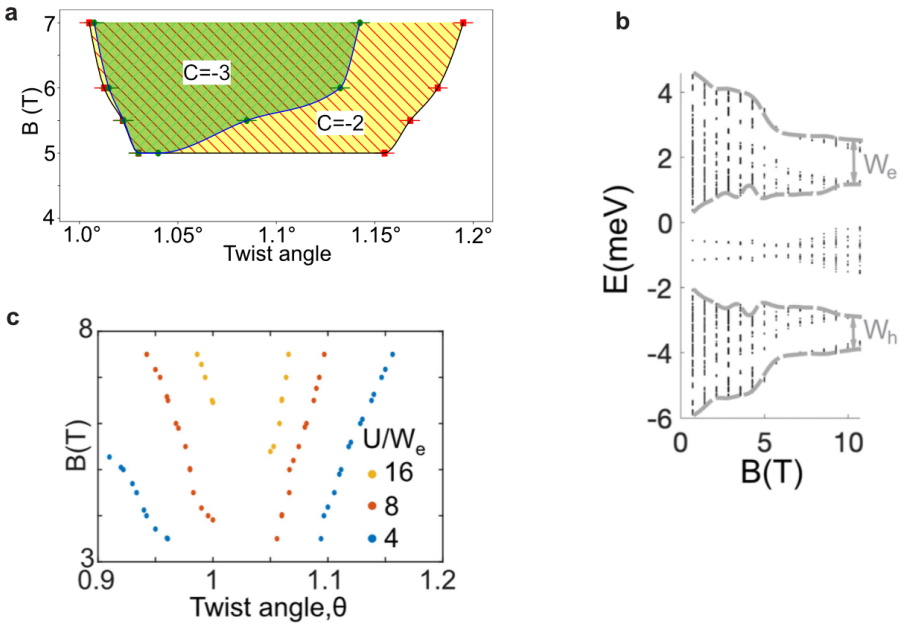

Figure 3.11: Phase diagram and theoretical understanding. a) Experimental phase diagram of $C = -2$ and $C = -3$ phases. b) VHS bandwidth W with changing B calculated from continuum model. c) Measure of correlation strength U/W as a function of B and θ.

mechanisms were proposed to explain the four-fold degenerate LLs formed at CNP [30, 62, 63], although no general consensus has emerged.

Figure 3.12 shows the evolution of CNP LLs for 0.5 T< B < 4 T, as the separations between LLs increase with magnetic field. The four-fold LL degeneracy is seen here through the equal separation between LLs in V_{Gate} as they cross E_F (compare color codings from the diagram in Fig. 3.6). Equal separation in V_{Gate} also means that there are no hidden LLs that are invisible to the spectroscopy. We focus on the relative energy separation between LLs taken at fixed V_{Gate} while varying B (Fig. 3.13). Since the energy separation between LLs can be affected by exchange interactions when LLs cross the Fermi energy, we choose V_{Gate} values to avoid such interaction-altered regions. We then compile the energy spectrum in Fig. 3.13d. We note that, although fine features of the LL spectrum may vary with spatial location, the amount of energy separations remains similar.

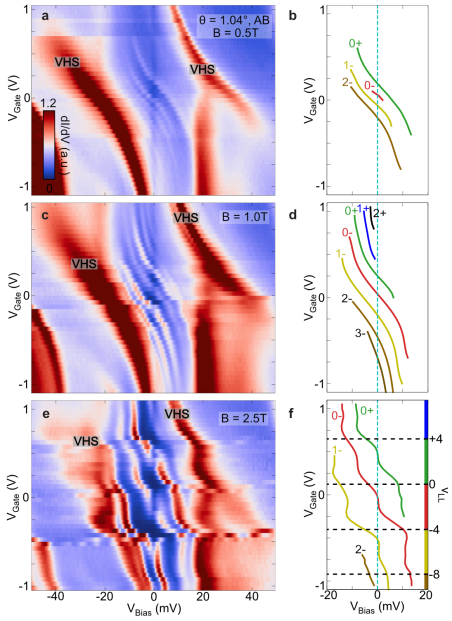

Figure 3.12: Landau levels around charge neutrality. a,c,e) Evolution of LLs from CNP at $B = 0.5T$, $B = 1T$, and $B = 2.5T$, respectively. b,d,f) Tracing the LLs from (a,c,e)

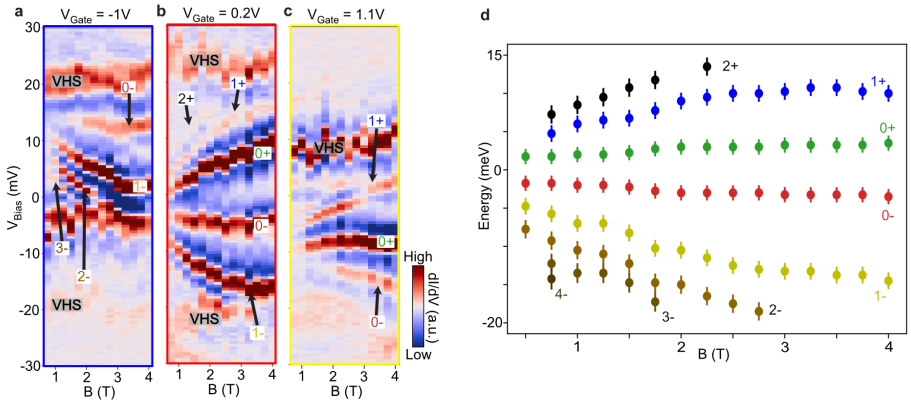

Figure 3.13: Energy spectrum of Landau levels at charge neutrality. a,b,c) Energy spectrum at $V_{Gate} = -1\ V$, $V_{Gate} = 0.2\ V$,and $V_{Gate} 1.1\ V$, respectively. d) Compiled energy spectrum of the CNP LLs.

The observed LL spectrum can be explained with a scenario wherein the two moiré Brillouin zone Dirac cones are shifted in energy, either by strain (0.3% in this area) [62, 63] or layer polarization due to a displacement field [64]. In this

scenario, 0+ and 0− LLs (Fig. 3.13) originate from the two Dirac points and the spectrum can be compared to the Dirac-like dispersion $E_n = sgn(n)v_D\sqrt{2e\hbar|n|\mathrm{B}}$ with $sgn(n) = n/|n|$. The observed LL separations (e.g., 8 meV for 0− to 1− and 5 meV for 1− to 2− at B = 2 T) yield a Dirac velocity $v_D \approx 2 \times 10^5$ m/s. The extracted value exceeds continuum-model predictions by an order of magnitude, highlighting interaction-induced modification of MATBG bands near the CNP.

Although this scenario (details in Fig. 3.14c,d) matches well with most of the Landau levels, as shown in Fig. 3.14i, experimental data seem to miss the LLs from the lower blue dashed lines. Here the two Dirac cones create separate sets of Landau levels, colored in blue and red. Other scenarios such as Fig. 3.14e,f,g,h all induce very complicated mixtures of LLs which we don't see in the experiment. One possible scenario remaining is that the observed LLs are actually from γ pockets (Fig. 3.14a,b). But the origin of this giant inversion of γ pockets is not understood yet. We believe that some kind of partial mixtures of γ and the Dirac cone could reproduce the experimental spectrum.

Moreover, electron-hole asymmetry is also present, as the energy differences between the first few LLs on the hole side are larger than their electron-side counterparts. Moreover, upon doping, LLs move together toward the VHS while the separation between them is hardly affected (Fig. 3.12a,c,e). This finding signals that dispersive pockets within the flat bands do not change significantly as flatter parts of the bands deform [38, 60]. These observations place strict restrictions on the MATBG electronic bands and provide guidance for further theoretical modeling.

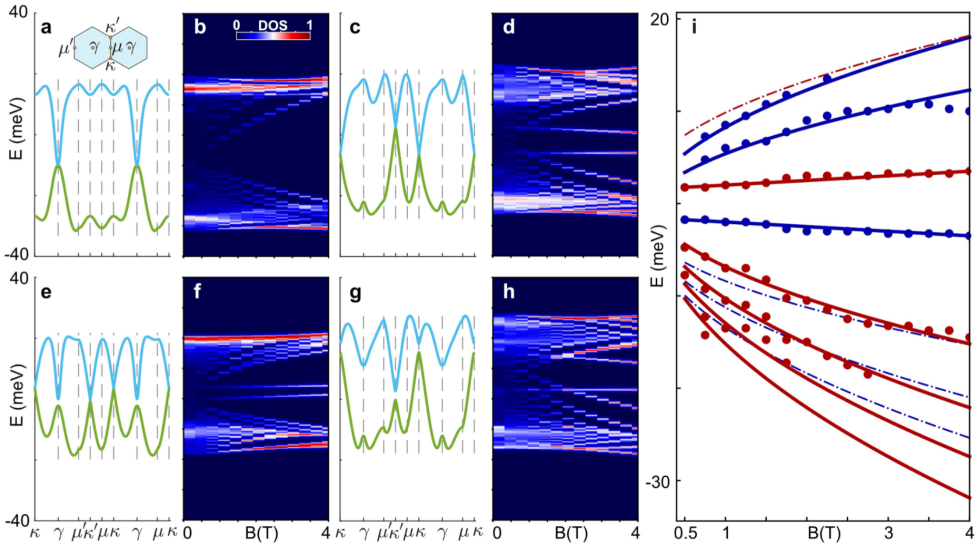

Figure 3.14: Possible scenarios for the band structure around charge neutrality. a,c,e,g) Model band structures. b,d,f,h) Landau level spectrum from the model band structures. i) Experimental data laid on calculation from (c). Overall the spectrum is matching well, although the blue dashed lines are missing in the experiment.

Chapter 4

INTERACTION-DRIVEN BAND FLATTENING

Flat band dispersion is a necessary ingredient for having strong electronic correlations in TBG. Seminal theoretical considerations [5–7] suggested that, when two graphene sheets are twisted at a particular magic angle of 1.1°, the Dirac velocity of the resulting TBG electronic bands vanishes and the band becomes entirely flat with the bandwidth less than 5 meV. However, experimental bandwidths from STM [28, 53–55] as well as compressibility measurements [48, 65] are all much larger, of the scale of 50 meV. Since the rough estimate of electronic interaction is given by $U \sim \frac{e^2}{4\pi\epsilon L_M} \sim 30\ meV$, U/W, which tells strength of correlation, becomes less than unity and might not be enough to bring strong correlations.

To resolve this discrepancy, we utilize STM to look into the detailed TBG band structure. By following Landau levels that form with perpendicular magnetic field, we find that electronic interaction significantly deforms the band and creates locally flatter portions within the band structure. We show that the correlated phenomena begin not because the entire band is flat, but because the relevant portion of the band is flat.

4.1 Band structure at slightly larger twist angle

As shown in Chapter 2 and 3, the measured LDOS contains large contributions from correlations around the magic angle. To minimize the effect of correlations and reveal the bare band structure, we measure a TBG region with local twist angle larger than the magic angle ($\sim 1.1°$).

Gate dependent spectra at larger angle

Figure 4.1 shows the gate dependent spectroscopy at 1.26°. Two VHSs are separated by $\sim 30\ meV$, and cross the Fermi energy as the system is doped, as we discussed in to Chapter 2 and 3. However, all the important signatures of correlations such as enhancement of VHS separation at the CNP or the cascade of phase transitions are missing, providing an ideal playground for investigating the bare band structure of TBG.

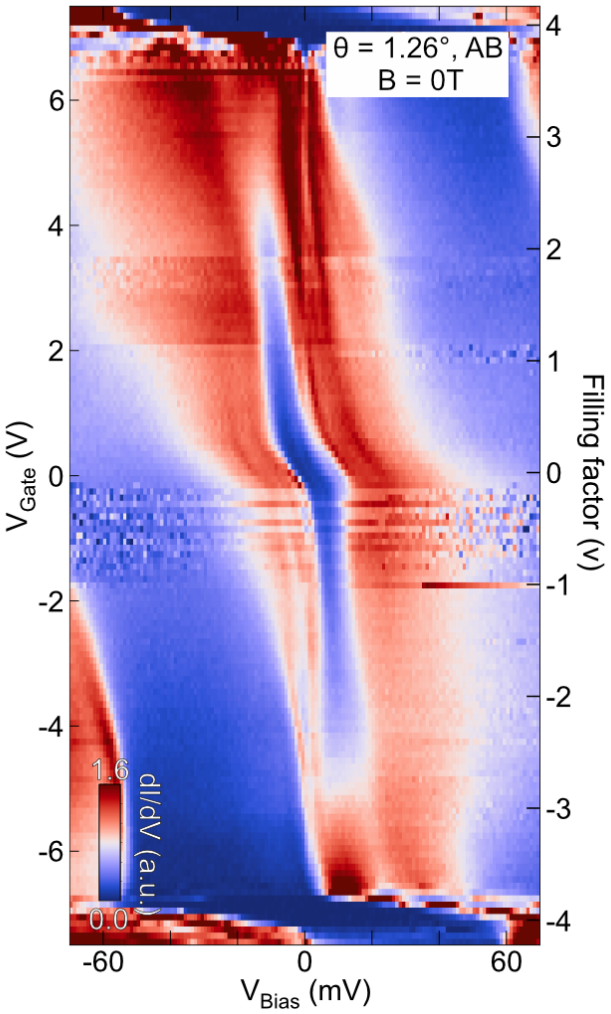

Figure 4.1: Gate dependent spectra at $\theta = 1.26°$.

Two sets of Landau levels in TBG band structure

To examine the band structure in more detail, we probe Landau levels (LLs) that develop when an out-of-plane magnetic field is applied. The tunneling conductance spectrum taken on an AB site shows LLs at $\theta = 1.32°$ (Fig. 4.2), similar to Chapter 3.2. However, at this larger angle, two different sets of LLs are observed as LDOS peaks separated by the VHSs. The LLs from the inner set, with energies bounded within the two VHSs [66] (Chapter 3), originate from band pockets around the κ and κ' high symmetry points of the moiré Brillouin zone; we therefore denote them as κLLs (Fig. 4.2). Similarly we define the LLs outside the VHSs as γLLs since they originate from portions of the bands around the γ point (see Chapter 1.1 for the

discussions on high symmetry points).

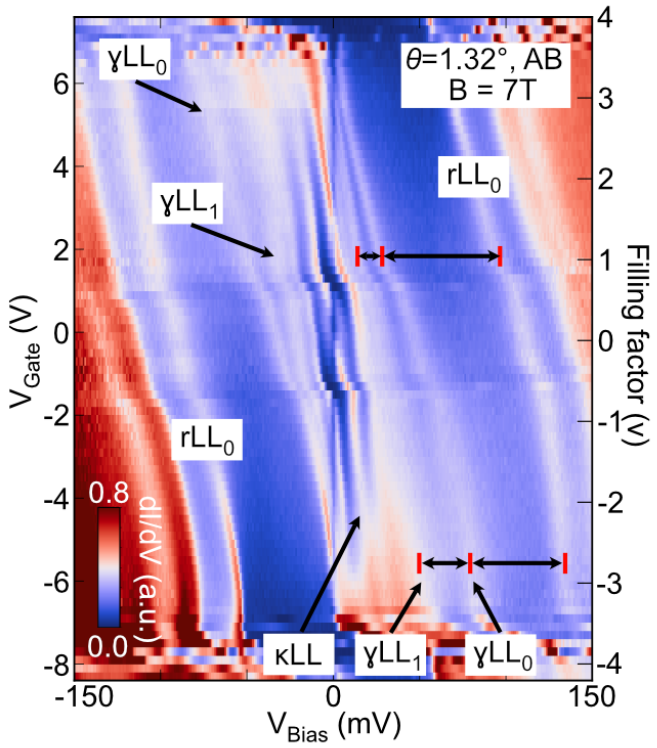

Figure 4.2: Landau levels at $\theta = 1.32°$, $B = 7\ T$ on an AB site.

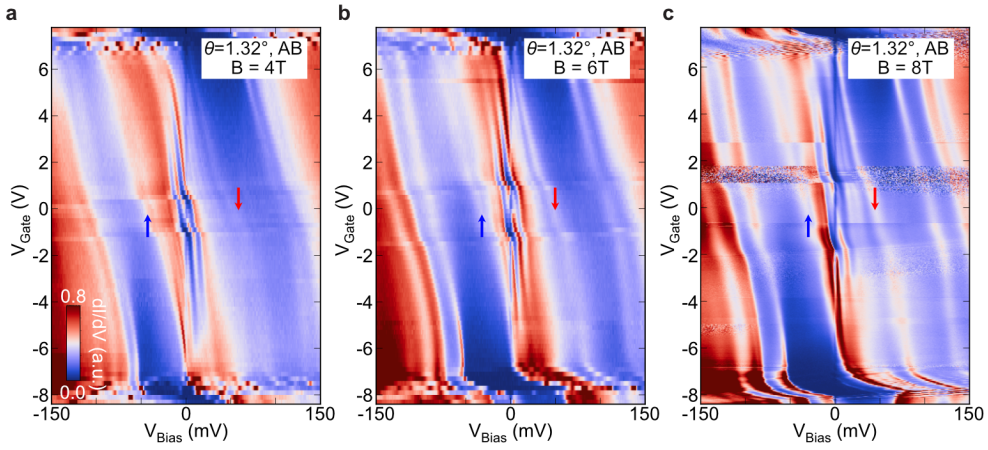

Figure 4.3: Field dependence of the Landau levels at $\theta = 1.32°$. a,b,c) 4T, 6T, 8T, respectively. The positions of the red and blue arrows are used in the next figure.

This assignment is justified by the magnetic-field dependence of the observed LL spectrum (Fig. 4.3). In particular, upon increasing the magnetic field, the zeroth γLLs (γLL_0 in the valence and conduction bands, marked in blue and red arrows in Fig. 4.3) approach the VHSs, as expected from the conduction- and valence-band dispersion at the γ point (Fig. 4.4a); the κLL energies, in contrast, do not change—consistent with the zeroth LLs expected from the Dirac-like dispersion at the κ, κ' points. Continuum model calculations of Landau level spectrum confirms that the LLs from γ point move in energy with magnetic field, but the LLs from κ, κ' points do not move in energy with magnetic fields (Fig. 4.4b).

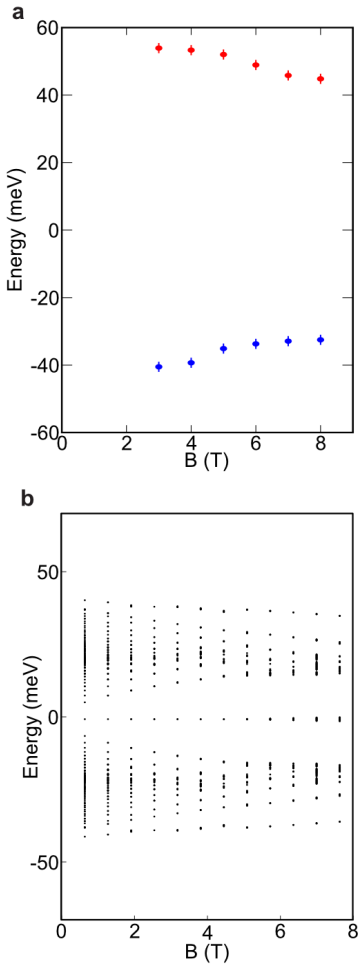

Figure 4.4: Evolution of γ LLs and κ LLs with magnetic field. a) Experimentally extracted energy spectrum of γ LLs from Fig. 4.3. b) Theoretical Landau level spectrum.

Moreover, even though both κLLs and γLLs are visible on the AB sites, only the κLLs are resolved on AA sites (Fig 4.5). This observation suggests that the spectral weight of the κ, κ' pockets is spatially located predominantly on AA sites while the weight of the γ pocket is distributed instead over AB sites and intermediate domain walls, in line with previous theoretical calculations [38, 64, 67].

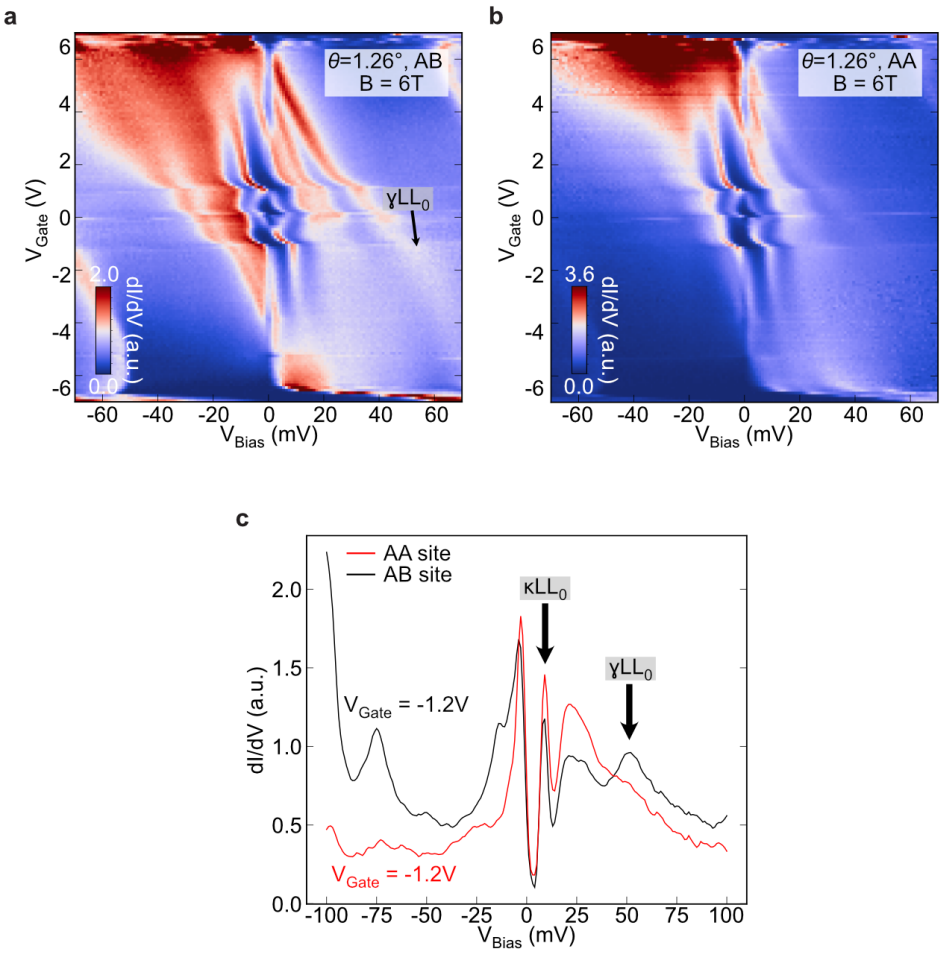

Figure 4.5: Spatial variations in LLs. a) Both κLLs and γLLs are visible on an AB site. b) Only κLLs is clearly visible and γLLs is faint. c) Linecuts showing the relative spectral weight.

Setting continuum model parameters with Landau level separations

As a side note, the non-interacting continuum model has a range of different parameters, notably the moiré interlayer couplings u, u', bare graphene velocity v, and

twist angle θ. Their ratio $\eta = u/u'$ is denoted as a relaxation parameter. To fix these two parameters u and u' we focus on the largest experimentally measured angle of $\theta = 1.32°$ where the role of interactions is least important. We fix $u' = 90$ meV and $u = 0.4u'$ to correctly reproduce the LL spectrum spacing between the γLL and the first LLs from the remote bands ($\sim 60\ meV$), as seen in Fig. 4.6. Conventionally used value of $\eta = 0.8$ cannot reproduce our experimental data. We assume these deduced values to hold to lower angles in the calculations in the later sections. This approximation misses the subtle role that relaxation plays on increasing the ratio η as the twist angle is brought closer to the magic angle [68].

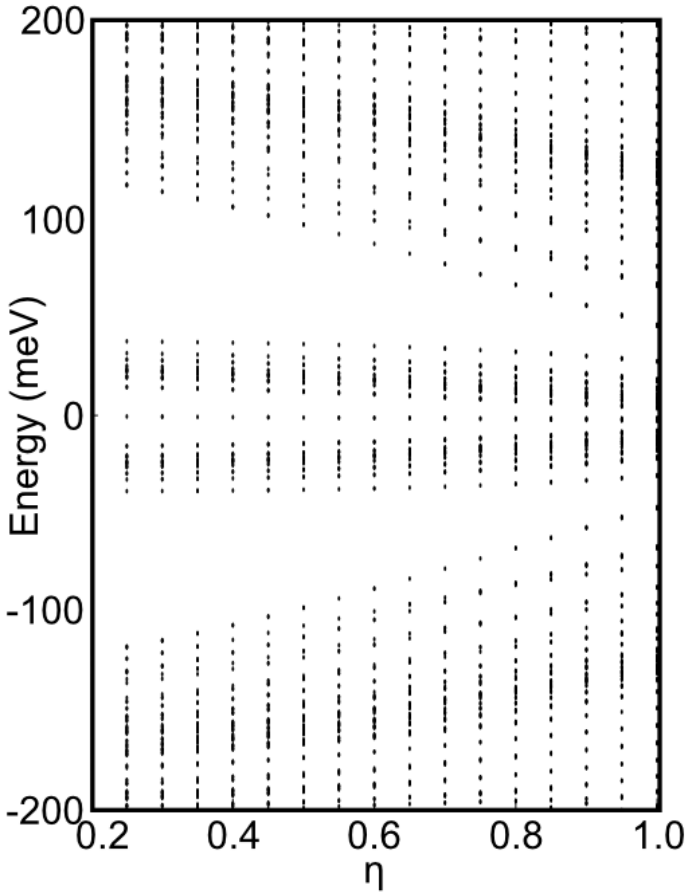

Figure 4.6: Theoretical LL spectrum as a function of the parameter η at $\theta = 1.32°$. Note that the spacing between the first LL from the remote band and the γLL from the flat band is mainly determined by η.

Band deformation revealed by LL separations

Importantly, the energy separation between γLL_0 and γLL_1 changes with carrier density (Fig. 4.2, highlighted by black arrows), signaling significant deformation of the moiré bands with doping even at the large twist angle 1.32°. Figure 4.7a highlights this effect by fixing the position of κLL to 0 at various gate voltages. Extracted energies are shown in Figure 4.7b as a function of filling factor. For the conduction band, the separation is maximized at $\nu = -4$, where $E(\gamma LL_0) - E(\gamma LL_1) \approx 25$ meV, and monotonically decreases below 5 meV near $\nu = +4$. For the valence band, the trend is reversed: the separation between γLLs increases with filling factor. The inset in Figure 4.7b represents that this effect is a result of the band deformation. The separation between LLs from the flat band and the remote band are also changing, as shown in Figure 4.8a. Figure 4.8b shows the change of effective mass due to this band deformation.

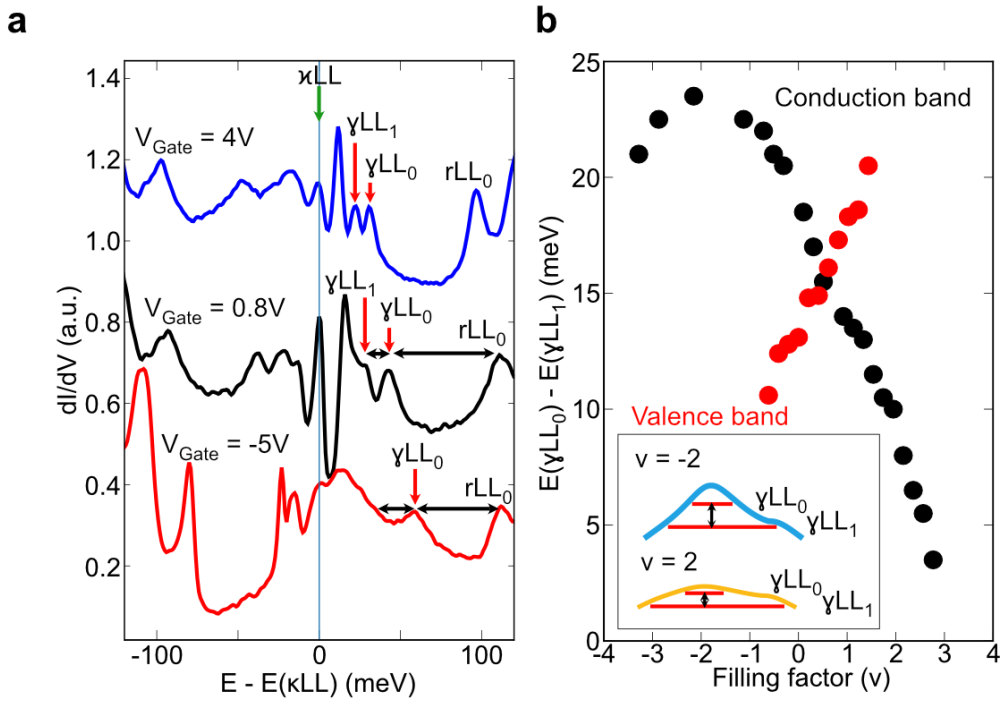

Figure 4.7: Energy separation of LLs as a function of doping. a) Linecuts from Fig. 4.2, setting the position of κLL to zero. b) Extracted energy separations $E(\gamma LL_0) - E(\gamma LL_1)$ as a function of doping, for conduction band (black) and valence band (red). The inset represents that this effect is caused by the band deformation.

Note that a displacement field, likely present due to the single back-gate geometry

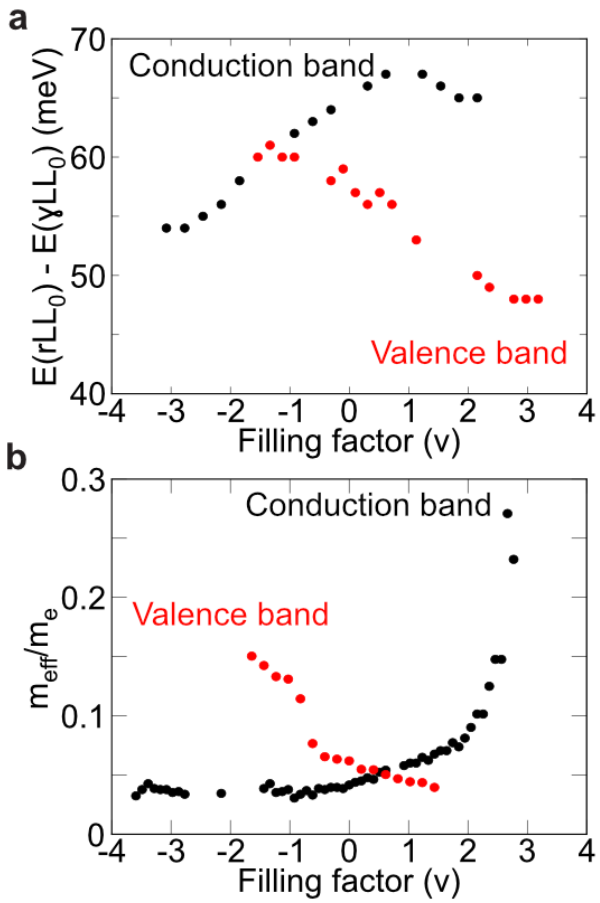

Figure 4.8: Effective mass as a function of doping. a) Extracted energy separations $E(r\mathrm{LL}_0) - E(\gamma\mathrm{LL}_0)$ as a function of doping, for conduction band (black) and valence band (red). b) Effective mass changing with the doping.

of our device, might also slightly modify the band structure with doping. However, the displacement field would change the conduction and the valence bands symmetrically, in contrast to the observed asymmetric evolution of γLLs. As shown in Fig. 4.9, the separations between γLL_0 and γLL_1 are not much changing with displacement field, although κLL starts to split into two which we do not resolve in the experiment, meaning that the simulated displacement field is in the right range.

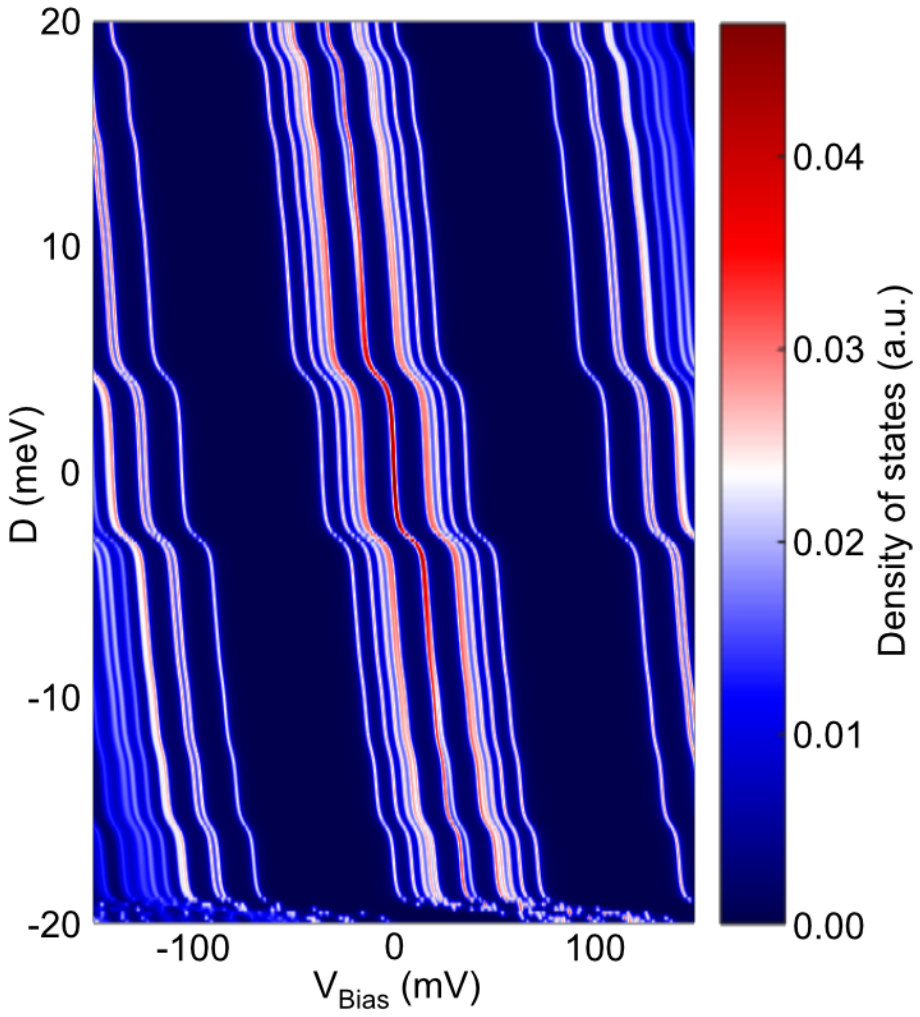

Figure 4.9: Effect of displacement field. The displacement field cannot explain observed asymmetric separation change.

4.2 Interaction-driven band deformation : Hartree effect

The doping-dependent shifts between γLLs are well-captured by a model that includes interaction effects deriving from the inhomogeneous charge distribution in a moiré unit cell [38, 60, 69–71]. Starting from charge neutrality, electrons are first added or removed from states near κ, κ' that localize primarily on AA sites—creating an associated inhomogeneous electrostatic Hartree potential peaked in the AA regions. States near the γ point feel this potential less strongly compared to states near the κ point because they are relatively delocalized within the unit cell. The electrostatic potential experienced differently in each part of the moiré bands

renormalizes the band dispersion. This band deformation changes upon doping because the Hartree potential depends on the filling of the moiré bands. Figure 4.10 presents the calculated band structures for different integer fillings at B = 0 T. The conduction and valence bands deform asymmetrically with doping: the conduction (valence) band becomes flatter and the valence (conduction) band more dispersive as the filling factor increases (decreases).

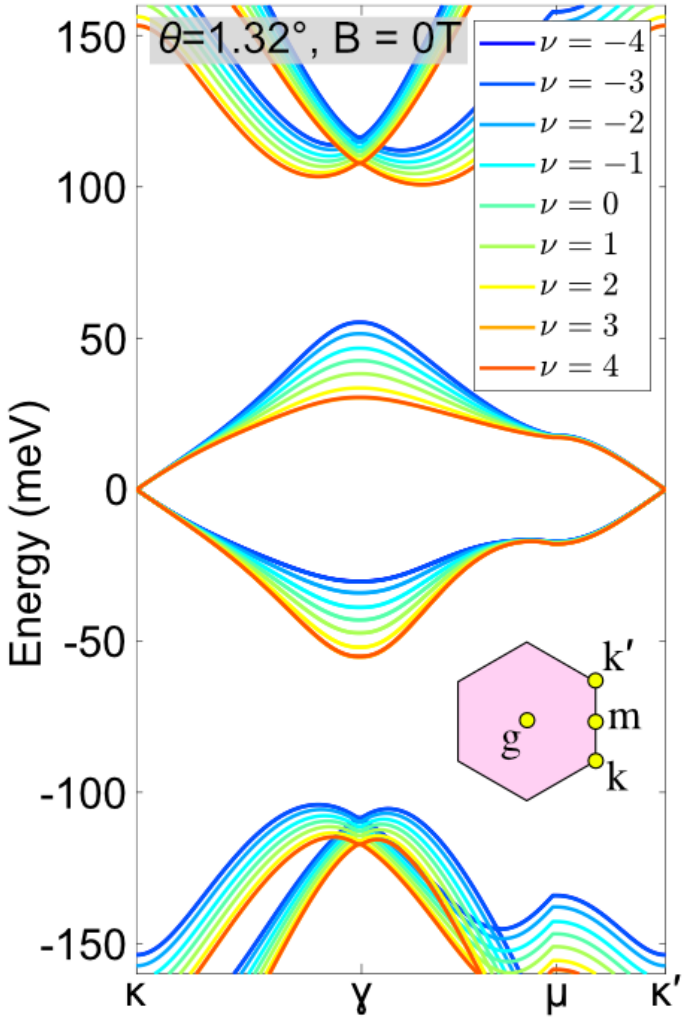

Figure 4.10: Hartree effect on band structure. κ points and γ point shift relatively upon doping.

Consequently, in finite magnetic fields the energy separation between γLLs also changes asymmetrically. The Landau level spectrum evaluated with only the electrostatic Hartree potential (Fig. 4.11) indeed reproduces the main features of the experimental data for this twist angle.

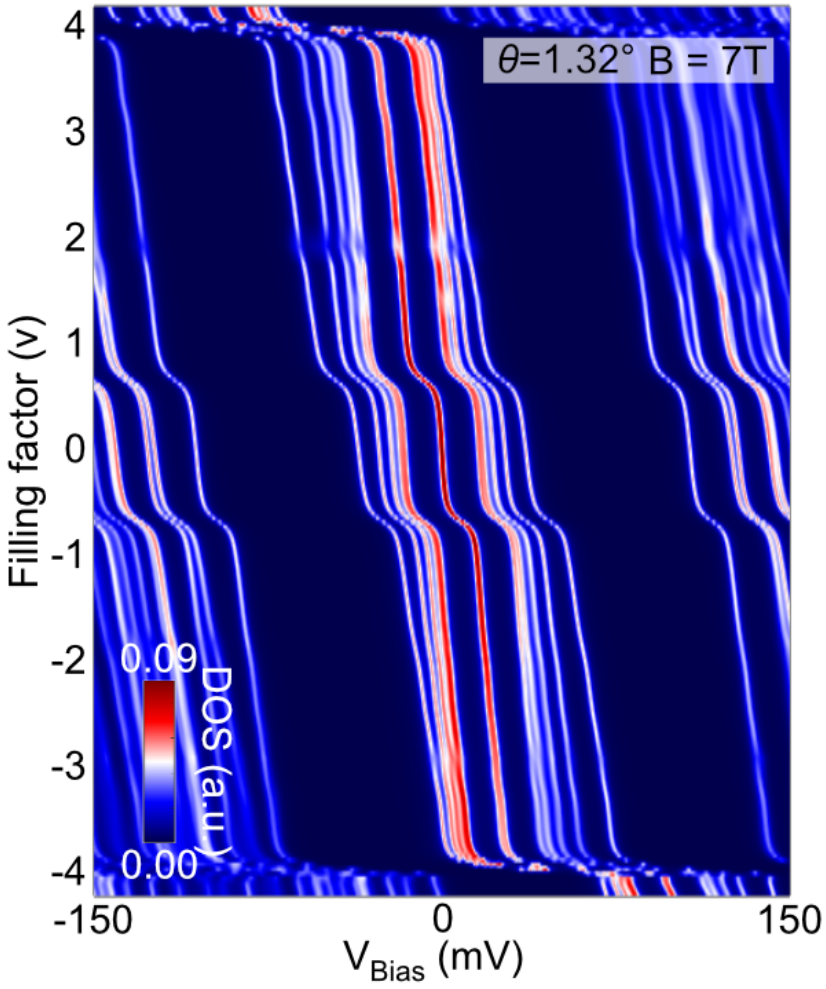

Figure 4.11: Simulated DOS incorporating Hartree effect with magnetic field. The calculation captures the doping dependent energy separation change between γLLs.

4.3 Mapping the band flattening

An interaction-induced deformation of the moiré bands completely flattens the γ pocket when the twist angle approaches the magic-angle value, as can be deduced from the measured evolution of γLLs. By visualizing this interaction-driven band flattening effect from mapping the LL evolution changing the twist angle and doping, we are able to pinpoint where the γ pocket merging happens. As shown in Chaper 3, to change the twist angle continuously, we focus on an area where the angle changes over a $\sim$ 600 nm area and strain is relatively low ($< 0.3\%$), see Fig. 4.12a.

Spatially resolved measurements in this area reveal the twist angle-dependent evolu-

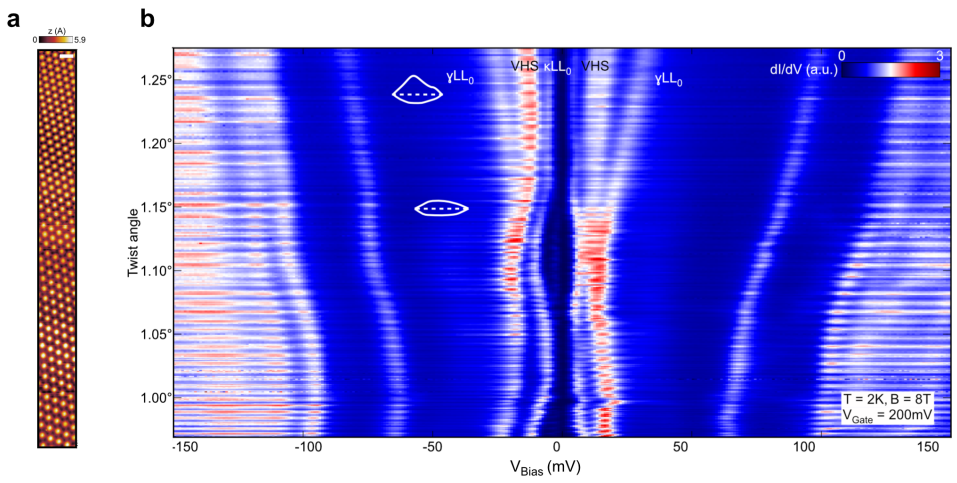

Figure 4.12: Mapping the band flattening. a) An area where the twist angle continuously changes from $\theta = 0.98°$ to $\theta = 1.27°$. b) Spatial evolution of LLs at $V_{Gate} = 200\ mV$. γLL_0 on the conduction and valence band merge with VHS at angles below $\sim 1.15°$.

tion of LLs with electrostatic doping (Fig. 4.12b). At V_{Gate} near the charge neutrality point (CNP, $V_{Gate} = 200mV$), we observe that, for both the valence and conduction moiré bands, the γLL_0 eventually merges with the corresponding VHS—signaling maximal band flattening. The onset of merging occurs at somewhat larger angles for the valence band ($\sim 1.15°$) compared to the conduction band ($\sim 1.1°$).

Moreover, doping strongly shifts this onset. For example, in the valence band (Fig. 4.13a) the γLL merging point, or the maximal band flattening, moves considerably towards larger twist angles for hole doping. At electron doping, the merging happens around 1.10°. At charge neutrality, the merging happens around 1.15°. And at hole doping, the merging is shifted to around 1.25°. This shifting of merging angles upon doping clearly visualizes the effect of the interaction-driven band flattening.

4.4 Band flattening and Correlated Chern Phases in finite magnetic field

As discussed in Chapter 3, in out-of-plane magnetic field, DOS becomes high enough to ignite Stoner's instability and create correlated Chern phases emanating from integer fillings. Here we show that the correlated Chern phases start to occur with the twist angle when γLL_0 merges with a VHS, which enhances DOS significantly.

At 1.23° (Fig. 4.14a), the γLL_0 energies are well-resolved in both the valence and

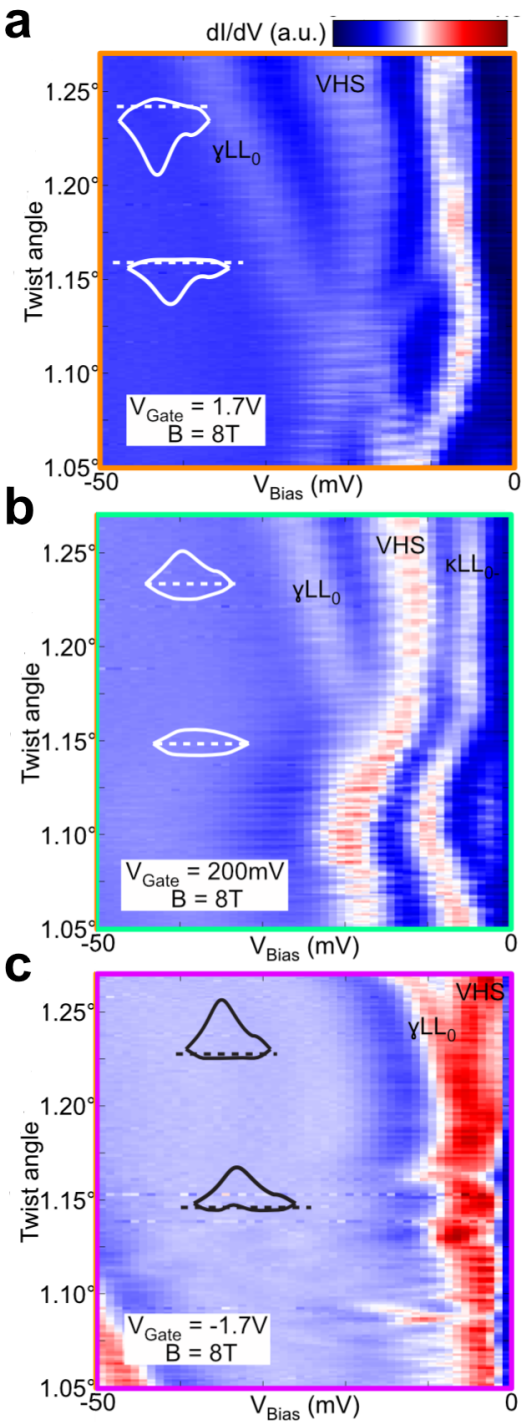

Figure 4.13: Shifting of γLL merging point upon doping. a) $V_{Gate} = 1.7\,V$, electron doped. b) $V_{Gate} = 0.2\,V$, charge neutrality. c) $V_{Gate} = -1.7\,V$, hole doped. The inserted band structures schematically show corresponding band structures.

conduction bands between $\nu \approx -2.2$ and $\nu \approx +3.3$, beyond which one of the two merges with the corresponding VHS; in this case, the joining further occurs at the doping where the VHS lies at the Fermi energy $V_{Bias} = 0$ mV. The difference in the filling factor magnitude where the conduction and valence band γLLs merge reflects an appreciable electron-hole asymmetry. At this large twist angle, aside from quantum Hall ferromagnetism in the zeroth κLL (responsible for the structure between $\nu = -1$ and +1), no pronounced correlated gaps are observed at the Fermi energy.

As the twist angle is decreased to 1.17°, the γLL_0 in the valence band merges with the VHS at a lower $|\nu|$, and an additional correlated gap appears when the merged γLL_0 crosses the Fermi energy (black arrow in Fig. 4.14b). This correlated gap is the same kind of gap due to the correlated Chern phases from Chapter 3. For an even lower angle of 1.15°, correlated gaps also begin to emerge on the electron-doped side after the γLL_0 merges with conductance band VHS (black arrows in Fig. 4.14c). Our observations suggest that such correlated Chern phases emerge only once portions of the bands around γ become maximally flat and join with the VHS.

4.5 Band flattening and Correlated Insulating phases at zero magnetic field

Recent theoretical considerations also suggest that the band flattening is linked to the formation of certain correlated phases [72]. To explore the development of zero-field correlated phases as a function of twist angle, we perform angle-dependent gate spectroscopy to trace out the evolution of the LDOS at the Fermi level ($V_{Bias} \approx 0$) as a function of charge density (V_{Gate}); see Fig. 4.15. Pronounced LDOS suppression near the Fermi energy occurs at certain integer filling factors ν. For all angles, prominent suppression is observed at $\nu = \pm 4, 0$, reflecting the small LDOS around the CNP ($\nu = 0$) and band gaps at full fillings ($\nu = \pm 4$). At $\nu = \pm 2$, +3, +1, we additionally observe sharp LDOS drops that can be attributed to emerging correlated insulating gaps similar to those observed in transport [10, 12, 50, 51].

Importantly, the observed LDOS suppressions at integer fillings begin to emerge within the same range of angles that displays considerable band flattening in finite fields. For example, the angle onset for $\nu = -2$ filling insulating state starts around 1.17°, where the γLL is fully merged with VHS (Fig. 4.14b). The angle onset for $\nu = +2$ filling insulating state starts around 1.12°, after the γLL is fully merged with VHS (Fig. 4.14c is not yet merged at $\nu = 2$). The angle onsets of the insulating regions for the conduction and valence bands (marked by dashed lines and arrows)

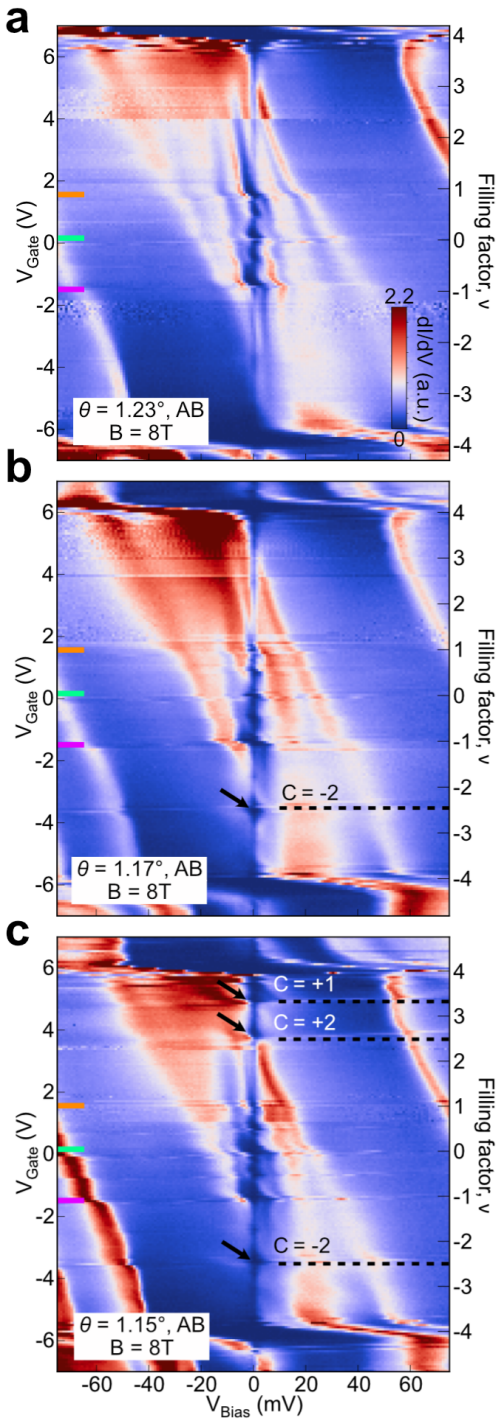

Figure 4.14: Band flattening and correlated Chern phases. a,b,c) $\theta = 1.23°$, $\theta = 1.17°$, $\theta = 1.15°$, respectively. Correlated Chern phases appear when the corresponding band becomes flat due to interactions.

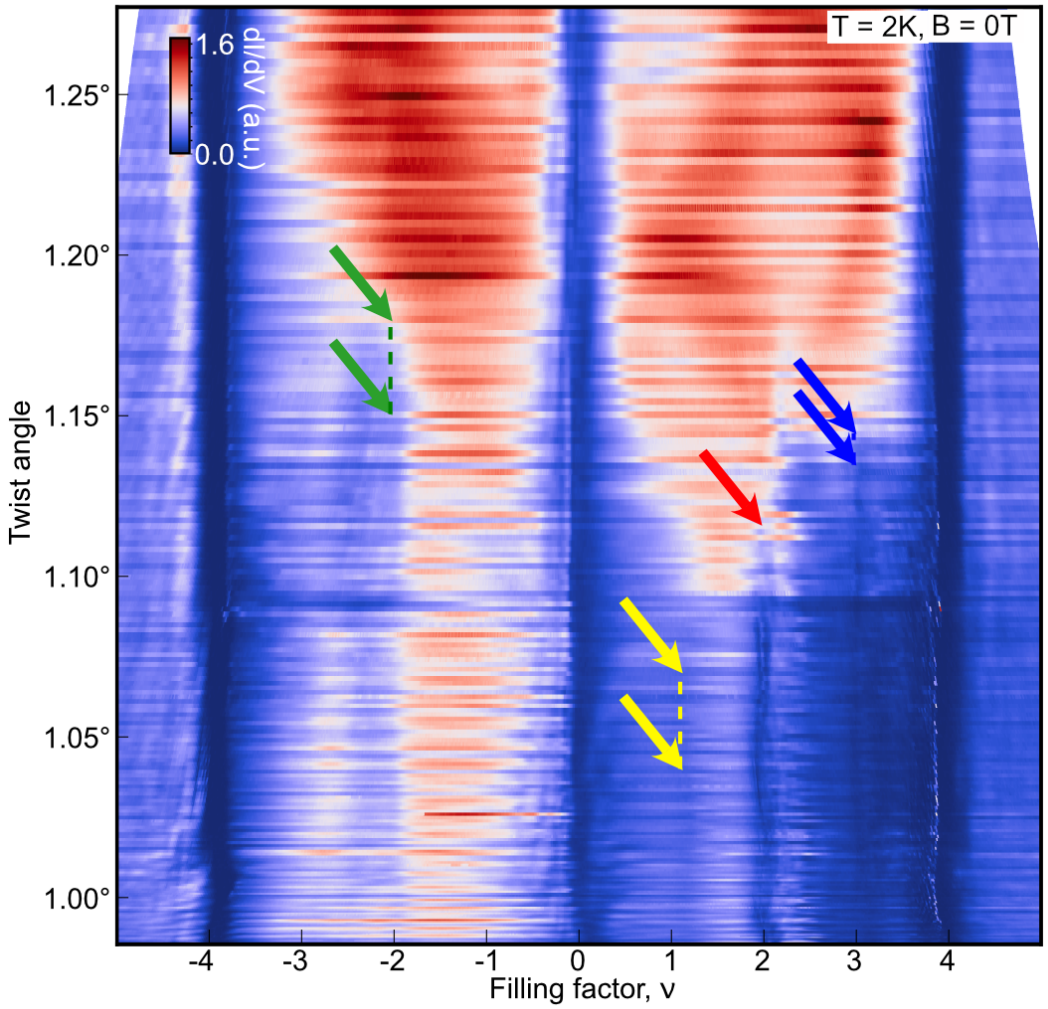

Figure 4.15: Mapping LDOS at zero bias as a function of twist angle and filling factors. Dark regions correspond to low LDOS or gapped regions. Correlated gaps at integer fillings are observed, their onsets marked by arrows.

have an electron-hole asymmetry that is also consistent with the band flattening.

Spectra at $\nu = \pm 2$ taken at various twist angles (Fig. 4.16) indeed show that LDOS suppressions originate from the development of a gap at the Fermi energy. And it also shows the $\nu = -2$ gap emerges at slightly higher angles—a further demonstration of electron-hole asymmetry. The maximal size of this half-filling gap is ~ 1.5 meV, slightly larger than the activation gap extracted from transport [10, 12, 50, 51], supporting that the gap we observe is indeed from the insulating gap considering spatial averaging from transport. We note that the LDOS suppression from the

observed gaps in Figure 4.16 may also be, in part, related to the Fermi surface reconstruction due to flavour symmetry-breaking cascade [48, 49]. Taken together, our observations suggest a close relation between band flattening, correlated gaps and cascade physics.

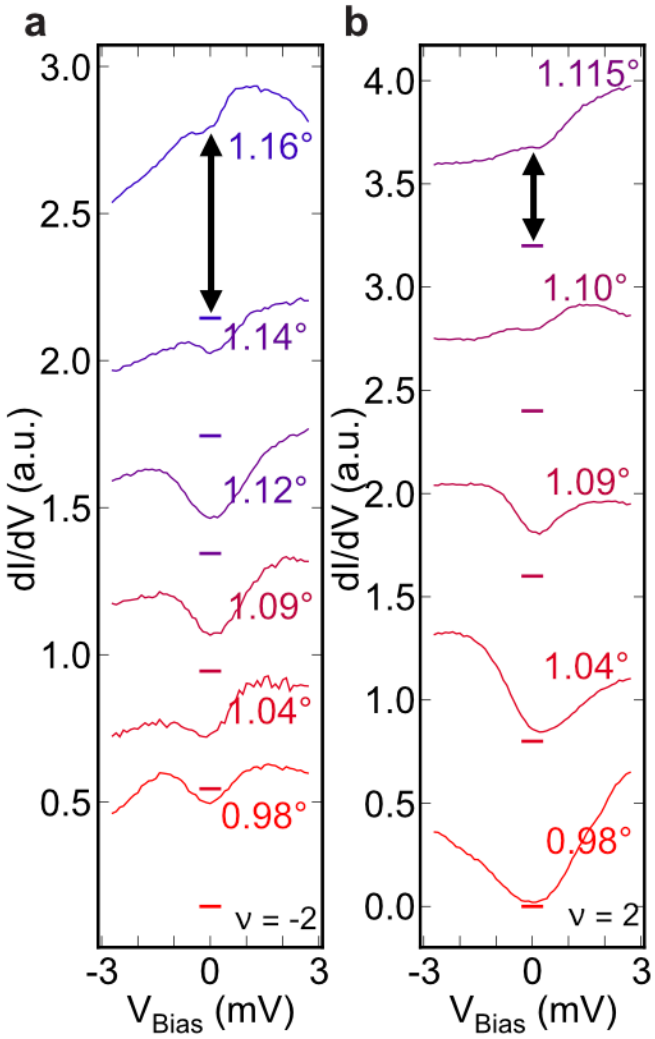

Figure 4.16: Correlated insulating gaps at $\nu = \pm 2$ at various angles. a) On the hole side, $\nu = -2$. b) On the electron side, $\nu = +2$.

4.6 Theoretical understanding on the angle onsets

A theory analysis of the continuum-model band structure [7, 37] with interactions treated at a mean-field level in part accounts for the observed band flattening and related symmetry-breaking cascade instabilities near the magic angle. While the doping dependence of the moiré band deformation at larger angles is well-modeled by

assuming only a Hartree correction (Fig. 4.10), near the magic angle a Hartree-only theory becomes insufficient: such theory cannot describe cascade, and, moreover, by construction it is equivalent to the non-interacting model at charge neutrality, thus predicting unrealistically small flat-band bandwidths. Fock terms, although difficult to include in a way that produces complete quantitative matching with the experiments [61, 69, 73, 74], alleviate some of these qualitative shortcomings.

Focusing only on the γ-pocket near the magic angle, Fock terms counteract Hartree-driven inversions and thereby may further stabilize band flattening. Regardless of the exact details, the band-flattening significantly amplifies the density of states (DOS) at the Fermi level (E_F) relative to expectations from non-interacting models (by up to a factor of ~ 4 for $\nu = 2$ and ~ 15 for $\nu = 3$ in our model); see Figure 4.17. This interaction-driven magnification of the already-substantial DOS around the VHS accordingly promotes the symmetry-breaking cascade of electronic transitions [48, 49].

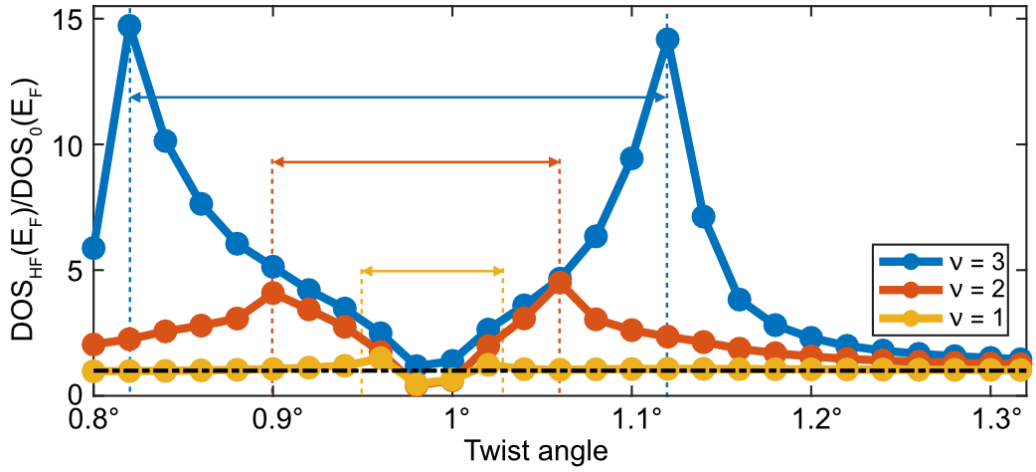

Figure 4.17: Enhanced DOS due to Hartree-Fock corrections. Compared to non-interacting case, the enhancement of DOS is more than 5 times for $\nu = 2, 3$, which significantly enhances correlations.

For a more quantitative treatment of the cascade instabilities, we compare the energies of unpolarized and flavor-polarized states at integer fillings for different twist angles. Depending on the model, a non-self-consistent treatment that neglects band renormalization predicts either spontaneous flavour polarization within a narrow window around the magic angle or no cascade at all. A self-consistent treatment that incorporates band flattening (Fig. 4.18), by contrast, exhibits cascade behaviour over broader twist-angle windows whose widths depend strongly on filling—in agree-

ment with experimental data on the electron-doped side of Fig. 4.15. These findings are also in agreement with recent theoretical calculations [72] that predict a broader twist-angle window where correlated physics is observed when band-flattening is taken into account.

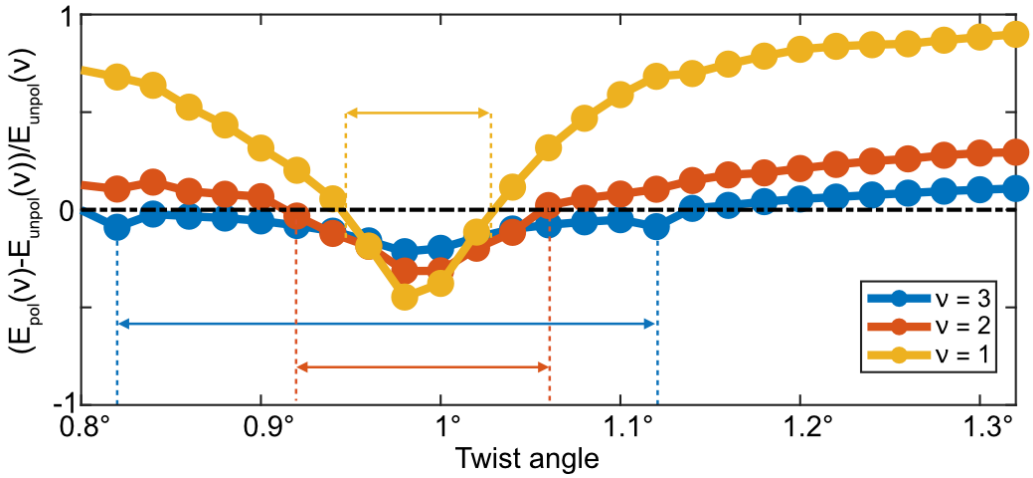

Figure 4.18: Increased range of angles that favors cascade of phase transitions. When Hartree-Fock corrections are added, the range significantly increases, compared to non-interacting cases.

4.7 Effect of heterostrain

As some papers note the role of heterostrain in the band structure, we systematically study how much the strain affects the band structure. We compare the VHS separation as a function of strain and angle. We took the VHS separation at full filling to exclude additional increase in the separation that happens at partial flat-band filling due to interactions (Figure 4.19a). Figure 4.19b shows that the VHS separation increases by $3.1 \pm 0.5\ meV$ per increase in 0.1% heterostrain in the twist angle range 1.01° - 1.06° . A similar value has been predicted from theory [30]. Because our sample has heterostrain of 0.15 - 0.3%, we expect an enhanced VHS separation of around 4 - 8 meV. This enhancement could potentially affect the onset of the cascade, but the role of the Hartree-driven band flattening remains. Robustness of the band-flattening physics stems from the fact that the nature of the inhomogenous charge distribution coming from different momentum points persists in a strained system as well. The interaction-driven band flattening mechanism is thus valid within the range of heterostrain.

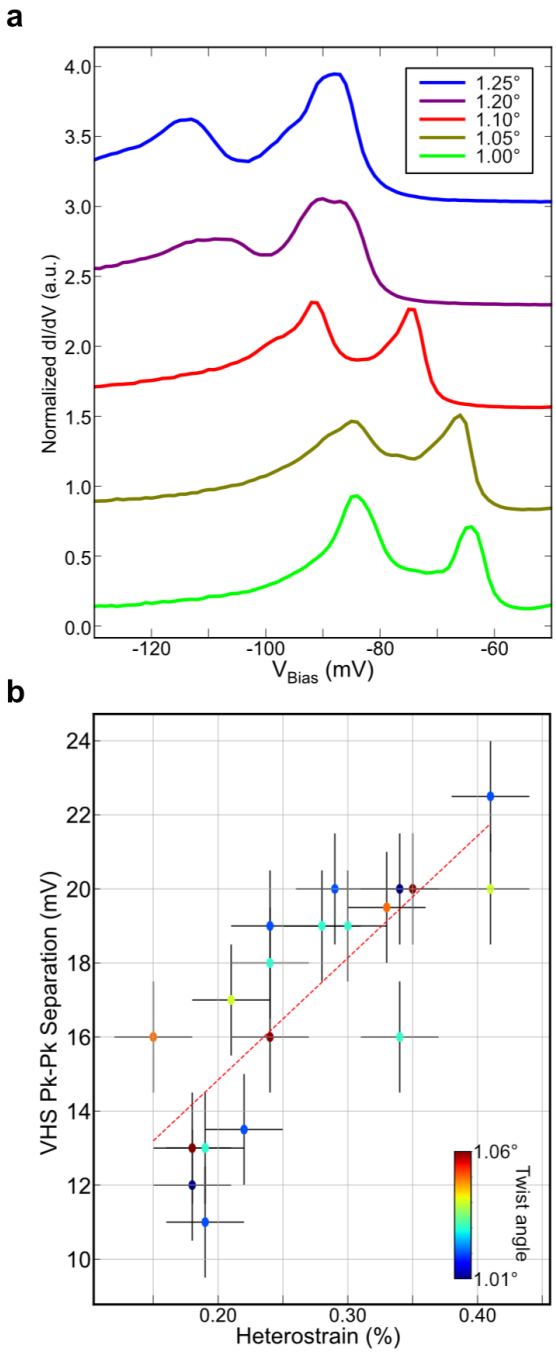

Figure 4.19: Effect of heterostrain. a) VHS separations at $\nu > +4$. b) The VHS separation linearly increases with heterostrain.

4.8 Conclusion

Our observations reconcile the apparent discrepancy between the predominance of interactions implied by the emergence of correlated phases around the magic angle

and previous measurements, including (i) a large Dirac velocity around the CNP [66], (ii) a total bandwidth exceeding 40 meV [28, 48, 53–55, 65], and (iii) a large separation of the VHSs [28, 53], that seem at odds with supposedly crucial aspects of the band theory predictions. These quantities—Dirac velocity, total bandwidth and the VHS separation—appear not to be essential. For example, Fig. 4.20 shows that the measured Dirac velocity and VHS separation are even smaller at 1.18° than 1.04°, while signatures of strongly correlated phases (e.g., symmetry-breaking cascade and correlated gaps) appear at the latter twist angle but not the former. Instead, we identify the interaction-driven flattening of the moiré bands around the γ pockets, with the consequent increase in the density of states, as the decisive feature needed for the formation of correlated phases.

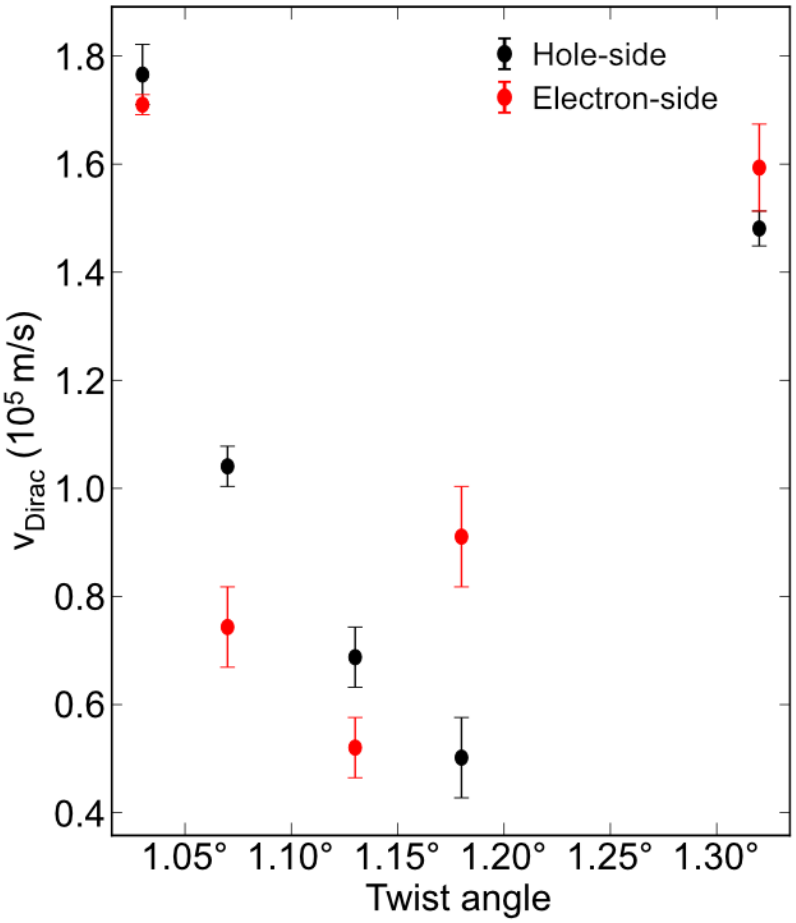

Figure 4.20: Dirac velocities at different twist angles. Note that 1.04° has larger Dirac velocities than 1.32°, where former shows correlated physics and latter does not.

Chapter 5

OUTLOOK

5.1 Search for superconductivity : a candidate

The central question around all the interesting phenomena in TBG is the question of superconductivity. What is the paring glue: phonon or a more exotic one? What is the paring symmetry? Can the mechanism of TBG superconductivity give any hint on understanding high temperature superconductivity? Since properties of superconductivity may be hidden in the spectroscopy of the superconducting gap, we have been searching for the signatures of superconductivity through STM.

We find gapped structures we suspect due to superconductivity. First, prominent LDOS suppressions at the Fermi level are visible in both the $2 < \nu < 3$ and $-3 < \nu < -2$ doping regions (Fig. 5.1).

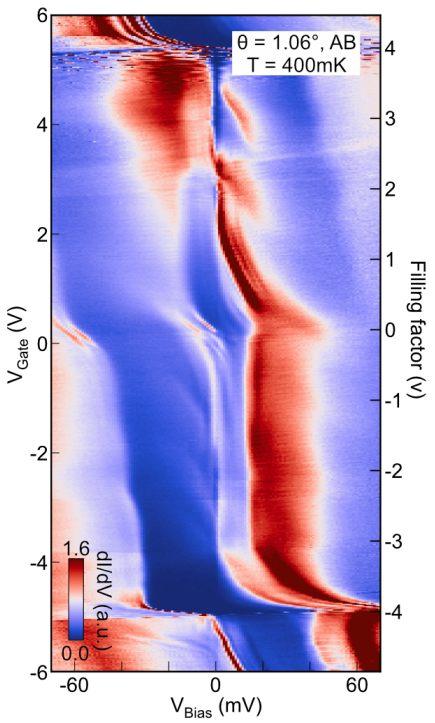

Figure 5.1: Gapped regions between $2 < \nu < 3$ and $-3 < \nu < -2$.

Of the two regions, the feature between $\nu = +2$ and $+3$ has a 'tilted V' shape

at small bias voltages, which can be largely understood as a consequence of the relative prominence of the flavor polarization in the conduction band compared to the valence band. There, two of the four flavors are pushed away from the Fermi energy by strong interactions [48], consistent with the LDOS being predominantly shifted to higher energy and resulting in an asymmetric spectrum down to the Fermi energy (Fig. 5.2a).

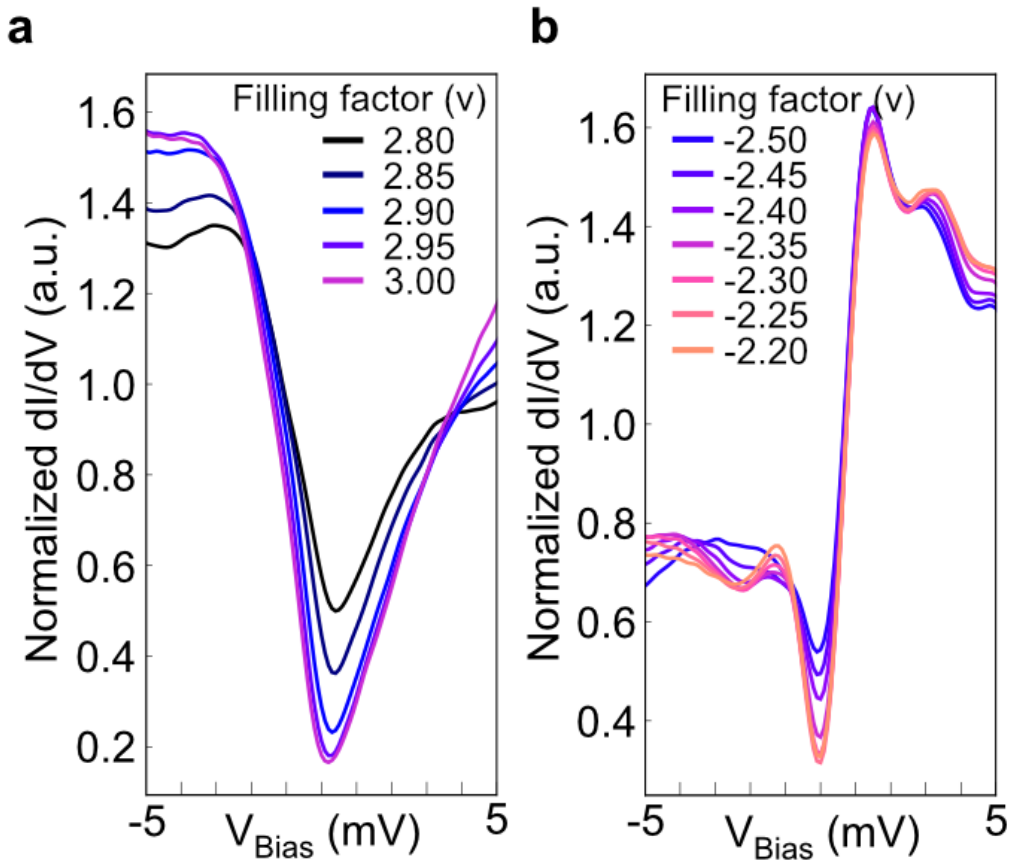

Figure 5.2: Shape of the gaps. a) $2 < \nu < 3$, the gap has an asymmetrically tilted V shape. b) $-3 < \nu < -2$, in addition to global asymmetry, there is a more symmetric gap at the low energy.

In contrast, the spectrum between $\nu = -2$ and -3 exhibits a slightly different shape that cannot be fully explained by a simple flavor-symmetry-breaking cascade that produces a large overall asymmetry. Additionally, this doping range also shows a clear, more symmetric gapped feature at small bias voltages (Fig. 5.2b). The fine resolution data focusing on this region shows that the corresponding gap spans almost the entire filling range $-3 < \nu < -2$ (Fig. 5.3).

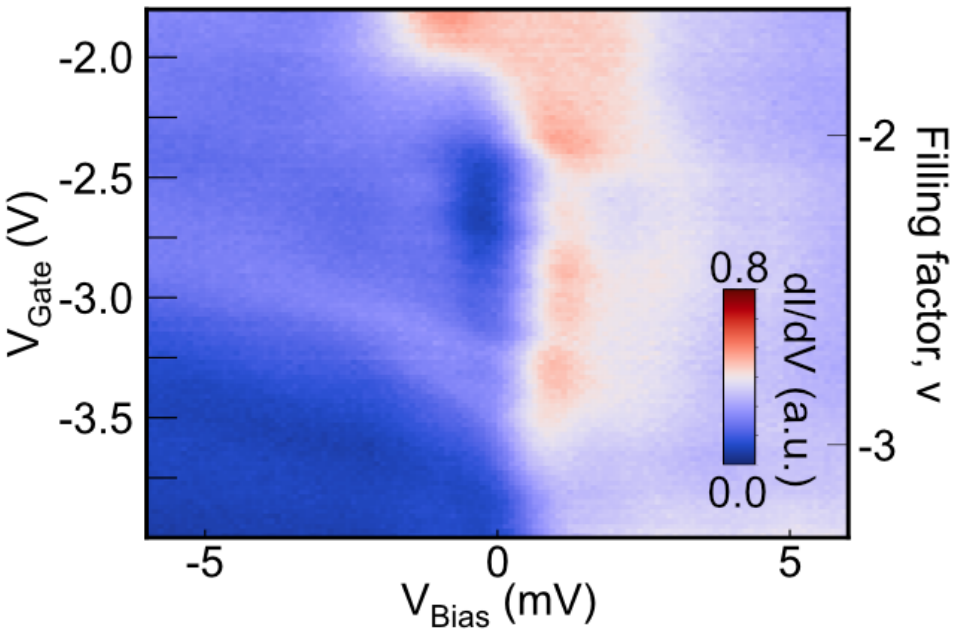

Figure 5.3: High resolution spectrum at $-3 < \nu < -2$.

The gap reaches its maximal size of $2\Delta \approx 1.1$ meV. Also, it becomes prominent only below $\theta = 1.16°$, and gradually recedes with temperature and disappears above 5 K (Fig. 5.4). The gap size as well the temperature dependence of this feature is similar to the gap at $\nu = -2$; however, the filling range observed here is unusually large. Importantly, the gap exists over a filling range that superconductivity has been observed in transport at similar angles for TBG on WSe_2 [50] as well as in many hBN-only encapsulated devices [11, 12, 51]. This correspondence indicates that the observed feature may be related to superconductivity itself or signals the possible existence of a pseudo-gap phase that precedes superconductivity [75]. Regardless of its exact origin, the pronounced suppression (instead of increase) of the LDOS near the Fermi energy, together with symmetry-breaking cascade features, for fillings where superconductivity is anticipated may suggest either an electronic pairing origin [76] or a regime of strong-coupling superconductivity as recently pointed out for magic-angle trilayer graphene [77, 78].

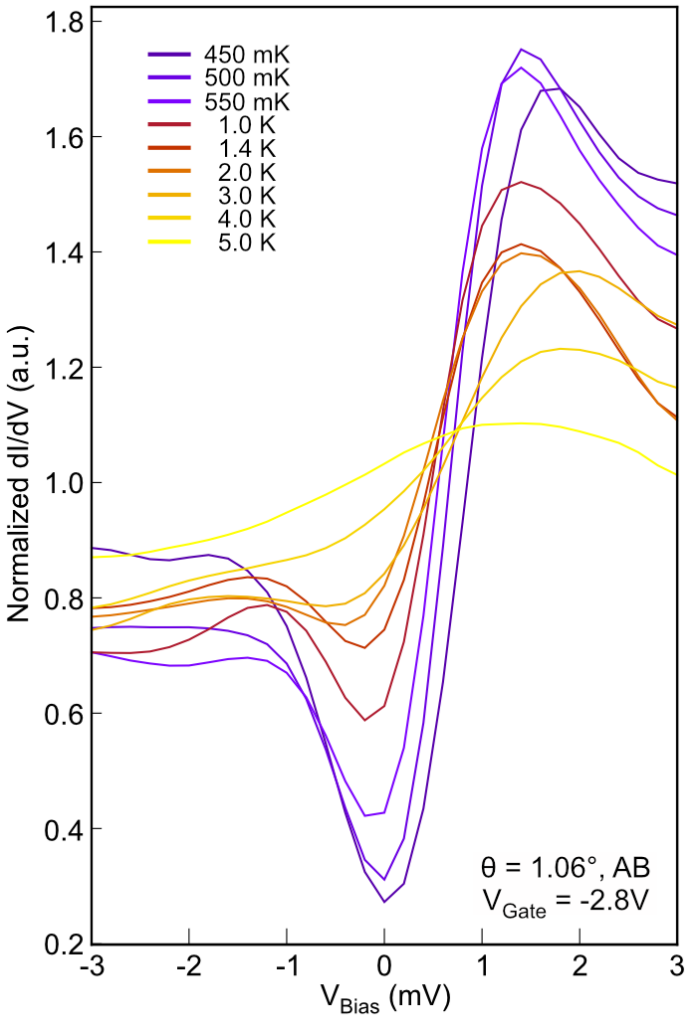

Figure 5.4: Temperature dependence of the gap. It vanishes around 5K.

5.2 Superconductivity in a similar moiré system : magic angle twisted trilayer graphene

In general, twisted-N-layer graphene can host a flat band similar to the twisted bilayer graphene, with slight modification of the band structure. One example is magic angle twisted trilayer graphene (MATTG). Calculations [79] predicted that the mirror symmetric stacking of three graphene sheets — top and the bottom are un-rotated but the middle one is rotated by θ (Fig. 5.5), the band structure consists of a flat band and a dispersive Dirac cone, and the magic angle is around 1.5°, 50% larger than the MATBG.

Park et al. [77] and Hao et al. [78] reported that phenomenology of MATTG

Figure 5.5: Schematic of twisted trilayer graphene. Middle layer is rotated by θ.

is similar to MATBG, including superconductivity around $2 < \nu < 3$ and $-3 < \nu < -2$, or cascade of phase transitions around integer fillings and resistive states. Additional feature compared to MATBG is that this system has a clear tunability of superconductivity with the displacement field.

One of the practical properties about the MATTG is that the superconductivity is more robust than MATBG. The critical temperature and magnetic field are slightly higher. T_{BKT} reaches as high as 2.2 K in MATTG, where in MATBG the typical highest value is only around 1 K, giving hope that spectroscopic signature of superconductivity might also be more robust in MATTG.

Topography

With that in mind, we measure MATTG with our STM. Topography that shows the moiré pattern looks very similar to the topography of TBG (Fig. 5.6). The moiré wavelength is around 10 nm, which corresponds to the twist angle of around 1.5°. Spectroscopy as a function of doping also looks very similar to MATBG (Fig. 5.7), although the twist angle is very different (1.1° for MATBG and 1.5° for MATTG).

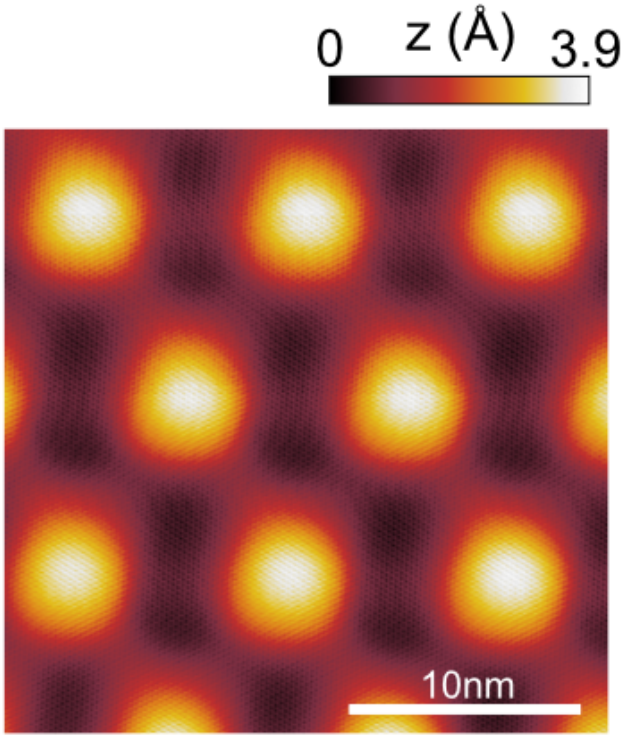

Figure 5.6: Topography of MATTG. Moiré wavelength is around 10 nm.

Spectroscopy

The two Van Hove singularities originating from the flat bands, detected as peaks in $dI/dV \sim LDOS$, are separated further apart at the charge neutrality point (CNP, $\nu = 0$) compared to full filling of four electrons (holes) per moiré unit cell ($\nu = \pm 4$). This factor of five increase in VHSs separation indicates that the flat band structure is largely determined by the electronic correlations [53]. Note that in MATTG shorter moiré length is expected to result in even stronger electron-electron interactions. The enhanced separation between VHSs has not been observed in TBG at similar twist angles of around 1.5°. Moreover, a well-developed cascade of flavor symmetry breaking phase transitions [48, 49] is also observed (Fig. 5.7).

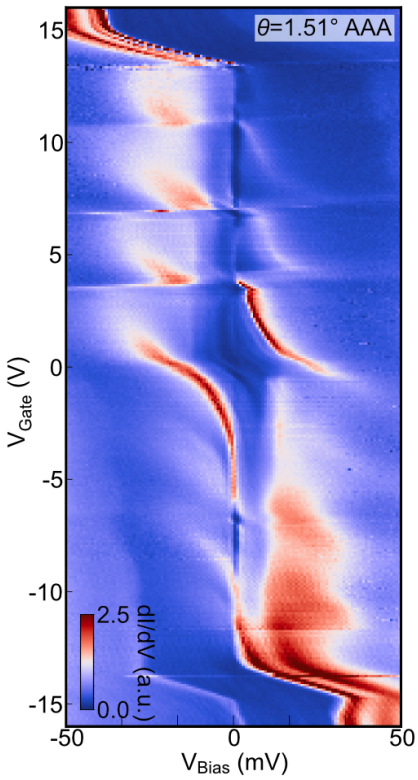

Figure 5.7: Spectroscopy of MATTG taken on a topographic peak (AAA site) at 1.51° as a function of doping.

Superconductivity in MATTG

Similar to Figure 5.3 from MATBG, gapped feature is pronounced between $-3 < \nu < -2$. In this range, transport studies established superconductivity [77, 78]. The gaps are observed in two separate regions of doping, a smaller region between $\nu = -1.9$ and $\nu = -2.1$) and a larger one between $\nu = -2.2$ and $\nu = -3$ (Fig. 5.8). The smaller region is convoluted with the correlated gap from insulating state since it is accompanied by Coulomb diamonds and nearly horizontal resonance peaks, signaling existence of a quantum dot [66]. Moreover, the center of this region coincides with $\nu = -2$ which is directly pinpointed by the LDOS Landau fan

diagram, agreeing with the increase in resistance at $\nu = -2$ [77, 78]. We emphasize that in both gapped regions, gaps necessarily originate from correlations effects as any trival gap coming from the band structure effects will shift away from the Fermi energy with doping.

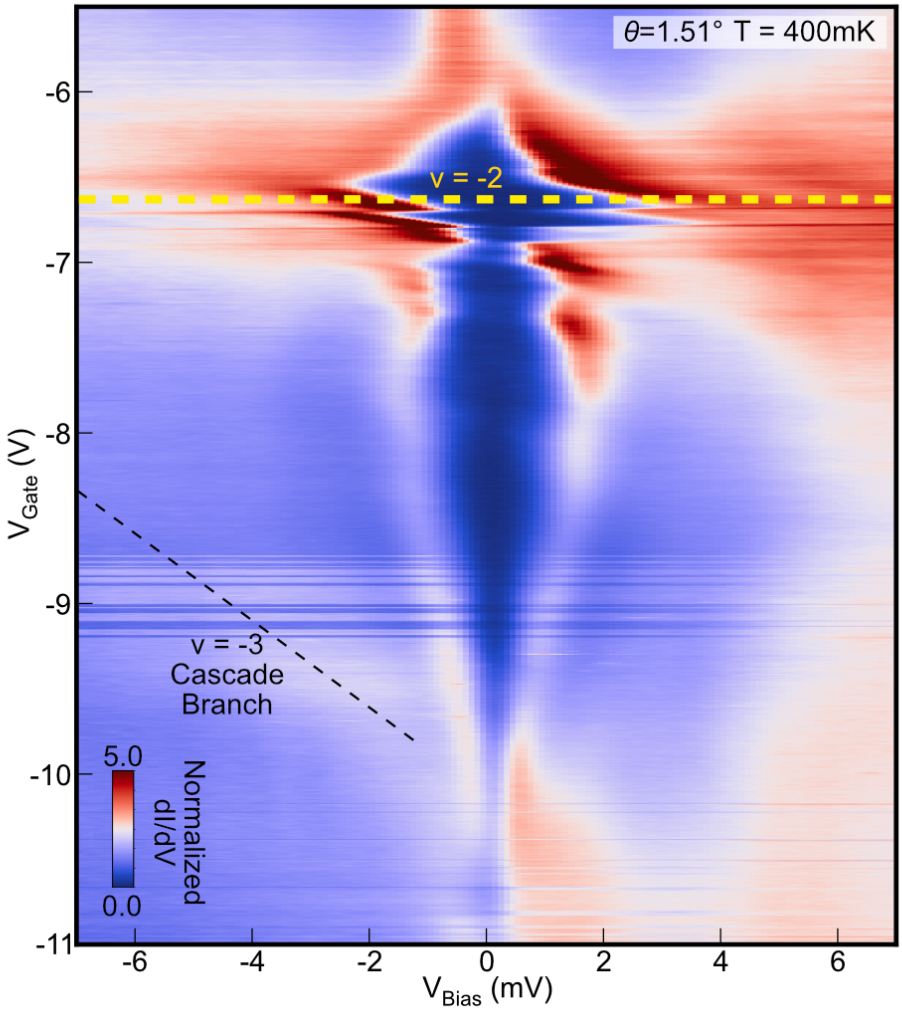

Figure 5.8: Superconducting gap of MATTG around $\nu \sim -2$ at $\theta = 1.51°$.

In the following we focus on this larger region where the gap is well-pinned to the Fermi energy. Strikingly, this gap is accompanied by peak structures. The development such sharp narrow peaks, strongly resemble coherence peaks occurring in superconductors and are difficult to explain by other mechanisms. We thus attribute the observed gap and corresponding coherence peaks in the larger doping region (from $\nu = -2.2$ to $\nu = -3$) to superconductivity in MATTG. Note that in 5.3,

sharp coherence peaks were missing in MATBG, possibly due to weaker strength of superconductivity.

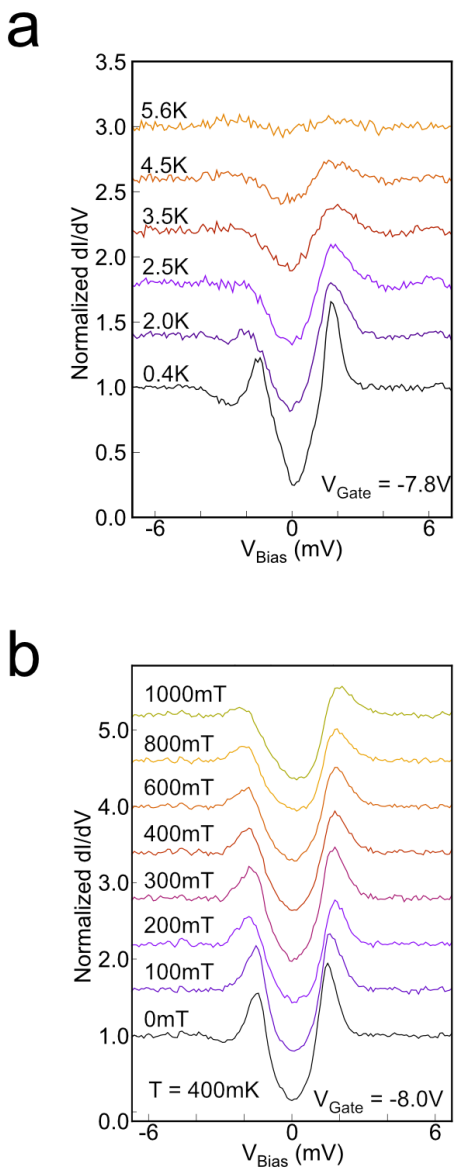

Figure 5.9: Temperature (a) and Magnetic field (b) dependence of the superconducting gap.

To further check whether the gap and corresponding coherence peaks are indeed

consistent with the expectation of superconductivity in this system, we characterize the gap evolution with temperature and magnetic field (Fig. 5.9). As the temperature and magnetic field are increased, we observed that coherence peaks on the both sides of E_F subside sharply.

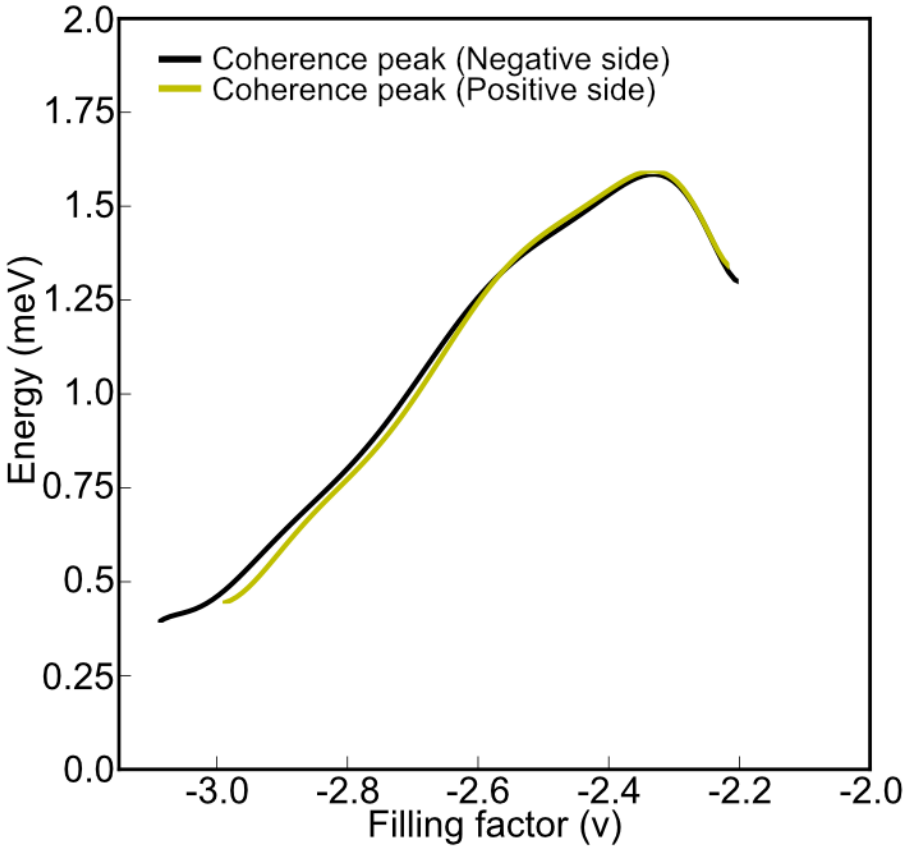

Figure 5.10: Doping dependence of the gap size.

By defining peak-to-peak distance as 2Δ, we plot doping dependence of Δ (Fig. 5.10). We find that the gap size peaks around $\nu = -2.4$. This observation resembles with the doping dependence of the critical temperature T_C [77, 78], also peaking around $\nu \approx -2.4$. However, putting $\Delta \approx 1.6\ meV$ and taking upper limit for superconductivity $T_C \approx 2 - 3\ K$ yields $2\Delta/k_B T_C \approx 13$ which exceeds conventional BCS value (~ 4) by a factor of ~ 3, highlighting possible unconventional nature of

superconductivity in MATTG.

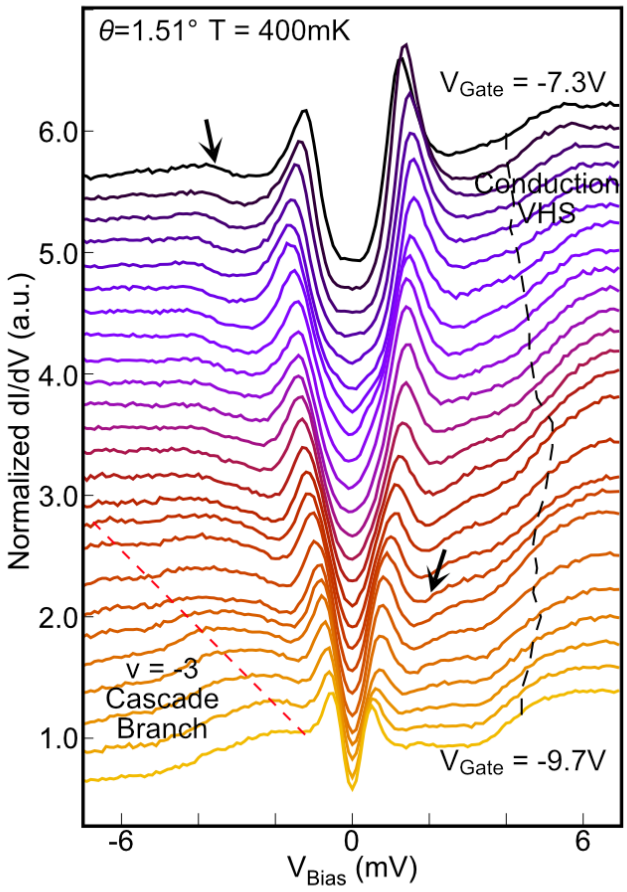

Figure 5.11: Dip-hump structure at different gate voltages.

Dip-hump structure

In addition to gaped regions and corresponding coherence peaks, we observe features that is closely associated to superconductivity. In the large range of doping, we can resolve clear dip-hump structures outside the gap, which are usually interpreted as the signature of a bosonic excitation due to superconducting glue. The mode at energy $E = \Delta + \Omega$ (Δ is the superconducting gap and Ω the excitation energy) is a signature of strongly coupled superconductivity. In unconventional superconductors, such as cuprate [80–82], the features have given insights on paring mediators. In Figure 5.11, clear dip-hump structures are present at different gate voltages. The structure

only exists at the the superconducting pocket and the positive dip and negative dip are nearly symmetric in energy, ruling out the possibility that the dip-hump is intrinsic to DOS (or background effect) (Fig. 5.12a).

We measure the energy of the mode $\Omega = E - \Delta$ as a function of doping (Fig. 5.12a). Moreover, as shown in Fig. 5.12b, $\Omega/(2\Delta)$ is anticorrelated with the gap and bounded to be less than 1, similar to other unconventional superconductors [80–82].

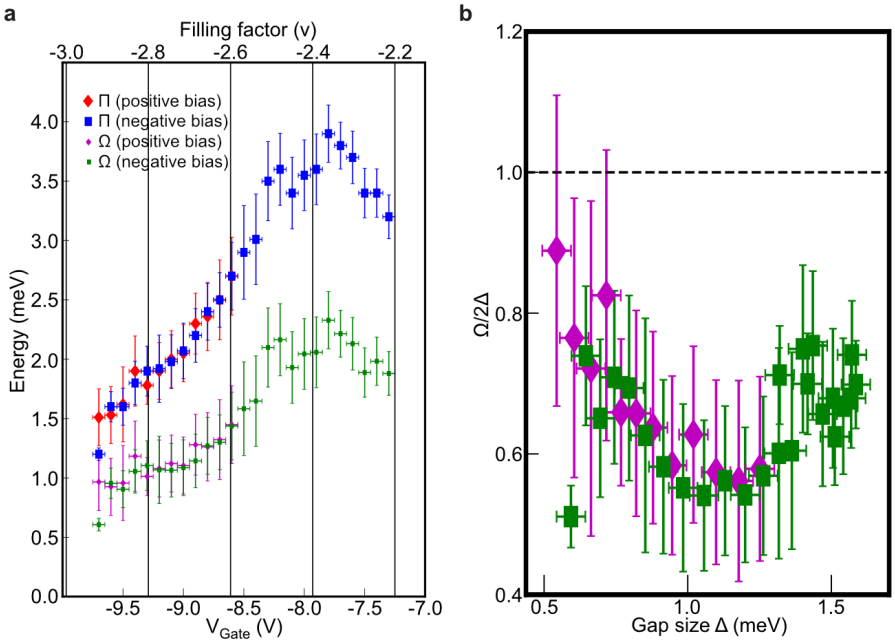

Figure 5.12: Energetics of the dip-hump structure. a) Ω as a function of doping, b) anticorrelation between $\Omega/(2\Delta)$ and Δ.

Looking forward, having identified the superconductivity spectroscopically, several measurements can be done in the future to answer some of the questions regarding

the nature of superconductivity. We hope that further analysis such as the shape of the superconducting gap, behavior of the gap under magnetic or non-magnetic impurities, and spatial distribution of the superconducting gap and dip-hump structures, would shed light on this unconventional superconductivity.

5.3 Possible experimental techniques to study superconductivity

In situ measurement of transport and STM

A MATBG or MATTG device that is capable of both STM measurement and electrical transport measurement would give additional information. Many different aspects that have been observed in MATBG, such as quantized anomalous Hall effect, nematic superconducting behavior, percolating superconductivity and percolating quantum Hall states can be directly connected and visualized to STM's spatial and spectroscopic abilities.

Also, to verify if the identified $-3 < \nu < -2$ gap is indeed from superconductivity, we could simultaneously measure gaps and superconductivity from transport, changing temperatures and magnetic fields. The resulting trend or alignment would tell whether the gap is indeed related to superconductivity.

Shot noise with STM

From measuring shot noise, effective charge can be measured. In fractional quantum Hall effect, the 1/3 state is predicted to have fractional charge 1/3e. Using shot noise through a junction, experiments showed that indeed that was the case [83]. For superconductivity, due to Andreev reflextion the effective amount of charge becomes 2e when a system turns from normal to superconducting state. Recently, STM has been used to measure such a shot noise and identify superconductivity [84].

In addition to the gap we found, measuring 2e from the shot noise can be alternative signature for superconductivity in MATBG, and give a way to relate the gap and superconductivity. Bastiaans et al. used shot noise measurement with STM and found that superconducting pairing survives even above the critical temperature in a thin film superconductor [85]. It is interesting to search for similar phenomena in TBG since the superconducrtivity in MATBG is likely to be highly unconventional.

5.4 Pomeranchuk effect and nematicity

Another interesting observation we have in MATBG is that, while the gap-like features at the Fermi energy become weaker with increasing temperature, features at

higher energies—previously identified to be related to flavor symmetry breaking transitions—are enhanced; see the temperature evolution in Figure 5.13. The relation of these features and various recently reported phases that emerge at elevated temperatures [86, 87] remains a subject for future investigations.

Cao et al. [88] found that at very narrow angle ranges, superconductivity seems to be nematic, adding another interesting possible phases in MATBG. Few is known why this directional difference occurs. In Chapter 2, we showed that there is a spatially preferred direction with energies. It will be interesting to see if there is any relation between those nematic behaviors.

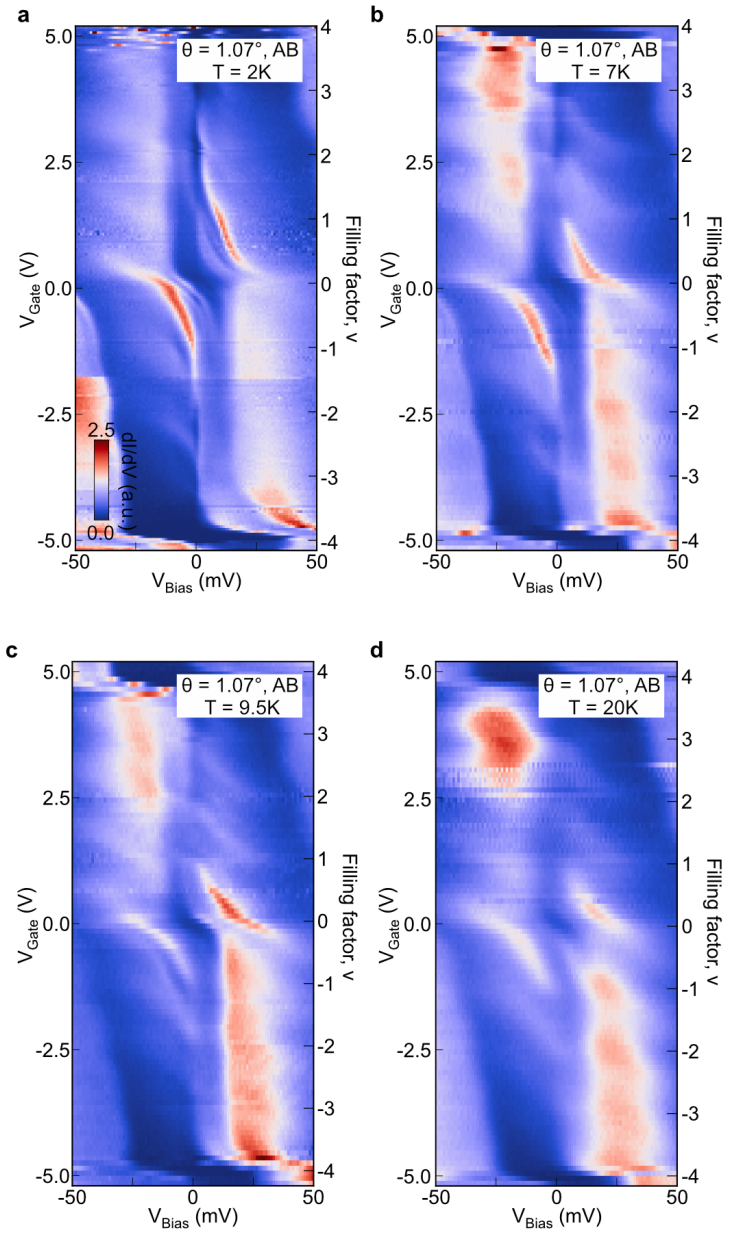

Figure 5.13: Temperature dependence of cascade of phase transitions. a,b,c,d) 2K, 7K, 9.5K, 20K, respectively.

Bibliography

[1] Yuanbo Zhang, Yan-Wen Tan, Horst L. Stormer, and Philip Kim. Experimental observation of the quantum Hall effect and Berry's phase in graphene. *Nature*, 438(7065):201–204, 2005.

[2] K. S. Novoselov, A. K. Geim, S. V. Morozov, D. Jiang, M. I. Katsnelson, I. V. Grigorieva, S. V. Dubonos, and A. A. Firsov. Two-dimensional gas of massless Dirac fermions in graphene. *Nature*, 438(7065):197–200, 2005.

[3] Kirill I. Bolotin, Fereshte Ghahari, Michael D. Shulman, Horst L. Stormer, and Philip Kim. Observation of the fractional quantum Hall effect in graphene. *Nature*, 462(7270):196–199, 2009.

[4] Xu Du, Ivan Skachko, Fabian Duerr, Adina Luican, and Eva Y. Andrei. Fractional quantum Hall effect and insulating phase of Dirac electrons in graphene. *Nature*, 462(7270):192–195, 2009.

[5] J. M. B. Lopes dos Santos, N. M. R. Peres, and A. H. Castro Neto. Graphene Bilayer with a Twist: Electronic Structure. *Physical Review Letters*, 99(25):256802, 2007.

[6] E. Suárez Morell, J. D. Correa, P. Vargas, M. Pacheco, and Z. Barticevic. Flat bands in slightly twisted bilayer graphene: Tight-binding calculations. *Physical Review B*, 82(12):121407, 2010.

[7] Rafi Bistritzer and Allan H. MacDonald. Moiré bands in twisted double-layer graphene. *Proceedings of the National Academy of Sciences*, 108(30):12233–12237, 2011.

[8] Kyounghwan Kim, Matthew Yankowitz, Babak Fallahazad, Sangwoo Kang, Hema C. P. Movva, Shengqiang Huang, Stefano Larentis, Chris M. Corbet, Takashi Taniguchi, Kenji Watanabe, Sanjay K. Banerjee, Brian J. LeRoy, and Emanuel Tutuc. van der Waals Heterostructures with High Accuracy Rotational Alignment. *Nano Letters*, 16(3):1989–1995, 2016.

[9] Y. Cao, J. Y. Luo, V. Fatemi, S. Fang, J. D. Sanchez-Yamagishi, K. Watanabe, T. Taniguchi, E. Kaxiras, and P. Jarillo-Herrero. Superlattice-Induced Insulating States and Valley-Protected Orbits in Twisted Bilayer Graphene. *Physical Review Letters*, 117(11):116804, 2016.

[10] Yuan Cao, Valla Fatemi, Ahmet Demir, Shiang Fang, Spencer L. Tomarken, Jason Y. Luo, Javier D. Sanchez-Yamagishi, Kenji Watanabe, Takashi Taniguchi, Efthimios Kaxiras, Ray C. Ashoori, and Pablo Jarillo-Herrero. Correlated insulator behaviour at half-filling in magic-angle graphene superlattices. *Nature*, 556(7699):80–84, 2018.

[11] Yuan Cao, Valla Fatemi, Shiang Fang, Kenji Watanabe, Takashi Taniguchi, Efthimios Kaxiras, and Pablo Jarillo-Herrero. Unconventional superconductivity in magic-angle graphene superlattices. *Nature*, 556(7699):43–50, 2018.

[12] Matthew Yankowitz, Shaowen Chen, Hryhoriy Polshyn, Yuxuan Zhang, K. Watanabe, T. Taniguchi, David Graf, Andrea F. Young, and Cory R. Dean. Tuning superconductivity in twisted bilayer graphene. *Science*, 363(6431):eaav1910, 2019.

[13] Aaron L. Sharpe, Eli J. Fox, Arthur W. Barnard, Joe Finney, Kenji Watanabe, Takashi Taniguchi, M. A. Kastner, and David Goldhaber-Gordon. Emergent ferromagnetism near three-quarters filling in twisted bilayer graphene. *Science*, 365(6453):605–608, 2019.

[14] M. Serlin, C. L. Tschirhart, H. Polshyn, Y. Zhang, J. Zhu, K. Watanabe, T. Taniguchi, L. Balents, and A. F. Young. Intrinsic quantized anomalous Hall effect in a moiré heterostructure. *Science*, 367(6480):900–903, 2020.

[15] C. L. Tschirhart, M. Serlin, H. Polshyn, A. Shragai, Z. Xia, J. Zhu, Y. Zhang, K. Watanabe, T. Taniguchi, M. E. Huber, and A. F. Young. Imaging orbital ferromagnetism in a moiré Chern insulator. *Science*, 372(6548):1323–1327, 2021.

[16] M. Z. Hasan and C. L. Kane. Colloquium: Topological insulators. *Reviews of Modern Physics*, 82(4):3045–3067, 2010.

[17] Guohong Li, A. Luican, J. M. B. Lopes dos Santos, A. H. Castro Neto, A. Reina, J. Kong, and E. Y. Andrei. Observation of Van Hove singularities in twisted graphene layers. *Nature Physics*, 6(2):109–113, 2010.

[18] I. Brihuega, P. Mallet, H. González-Herrero, G. Trambly de Laissardière, M. M. Ugeda, L. Magaud, J. M. Gómez-Rodríguez, F. Ynduráin, and J.-Y. Veuillen. Unraveling the Intrinsic and Robust Nature of van Hove Singularities in Twisted Bilayer Graphene by Scanning Tunneling Microscopy and Theoretical Analysis. *Physical Review Letters*, 109(19):196802, 2012.

[19] Dillon Wong, Yang Wang, Jeil Jung, Sergio Pezzini, Ashley M. DaSilva, Hsin-Zon Tsai, Han Sae Jung, Ramin Khajeh, Youngkyou Kim, Juwon Lee, Salman Kahn, Sajjad Tollabimazraehno, Haider Rasool, Kenji Watanabe, Takashi Taniguchi, Alex Zettl, Shaffique Adam, Allan H. MacDonald, and Michael F. Crommie. Local spectroscopy of moiré-induced electronic structure in gate-tunable twisted bilayer graphene. *Physical Review B*, 92(15):155409, 2015.

[20] Kyounghwan Kim, Ashley DaSilva, Shengqiang Huang, Babak Fallahazad, Stefano Larentis, Takashi Taniguchi, Kenji Watanabe, Brian J. LeRoy, Allan H. MacDonald, and Emanuel Tutuc. Tunable moiré bands and strong correlations in small-twist-angle bilayer graphene. *Proceedings of the National Academy of Sciences*, 114(13):3364–3369, 2017.

[21] David L. Miller, Kevin D. Kubista, Gregory M. Rutter, Ming Ruan, Walt A. de Heer, Phillip N. First, and Joseph A. Stroscio. Observing the Quantization of Zero Mass Carriers in Graphene. *Science*, 324(5929):924–927, 2009.

[22] Suyong Jung, Gregory M. Rutter, Nikolai N. Klimov, David B. Newell, Irene Calizo, Angela R. Hight-Walker, Nikolai B. Zhitenev, and Joseph A. Stroscio. Evolution of microscopic localization in graphene in a magnetic field from scattering resonances to quantum dots. *Nature Physics*, 7(3):245–251, 2011.

[23] C. R. Dean, A. F. Young, I. Meric, C. Lee, L. Wang, S. Sorgenfrei, K. Watanabe, T. Taniguchi, P. Kim, K. L. Shepard, and J. Hone. Boron nitride substrates for high-quality graphene electronics. *Nature Nanotechnology*, 5(10):722–726, 2010.

[24] Jiamin Xue, Javier Sanchez-Yamagishi, Danny Bulmash, Philippe Jacquod, Aparna Deshpande, K. Watanabe, T. Taniguchi, Pablo Jarillo-Herrero, and Brian J. LeRoy. Scanning tunnelling microscopy and spectroscopy of ultra-flat graphene on hexagonal boron nitride. *Nature Materials*, 10(4):282–285, 2011.

[25] Régis Decker, Yang Wang, Victor W. Brar, William Regan, Hsin-Zon Tsai, Qiong Wu, William Gannett, Alex Zettl, and Michael F. Crommie. Local Electronic Properties of Graphene on a BN Substrate via Scanning Tunneling Microscopy. *Nano Letters*, 11(6):2291–2295, 2011.

[26] Jungseok Chae, Suyong Jung, Andrea F. Young, Cory R. Dean, Lei Wang, Yuanda Gao, Kenji Watanabe, Takashi Taniguchi, James Hone, Kenneth L. Shepard, Phillip Kim, Nikolai B. Zhitenev, and Joseph A. Stroscio. Renormalization of the Graphene Dispersion Velocity Determined from Scanning Tunneling Spectroscopy. *Physical Review Letters*, 109(11):116802, 2012.

[27] Loïc Huder, Alexandre Artaud, Toai Le Quang, Guy Trambly de Laissardière, Aloysius G. M. Jansen, Gérard Lapertot, Claude Chapelier, and Vincent T. Renard. Electronic Spectrum of Twisted Graphene Layers under Heterostrain. *Physical Review Letters*, 120(15):156405, 2018.

[28] Alexander Kerelsky, Leo J. McGilly, Dante M. Kennes, Lede Xian, Matthew Yankowitz, Shaowen Chen, K. Watanabe, T. Taniguchi, James Hone, Cory Dean, Angel Rubio, and Abhay N. Pasupathy. Maximized electron interactions at the magic angle in twisted bilayer graphene. *Nature*, 572(7767):95–100, 2019.

[29] Nguyen N. T. Nam and Mikito Koshino. Lattice relaxation and energy band modulation in twisted bilayer graphene. *Physical Review B*, 96(7):075311, 2017.

[30] Zhen Bi, Noah F. Q. Yuan, and Liang Fu. Designing flat bands by strain. *Physical Review B*, 100(3):035448, 2019.

[31] Young Jae Song, Alexander F. Otte, Young Kuk, Yike Hu, David B. Torrance, Phillip N. First, Walt A. de Heer, Hongki Min, Shaffique Adam, Mark D. Stiles, Allan H. MacDonald, and Joseph A. Stroscio. High-resolution tunnelling spectroscopy of a graphene quartet. *Nature*, 467(7312):185–189, 2010.

[32] Liujun Zou, Hoi Chun Po, Ashvin Vishwanath, and T. Senthil. Band structure of twisted bilayer graphene: Emergent symmetries, commensurate approximants, and Wannier obstructions. *Physical Review B*, 98(8):085435, 2018.

[33] Hoi Chun Po, Liujun Zou, Ashvin Vishwanath, and T. Senthil. Origin of Mott Insulating Behavior and Superconductivity in Twisted Bilayer Graphene. *Physical Review X*, 8(3):031089, 2018.

[34] Hoi Chun Po, Liujun Zou, T. Senthil, and Ashvin Vishwanath. Faithful tight-binding models and fragile topology of magic-angle bilayer graphene. *Physical Review B*, 99(19):195455, 2019.

[35] Jian Kang and Oskar Vafek. Symmetry, Maximally Localized Wannier States, and a Low-Energy Model for Twisted Bilayer Graphene Narrow Bands. *Physical Review X*, 8(3):031088, 2018.

[36] Jian Kang and Oskar Vafek. Strong Coupling Phases of Partially Filled Twisted Bilayer Graphene Narrow Bands. *Physical Review Letters*, 122(24):246401, 2019.

[37] Mikito Koshino, Noah F. Q. Yuan, Takashi Koretsune, Masayuki Ochi, Kazuhiko Kuroki, and Liang Fu. Maximally Localized Wannier Orbitals and the Extended Hubbard Model for Twisted Bilayer Graphene. *Physical Review X*, 8(3):031087, 2018.

[38] Francisco Guinea and Niels R. Walet. Electrostatic effects, band distortions, and superconductivity in twisted graphene bilayers. *Proceedings of the National Academy of Sciences*, 115(52):201810947, 2018.

[39] Kasra Hejazi, Chunxiao Liu, Hassan Shapourian, Xiao Chen, and Leon Balents. Multiple topological transitions in twisted bilayer graphene near the first magic angle. *Physical Review B*, 99(3):035111, 2019.

[40] M. P. Lilly, K. B. Cooper, J. P. Eisenstein, L. N. Pfeiffer, and K. W. West. Anisotropic States of Two-Dimensional Electron Systems in High Landau Levels: Effect of an In-Plane Magnetic Field. *Physical Review Letters*, 83(4):824–827, 1999.

[41] Benjamin E. Feldman, Mallika T. Randeria, András Gyenis, Fengcheng Wu, Huiwen Ji, R. J. Cava, Allan H. MacDonald, and Ali Yazdani. Observation of a nematic quantum Hall liquid on the surface of bismuth. *Science*, 354(6310):316–321, 2016.

[42] A L Efros. Coulomb gap in disordered systems. *Journal of Physics C: Solid State Physics*, 9(11):2021, 1976.

[43] R. C. Ashoori, J. A. Lebens, N. P. Bigelow, and R. H. Silsbee. Equilibrium tunneling from the two-dimensional electron gas in GaAs: Evidence for a magnetic-field-induced energy gap. *Physical Review Letters*, 64(6):681–684, 1990.

[44] J. P. Eisenstein, L. N. Pfeiffer, and K. W. West. Coulomb barrier to tunneling between parallel two-dimensional electron systems. *Physical Review Letters*, 69(26):3804–3807, 1992.

[45] O. E. Dial, R. C. Ashoori, L. N. Pfeiffer, and K. W. West. High-resolution spectroscopy of two-dimensional electron systems. *Nature*, 448(7150):176–179, 2007.

[46] Ye-Heng Song, Zhen-Yu Jia, Dongqin Zhang, Xin-Yang Zhu, Zhi-Qiang Shi, Huaiqiang Wang, Li Zhu, Qian-Qian Yuan, Haijun Zhang, Ding-Yu Xing, and Shao-Chun Li. Observation of Coulomb gap in the quantum spin Hall candidate single-layer 1T'-WTe2. *Nature Communications*, 9(1):4071, 2018.

[47] Byoung Hee Moon, Jung Jun Bae, Min-Kyu Joo, Homin Choi, Gang Hee Han, Hanjo Lim, and Young Hee Lee. Soft Coulomb gap and asymmetric scaling towards metal-insulator quantum criticality in multilayer MoS2. *Nature Communications*, 9(1):2052, 2018.

[48] U. Zondiner, A. Rozen, D. Rodan-Legrain, Y. Cao, R. Queiroz, T. Taniguchi, K. Watanabe, Y. Oreg, F. von Oppen, Ady Stern, E. Berg, P. Jarillo-Herrero, and S. Ilani. Cascade of phase transitions and Dirac revivals in magic-angle graphene. *Nature*, 582(7811):203–208, 2020.

[49] Dillon Wong, Kevin P. Nuckolls, Myungchul Oh, Biao Lian, Yonglong Xie, Sangjun Jeon, Kenji Watanabe, Takashi Taniguchi, B. Andrei Bernevig, and Ali Yazdani. Cascade of electronic transitions in magic-angle twisted bilayer graphene. *Nature*, 582(7811):198–202, 2020.

[50] Harpreet Singh Arora, Robert Polski, Yiran Zhang, Alex Thomson, Youngjoon Choi, Hyunjin Kim, Zhong Lin, Ilham Zaky Wilson, Xiaodong Xu, Jiun-Haw Chu, Kenji Watanabe, Takashi Taniguchi, Jason Alicea, and Stevan Nadj-Perge. Superconductivity in metallic twisted bilayer graphene stabilized by WSe2. *Nature*, 583(7816):379–384, 2020.

[51] Xiaobo Lu, Petr Stepanov, Wei Yang, Ming Xie, Mohammed Ali Aamir, Ipsita Das, Carles Urgell, Kenji Watanabe, Takashi Taniguchi, Guangyu Zhang, Adrian Bachtold, Allan H. MacDonald, and Dmitri K. Efetov. Superconductors, orbital magnets and correlated states in magic-angle bilayer graphene. *Nature*, 574(7780):653–657, 2019.

[52] A. Uri, S. Grover, Y. Cao, J. A. Crosse, K. Bagani, D. Rodan-Legrain, Y. Myasoedov, K. Watanabe, T. Taniguchi, P. Moon, M. Koshino, P. Jarillo-Herrero, and E. Zeldov. Mapping the twist-angle disorder and Landau levels in magic-angle graphene. *Nature*, 581(7806):47–52, 2020.

[53] Youngjoon Choi, Jeannette Kemmer, Yang Peng, Alex Thomson, Harpreet Arora, Robert Polski, Yiran Zhang, Hechen Ren, Jason Alicea, Gil Refael, Felix von Oppen, Kenji Watanabe, Takashi Taniguchi, and Stevan Nadj-Perge. Electronic correlations in twisted bilayer graphene near the magic angle. *Nature Physics*, 15(11):1174–1180, 2019.

[54] Yonglong Xie, Biao Lian, Berthold Jäck, Xiaomeng Liu, Cheng-Li Chiu, Kenji Watanabe, Takashi Taniguchi, B. Andrei Bernevig, and Ali Yazdani. Spectroscopic signatures of many-body correlations in magic-angle twisted bilayer graphene. *Nature*, 572(7767):101–105, 2019.

[55] Yuhang Jiang, Xinyuan Lai, Kenji Watanabe, Takashi Taniguchi, Kristjan Haule, Jinhai Mao, and Eva Y. Andrei. Charge order and broken rotational symmetry in magic-angle twisted bilayer graphene. *Nature*, 573(7772):91–95, 2019.

[56] G. H. Wannier. A Result Not Dependent on Rationality for Bloch Electrons in a Magnetic Field. *physica status solidi (b)*, 88(2):757–765, 1978.

[57] Shuang Wu, Zhenyuan Zhang, K. Watanabe, T. Taniguchi, and Eva Y. Andrei. Chern insulators, van Hove singularities and topological flat bands in magic-angle twisted bilayer graphene. *Nature Materials*, 20(4):488–494, 2021.

[58] Yu Saito, Jingyuan Ge, Louk Rademaker, Kenji Watanabe, Takashi Taniguchi, Dmitry A. Abanin, and Andrea F. Young. Hofstadter subband ferromagnetism and symmetry-broken Chern insulators in twisted bilayer graphene. *Nature Physics*, 17(4):478–481, 2021.

[59] Ipsita Das, Xiaobo Lu, Jonah Herzog-Arbeitman, Zhi-Da Song, Kenji Watanabe, Takashi Taniguchi, B. Andrei Bernevig, and Dmitri K. Efetov. Symmetry-broken Chern insulators and Rashba-like Landau-level crossings in magic-angle bilayer graphene. *Nature Physics*, 17(6):710–714, 2021.

[60] Zachary A H Goodwin, Valerio Vitale, Xia Liang, Arash A Mostofi, and Johannes Lischner. Hartree theory calculations of quasiparticle properties in twisted bilayer graphene. *arXiv*, 2020.

[61] Ming Xie and A. H. MacDonald. Nature of the Correlated Insulator States in Twisted Bilayer Graphene. *Physical Review Letters*, 124(9):097601, 2020.

[62] Kasra Hejazi, Chunxiao Liu, and Leon Balents. Landau levels in twisted bilayer graphene and semiclassical orbits. *Physical Review B*, 100(3):035115, 2019.

[63] Ya-Hui Zhang, Hoi Chun Po, and T. Senthil. Landau level degeneracy in twisted bilayer graphene: Role of symmetry breaking. *Physical Review B*, 100(12):125104, 2019.

[64] Stephen Carr, Shiang Fang, Hoi Chun Po, Ashvin Vishwanath, and Efthimios Kaxiras. Derivation of Wannier orbitals and minimal-basis tight-binding Hamiltonians for twisted bilayer graphene: First-principles approach. *Physical Review Research*, 1(3):033072, 2019.

[65] S. L. Tomarken, Y. Cao, A. Demir, K. Watanabe, T. Taniguchi, P. Jarillo-Herrero, and R. C. Ashoori. Electronic Compressibility of Magic-Angle Graphene Superlattices. *Physical Review Letters*, 123(4):046601, 2019.

[66] Youngjoon Choi, Hyunjin Kim, Yang Peng, Alex Thomson, Cyprian Lewandowski, Robert Polski, Yiran Zhang, Harpreet Singh Arora, Kenji Watanabe, Takashi Taniguchi, Jason Alicea, and Stevan Nadj-Perge. Correlation-driven topological phases in magic-angle twisted bilayer graphene. *Nature*, 589(7843):536–541, 2021.

[67] Louk Rademaker and Paula Mellado. Charge-transfer insulation in twisted bilayer graphene. *Physical Review B*, 98(23):235158, 2018.

[68] Stephen Carr, Shiang Fang, Ziyan Zhu, and Efthimios Kaxiras. Exact continuum model for low-energy electronic states of twisted bilayer graphene. *Physical Review Research*, 1(1):013001, 2019.

[69] Tommaso Cea, Niels R. Walet, and Francisco Guinea. Electronic band structure and pinning of Fermi energy to Van Hove singularities in twisted bilayer graphene: A self-consistent approach. *Physical Review B*, 100(20):205113, 2019.

[70] Louk Rademaker, Dmitry A. Abanin, and Paula Mellado. Charge smoothening and band flattening due to Hartree corrections in twisted bilayer graphene. *Physical Review B*, 100(20):205114, 2019.

[71] M. J. Calderón and E. Bascones. Interactions in the 8-orbital model for twisted bilayer graphene. *Physical Review B*, 102(15):155149, 2020.

[72] Lennart Klebl, Zachary A. H. Goodwin, Arash A. Mostofi, Dante M. Kennes, and Johannes Lischner. Importance of long-ranged electron-electron interactions for the magnetic phase diagram of twisted bilayer graphene. *Physical Review B*, 103(19):195127, 2021.

[73] Tommaso Cea and Francisco Guinea. Band structure and insulating states driven by Coulomb interaction in twisted bilayer graphene. *Physical Review B*, 102(4):045107, 2020.

[74] Ming Xie and Allan H MacDonald. Weak-field Hall Resistivity and Spin/Valley Flavor Symmetry Breaking in MAtBG. *arXiv : 2010.07928*, 2020.

[75] Johannes S. Hofmann, Erez Berg, and Debanjan Chowdhury. Superconductivity, pseudogap, and phase separation in topological flat bands. *Physical Review B*, 102(20):201112, 2020.

[76] B. Andrei Bernevig, Biao Lian, Aditya Cowsik, Fang Xie, Nicolas Regnault, and Zhi-Da Song. Twisted bilayer graphene. V. Exact analytic many-body excitations in Coulomb Hamiltonians: Charge gap, Goldstone modes, and absence of Cooper pairing. *Physical Review B*, 103(20):205415, 2021.

[77] Jeong Min Park, Yuan Cao, Kenji Watanabe, Takashi Taniguchi, and Pablo Jarillo-Herrero. Tunable strongly coupled superconductivity in magic-angle twisted trilayer graphene. *Nature*, 590(7845):249–255, 2021.

[78] Zeyu Hao, A. M. Zimmerman, Patrick Ledwith, Eslam Khalaf, Danial Haie Najafabadi, Kenji Watanabe, Takashi Taniguchi, Ashvin Vishwanath, and Philip Kim. Electric field–tunable superconductivity in alternating-twist magic-angle trilayer graphene. *Science*, 371(6534):1133–1138, 2021.

[79] Eslam Khalaf, Alex J. Kruchkov, Grigory Tarnopolsky, and Ashvin Vishwanath. Magic angle hierarchy in twisted graphene multilayers. *Physical Review B*, 100(8):085109, 2019.

[80] Øystein Fischer, Martin Kugler, Ivan Maggio-Aprile, Christophe Berthod, and Christoph Renner. Scanning tunneling spectroscopy of high-temperature superconductors. *Reviews of Modern Physics*, 79(1):353–419, 2007.

[81] Jinho Lee, K. Fujita, K. McElroy, J. A. Slezak, M. Wang, Y. Aiura, H. Bando, M. Ishikado, T. Masui, J.-X. Zhu, A. V. Balatsky, H. Eisaki, S. Uchida, and J. C. Davis. Interplay of electron–lattice interactions and superconductivity in Bi2Sr2CaCu2O8+. *Nature*, 442(7102):546–550, 2006.

[82] F. C. Niestemski, S. Kunwar, S. Zhou, Shiliang Li, H. Ding, Ziqiang Wang, Pengcheng Dai, and V. Madhavan. A distinct bosonic mode in an electron-doped high-transition-temperature superconductor. *Nature*, 450(7172):1058–1061, 2007.

[83] R. de Picciotto, M. Reznikov, M. Heiblum, V. Umansky, G. Bunin, and D. Mahalu. Direct observation of a fractional charge. *Nature*, 389(6647):162–164, 1997.

[84] K. M. Bastiaans, D. Cho, D. Chatzopoulos, M. Leeuwenhoek, C. Koks, and M. P. Allan. Imaging doubled shot noise in a Josephson scanning tunneling microscope. *Physical Review B*, 100(10):104506, 2019.

[85] Koen M Bastiaans, Damianos Chatzopoulos, Jian-Feng Ge, Doohee Cho, Willem O Tromp, Jan M van Ruitenbeek, Mark H Fischer, Pieter J de Visser, David J Thoen, Eduard F C Driessen, Teunis M Klapwijk, and Milan P Allan. Direct evidence for Cooper pairing without a spectral gap in a disordered superconductor above T_C. *arXiv : 2101.08535*, 2021.

[86] Yu Saito, Fangyuan Yang, Jingyuan Ge, Xiaoxue Liu, Takashi Taniguchi, Kenji Watanabe, J. I. A. Li, Erez Berg, and Andrea F. Young. Isospin Pomeranchuk effect in twisted bilayer graphene. *Nature*, 592(7853):220–224, 2021.

[87] Asaf Rozen, Jeong Min Park, Uri Zondiner, Yuan Cao, Daniel Rodan-Legrain, Takashi Taniguchi, Kenji Watanabe, Yuval Oreg, Ady Stern, Erez Berg, Pablo Jarillo-Herrero, and Shahal Ilani. Entropic evidence for a Pomeranchuk effect in magic-angle graphene. *Nature*, 592(7853):214–219, 2021.

[88] Yuan Cao, Daniel Rodan-Legrain, Jeong Min Park, Noah F. Q. Yuan, Kenji Watanabe, Takashi Taniguchi, Rafael M. Fernandes, Liang Fu, and Pablo Jarillo-Herrero. Nematicity and competing orders in superconducting magic-angle graphene. *Science*, 372(6539):264–271, 2021.